POLITECNICO
MILANO 1863

DEPARTMENT OF PHYSICS

Strong Field-Electron-XUV Interaction Simulator: Study of ensemble effects in attosecond streaking spectroscopy

---

Author:
Federico VISMARRA
Student ID: *918990*

Supervisors:
Prof. Mauro NISOLI
Prof. Fabrizio GIORGIS
Co-Supervisors:
Dr. Rocio BORREGO VARILLAS
Dr. Matteo LUCCHINI

Master in Physics Engineering
Photonics and Nano Optics

Academic year,
2019-2020

POLITECNICO DI MILANO

Summary

Department of Physics

Master in Physics Engineering

Strong Field-Electron-XUV Interaction Simulator: Study of ensemble effects in attosecond streaking spectroscopy

by Federico VISMARRA

The time scale of electron dynamics in atoms, molecules, and solids occurs in the attosecond domain (1 $as = 10^{-18}$ s).
Careful optimization of the attosecond techniques and tools are paving the way for the control of these dynamics with potential benefits on many research and industrial fields.

In this thesis work, I have developed a code for the simulation of *streaking photo-electron spectroscopy*, which is one of the fundamental techniques used by researchers to investigate electron-dynamics. In particular, streaking traces can be used to retrieve information on both the pulses (temporal characterization) and the sample (photoemission delays) by means of retrieval algorithms.
This technique exploits the interaction between an eXtreme Ultra Violet (XUV) attosecond pulse, and a delayed femtosecond (1 $fs = 10^{-15}$ s) InfraRed (IR) pulse, with an atomic/molecular sample.
Most codes for simulating and reconstructing streaking traces work under the hypothesis of flat spatial profiles of the IR and XUV fields. Although this assumption is correct for a single atom interaction or small XUV focus with respect to the IR, an experimental trace records the emitted photo-electrons from an ensemble of atoms/molecules and non-flat profiled fields, which are often comparable in size. These are non-idealities that must be taken into account when discussing the feasibility and the time resolution limits of the technique.
Thus, the objectives of this work are:

1) The development of a programme to simulate simple atomic photo-electron traces, with simulation software adding a spatial ensemble averaging for different IR-XUV radial profiles.

2) To test the robustness of a well-corroborated field reconstruction algorithm named extended Ptychographic Iterative Engine (ePIE) against these ensemble effects, and to report the reconstruction accuracy.

This thesis work is organized as follows:

- In the first chapter, I will introduce the state of the art regarding attosecond photo-electron spectroscopy, focusing on the reconstruction algorithm ePIE.
- In the second chapter, the theoretical background of photo-electron two-color (XUV and IR) interaction will be presented in great detail, exploiting a propagators formalism.
- In the third chapter, the Matlab programme SFEXIS will be presented as a simple tool to study two-color interaction phenomena.
- In the fourth chapter, the study of ensemble effects and robustness of ePIE is performed.

It will be shown that, even in the worst-case scenario, where the ensemble effects generate a difference in the real photo-electron trace up to the 60% with respect the ideal flat-field case, ePIE is quite robust with a relative error on the reconstructed fields that do not overcome 4%.

POLITECNICO DI MILANO

Sommario

Department of Physics

Master in Physics Engineering

Strong Field-Electron-XUV Interaction Simulator:
Study of ensemble effects in attosecond streaking spectroscopy

di Federico VISMARRA

Le tipica scala temporale dei processi elettronici in atomi, molecole e solidi appartiene al dominio degli attosecondi (1 $as = 10^{-18}$ s).
Perfezionare le tecniche di misura ad attosecondi potrà consentire, nel futuro, di controllare queste dinamiche con importanti conseguenze in diversi ambiti di ricerca fondamentale e industriale.

In questo lavoro di tesi, ho sviluppato un codice Matlab per la simulazione di tracce di foto-elettroni, generate dall'interazione tra impulsi ad attosecondi ultravioletti e un intenso impulso infrarosso a femtosecondi (1 $fs = 10^{-15}$ s) con un campione atomico/molecolare.
La traccia ottenuta, detta "streaking", appartiene alle principali tecniche usate per indagare processi ultra-veloci e risalire alle informazioni sui campi che l'hanno generata.
La maggior parte dei lavori in letteratura assume profili spaziali dei campi piatti, tale approssimazione, valida nel caso di interazione con un singolo atomo/molecola, risulta non corretta negli esperimenti i cui foto-elettroni sono generati dall'interazione con un getto atomico/molecolare.
Questa non idealità deve, dunque, essere studiata per comprendere l'impatto di questi effetti sui limiti di risoluzione della tecnica e, in particolare, sulle capacità di ricostruzione dei campi da una traccia sperimentale.
Gli obbiettivi di questa tesi sono pertanto:

1) Simulare tracce di streaking generate dall'interazione tra atomi e impulsi ultra-brevi, aggiungendo semplici effetti di insieme.

2) Testare la robustezza di un ben-noto algoritmo di ricostruzione dei campi, ePIE, contro questi effetti di insieme.

La tesi è organizzata come segue:

- Nel primo capitolo, lo stato dell'arte sulle tecniche di spettroscopia di foto-elettroni ad attosecondi e l'algoritmo di ricostruzione ePIE verranno presentati.

- Nel secondo capitolo, il contesto teorico di interazione di campo forte verrà trattata nel dettaglio, sfruttando il formalismo quantistico dei propagatori.
- Nel terzo capitolo, il codice sviluppato in Matlab verrà introdotto come semplice strumento di studio dei fenomeni di interazione forte.
- Nel quarto capitolo, lo studio degli effetti di volume e della robustezza di ePIE verranno discussi.

Come risultato si mostrerà che ePIE è relativamente robusto agli effetti di insieme e che è in grado nel peggior scenario, in cui le variazioni della traccia rispetto al caso ideale raggiungono il 60%, di ricostruire gli impulsi con un errore che non supera il 4%.

Acknowledgements

I am profoundly thankful to my supervisors: Rocio B.V. for the constant and valuable support and her wise and helpful advice, Matteo L. for the enlightening discussions and insightful suggestions, and last but not least, to Prof. Mauro Nisoli for the trust and for all the opportunities, including becoming part of this great Attosecond group.

I am also particularly grateful to Bruno M., for its practical directions on ePIE, to Yingxuan W. and Fabian H. for sharing their experimental knowledge during the time spent in the lab.
Thanks also to my pal Gian Luca D., an untiring friend in this and all the next scientific adventures.

Of course, I am deeply indebted to my parents Marco and Paola, who always gave me the freedom to forge my own path.
I am thankful to my brother Alessandro for sharing his work station during the last months allowing me to run the majority of simulations.

I would like to extend my sincere thanks to my brothers from different mothers Jacopo, Francesco e Matteo for all the good time spent in our second home.

Finally, a special thanks to Marta, my companion in life, and all my physics adventures.

Contents

To all my scientific mentors

> "I am a quantum engineer, but on
> Sunday I have Principles"
>
> ---
>
> J.S. Bell

Chapter 1

Introduction to attosecond spectroscopy and work motivation

In this first chapter, after an introduction of the attosecond physics general mission and its basic tools, I will synthetically provide a state of the art review of *attosecond streaking photo-electron spectroscopy*, which is one of the possible attosecond experimental investigation techniques. In Section 1.2, I will focus the attention on *streaking spectroscopy* experimental relevance.

One of the key points behind this measurement is the retrieval of the fields that generate it, iterative algorithms typically do this task. In Section 1.2.2, I will, then, present the main reconstruction algorithms, with a focus on extended Ptychographic Iterative Engine (ePIE).
Despite the wide use of these algorithms, ensemble effects (i.e. the presence of an averaged interaction caused by the presence of multiple atomic/molecular species distributed among non-flat field profiles) have been neglected up to now. Thus, Section 1.3 will be devoted to an introductory discussion on the different kind of ensemble effects.

The discussion of their impact on the streaking traces and the reconstruction algorithm ePIE will be the main scope of this thesis, and it will be developed in the following Chapters.

1.1 Introduction to Attosecond Physics

Why Attosecond Physics?

We perceive a falling object because our brain can process the light received by our retina approximately every tens of *millisecond* (1 ms =$\mathbf{10^{-3}}$ s). Everything that is faster is, almost, imperceptible to our sense. Today, we can easily do slow-motion videos of a hummingbird wing-flapping, or a bullet breaking a water balloon because we have developed commercial devices that enhance our perception of reality by acquiring images down to the *microsecond* (1 μs =$\mathbf{10^{-6}}$ s).

This time resolution is still not enough. Indeed, many fundamental physical processes happen at an even smaller time scale, reaching the domain of attoseconds (1 as =$\mathbf{10^{-18}}$ s).

Consider, now, as simple proof of concept, a quantum system in superposition between ground-level, of energy ϵ_0, and the first excited level, of energy ϵ_1:

$$|\Psi\rangle = c_g |\psi_g\rangle + c_e |\psi_e\rangle \tag{1.1}$$

with c_e and c_g real weights, for simplicity, and

$$|\psi_g(t)\rangle = |0\rangle e^{-\frac{i\epsilon_0}{\hbar}t} \qquad\qquad |\psi_e(t)\rangle = |1\rangle e^{-\frac{i\epsilon_1}{\hbar}t}$$

where $\hbar$ is the reduced Planck constant.
We can write the expectation value of a generic hermitian and symmetric observable $\hat{P}$, $P(t) = \langle\Psi| \hat{P} |\Psi\rangle$, as:

$$P(t) = |c_g|^2 \langle 0| \hat{P} |0\rangle + |c_e|^2 \langle 1| \hat{P} |1\rangle + 2c_e c_g \langle 0| \hat{P} |1\rangle \cos\left(\frac{\epsilon_1 - \epsilon_0}{\hbar} t\right) \tag{1.2}$$

While the first two terms do not depend on time, the third, instead, does. This creates a dynamic for the observable $P(t)$ with a characteristic time, T_d, given by:

$$T_d = \frac{2\pi\hbar}{\epsilon_1 - \epsilon_0} \tag{1.3}$$

For example, we can look at the time-fluctuation of an electron radial probability density, $R(r,t)$, in Hydrogen atom with 1s, ground state, and 2p, excited state:

$$R(r,t) = 2\pi \int_0^{\pi} |\langle\Psi(t)|\Psi(t)\rangle|^2 r^2 \sin\theta d\theta \tag{1.4}$$

It can be shown that the energy difference of the two levels is $\Delta\epsilon = \epsilon_1 - \epsilon_0 \approx 10$ eV, thus, by using Eq. (1.3), the $R(r,t)$ dynamics develops in $T_d \approx 400$ as.

As a rule of thumb, every time the energy difference of a quantum system is in the eV order, the dynamics of its observables occur within attoseconds. The previous statement is true for most all-electron dynamics in atoms, molecules, and solids.

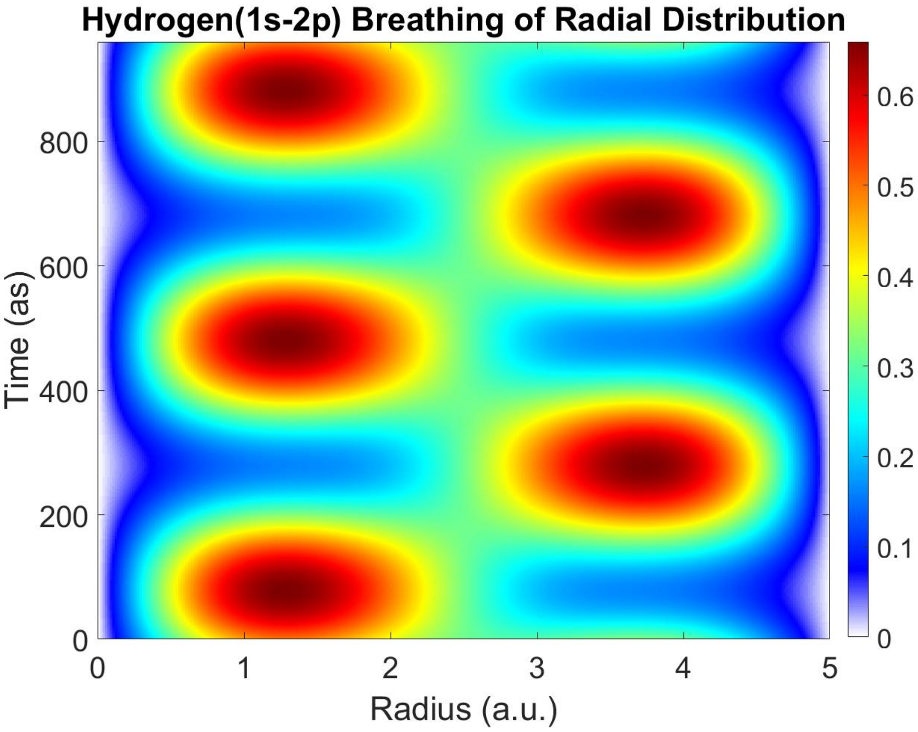

FIGURE 1.1: Radial Distribution probability map. Simulation of the exact radial probability amplitude for an H-states superposition (1s-2p) as a function of time. One can easily observe a period in the radial "breathing" process around 400 as.

Now, to "see" these dynamics, we must possess a controlled tool with an even shorter time duration.
This is the reason why researchers use attosecond light-pulses to disclose the physics behind ultra-fast phenomena. An additional motivation that pushes the entire field of research is the capability one day, with these same tools, to control and to engineer these dynamics.

What kind of light do we need to generate attosecond pulse?

To generate a *traveling* pulse with a duration in the order of tens of hundreds of attoseconds we need two key elements: bandwidth and frequency.
As it is well-known by Fourier analysis, the more the available bandwidth, the shorter, *potentially*, is the time duration. While for a pulse centered in the InfraRed (IR) $\lambda = 800$ nm its minimum time duration is around $T_{pulse} = \frac{\lambda}{c} = 2.67$ fs, for a light field with central component in the eXtreme UltraViolet (XUV) at $\lambda = 30$ nm, instead, the minimum duration is around $T_{pulse} = 100$ as.
For this reason, classical techniques to reach the attosecond regime are based on light sources with broad spectral bandwidths whose central frequency is centred in the XUV range.
The most common sources that fit these requirements are Free Electron Lasers (FEL) and High Harmonics Generation (HHG) tabletop setups.
In the following we will focus on the latter process.

1.1.1 High Harmonics Generation

When a "moderately" high-intensity laser pulse ($10^{12} - 10^{14}\ \frac{W}{cm^2}$) meets a gas or a solid target, XUV radiation characterized by a plateau, see Fig.1.2, of several orders of odd harmonics of the fundamental frequency can be emitted.

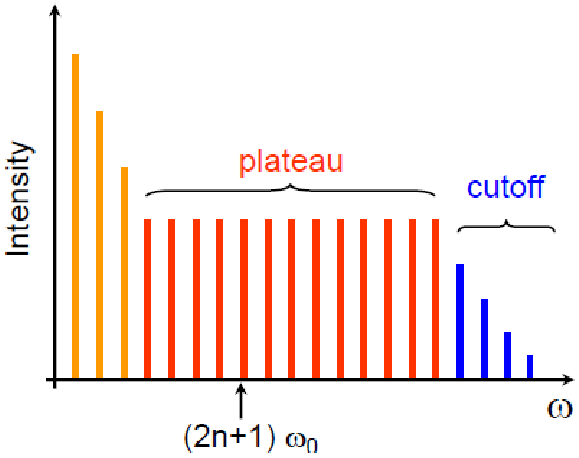

FIGURE 1.2: Schematic representation of High Harmonics generated by a laser of frequency ω_0.

This process is the result of a complex non-linear process between the atoms, and the field, which can be solved in a semi-classical environment with the support of a general theory named Strong Field Approximation (SFA), discussed[1] in details in Chapter 2.

The HHG phenomenon can be well-described with different rigorous approaches, like the *Leweinstein model*, or with a path-integrals-based formalism. Besides these complex discussions, the key process that makes HHG possible can be viewed as: *an in-phase sum of radiation emitted by oscillating dipoles* [1] *triggered and driven by an intense laser field*, often called *driving pulse*.

As a matter of fact, these peculiar emitting dipoles are the manifestation of an oscillating superposition between atomic ground-state and free-electron continuum-states. The role of the intense field is both to promote[2] the electron in the continuum, without completely emptying the starting level, and to efficiently drives the dipole oscillation mechanism.

These two requirements set the most suitable HHG-working-conditions for the driving intense laser field. In order to properly understand those let us, first, use a simple model, named *three step model* [2].

Three Step Model

The HHG process can be "semi"-classically viewed as the result of three subsequent steps:

---

[1] The theoretical foundations and proof of the theory are presented in Appendix A.

[2] Or better: to make the probability of detection in the continuum different from zero.

1) **Ionization:**
   At sufficient high laser intensities, we have a non-negligible probability of quantum tunnelling. Under this condition, an electron can tunnel through the Coulomb barrier bent by the field.
   The electron is, then, "emitted" as a freed electron, and it moves away accelerated by the electric force of the driving field.

2) **Motion After Ionization:**
   After ionization, the electron continues to move following the field potential. However, the electromagnetic wave propagates, thus, while the electrons move the field slowly changes its electric potential profile. This makes the electron starts moving backwards and, eventually, to re-encounter the parent ion. In this step, the electron is described as a Newton-particle.

3) **Recollision:**
   If the electron "re-encounters" the ions, recombination can occur causing a release of a light burst, whose energy is given by the ionization potential I_P plus all the acquired kinetic energy E_k.

$$\hbar\omega = I_p + E_k \tag{1.5}$$

If the acquired kinetic energy is high enough, an XUV pulse can be generated every half-period of the intense driving field, as shown in Fig. 1.3, resulting in an attosecond train of pulses. After few classical calculations [2], it can be shown that the maximum photon energy, or cut-off energy, is given by:

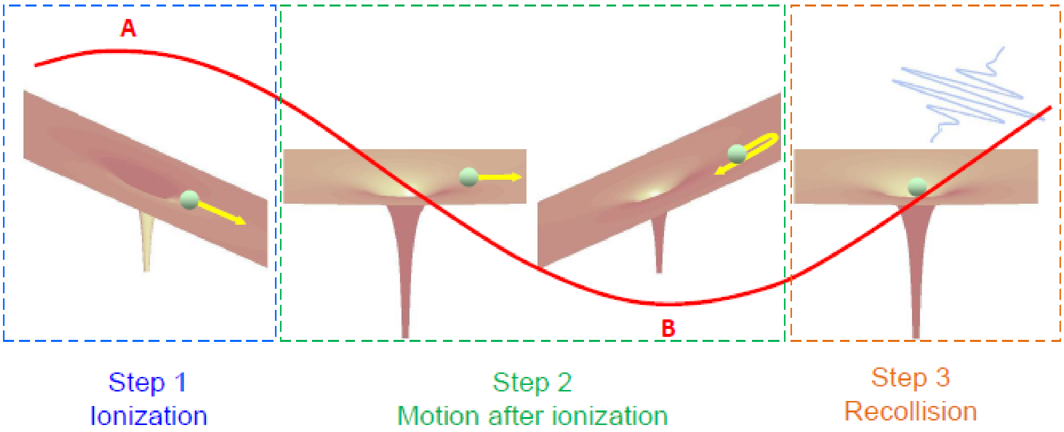

FIGURE 1.3: Schematic representation of the Three-step model. This process repeats every half period resulting in an attosecond pulse train, whose Fourier transform is an odd harmonic spectrum.

$$\hbar\omega_{HHmax} = I_P + 3.17U_P \tag{1.6}$$

where U_P is called ponderomotive energy:

$$U_P \approx I_L\lambda_0^2 \tag{1.7}$$

with λ_0 and I_L the driving field wavelength and intensity respectively.

Now we are almost ready to understand the optimal working-conditions that the driving pulse should satisfy in order to generate a High Harmonics spectrum efficiently.
Through the three-step model, we could infer, using Eq. (1.6) and Eq. (1.7), that the lower the frequency of the driving field, the higher the order of the generated harmonics and the plateau extension and, as a consequence, the lower the emitted pulse duration. However, two limits cannot be foreseen by the three-step model, and that must be taken into consideration when engineering a real HHG-based experiment.

First, if the intensity is too high the atom is entirely ionized, or depleted, thus, no oscillating dipole, and, as a consequence, no radiation is emitted. *Second*, if the wavelength is too large, then, due to diffraction, the free electron wavefunction broads significantly in free propagation, and, hence, the recombination probability and, so, the emitted radiation drops down to negligible values.

This is the reason why a common HHG-working-condition is an IR field, the driving pulse, centred around 800 nm with an intensity of around $10^{13}\ \frac{W}{cm^2}$.

Single Attosecond Pulse (SAP)

An Attosecond Train of Pulses (ATP), separated by half optical cycle of the IR, can be used in several experiments where attosecond temporal resolution is not an essential requirement. However, to see ultrafast dynamics, for example, ultra-fast charge migration processes in molecules [3], we need to create a single attosecond burst of light for each IR pulse.

Therefore, in recent years, many single attosecond pulse technologies have been developed and implemented in laboratories. Among these techniques, often called *gating techniques* [4], we can mention:

- *Spectral Gating*, in which one filters only the most intense harmonics peaks.
- *Polarization Gating*, in which one produces a peculiar IR profile (a doubly circularly polarized field with a linear polarization that lasts one optical cycle) see Fig. 1.4.
- *Ionization gating*, where the single attosecond pulse is generated at the rising edge of a driving pulse with a controlled intensity; so that, after few cycles, the intensity is so high that it completely depletes the HHG medium forbidding, then, any further generation.

As a last remark, the key requirement to practically use each one of these gating techniques is a controlled Carrier Envelope Phase (CEP), [5], of the driving IR pulse.

The first observation of the HHG process was done by McPherson in 1987 [6]. A 1 ps pulse at 248 nm, from an excimer laser, was focused on a Ne gas-jet at

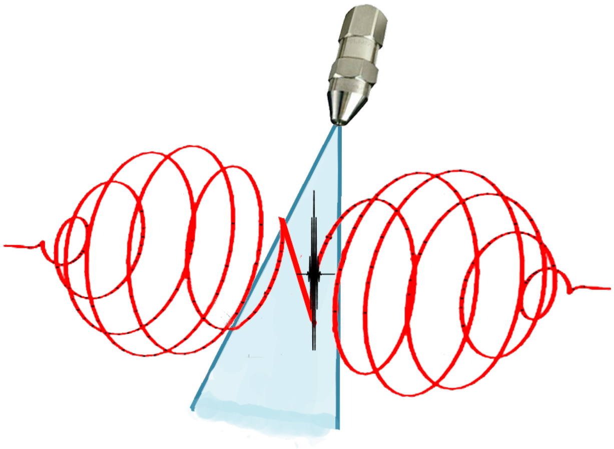

FIGURE 1.4: Polarization gating, in red the driving IR pulse and in black the generated SAP in a noble gas jet, emitted by the grey nozzle. The attosecond pulse is generated only in the linearly polarized part of the IR pulse.

$I = 10^{15} - 10^{16} \frac{W}{cm^2}$. The result was an high harmonics generation till the 17^{th} order, $\lambda = 14.6\,nm$.

By exploiting this remarkable process combined with a gating technique, we can generate a concise burst of XUV light. As an outstanding example, in 2006, at Politecnico di Milano, a 130 as HH generated pulse broke what was, at that time, the world record for the shortest generated electromagnetic wave [7].

1.2 Two-color attosecond photo-electron spectroscopy

At this point, we have understood how to generate an XUV single attosecond pulse from an intense IR field, experimentally, one of the most extended approaches to track attosecond dynamics is shown in Fig. 1.5.
This scheme is analogous to a standard pump-probe experiment. In fact, in the most common working condition, the *XUV pulse starts the dynamics*, as a "pump", and the IR fields follow it as a *delayed* "probe".

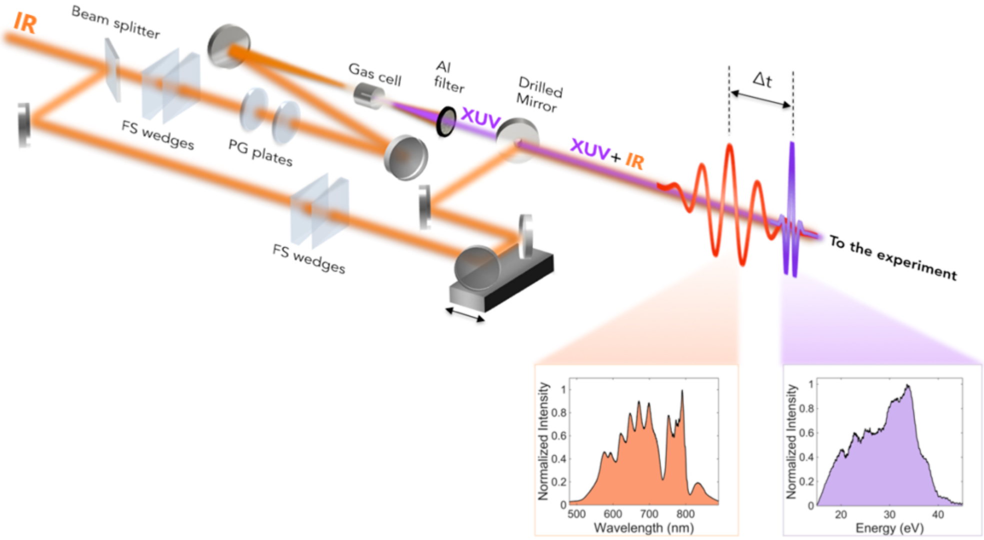

FIGURE 1.5: Possible pump-probe, or "pump-driver", experimental setup with single attosecond pulse generation implementing Polarization Gating (PG), with a delay stage for the IR. From [8]

However, referring to the IR as a "probe" is a conceptual mistake. Indeed, due to the high intensity reached by the streaking field the interaction with the sample is in a strong non-perturbative regime.

Therefore, the role of IR is, more correctly, *to drive the XUV-started dynamics* by exploring different XUV-IR delays, and, as reported in several pioneering experiments, to *control these dynamics*: e.g., to localize the remaining bounded electron in an XUV-started dissociation dynamics of D_2^+ [9], or to control the photo-fragmentation of Phenylalanine [3].
Once the Strong Field-sample-XUV interaction, or simply two-color interaction, later discussed in Chapter 2, has occurred, one has to select the most suitable observable to track and discover the ultrafast-dynamics occurring in the sample, which, in principle, could be an atom, a molecule, or a solid surface.
Few examples are:

- *Angular Asymmetry* in the velocity distribution of molecular photo-fragment, as in [9].
- *Quantum yield of Photo-fragments*, as in [3].

- *XUV spectrum transient absorption*, as in [10]
- *Photo-Electron kinetic energy*, as in[11].

We will discuss the later kind of observable, the kinetic energy of the emitted photo-electron, which gives birth, in our context, to the *two-color attosecond photo-electron spectroscopy*, which could be both obtained from a single attosecond pulse or a train of attosecond pulses.
If we can achieve a single ionizing pulse, the ejected electron follows the IR field giving rise to what is known as *streaking trace*.

1.2.1 Relevance of attosecond streaking spectroscopy

An attosecond streaking spectroscopy is, then, a 2-Dimensional map that counts the number of photo-electrons emitted during the sample-fields interaction in a specific energy range, by exploring different delays between the ionizing, which in our case lies in the XUV range and a second pulse, IR in our case.
As it will be deeply discussed in Chapter 2, the final streaking trace is a complex interference process between different photo-ionization quantum-paths. Each one of them is characterized by a phase term, called Volkov phase, which is a function of the strong-IR-field [12].
The mechanism can be "simply" viewed as the result of an interplay between the XUV ionization of a bounded electron, from a ground state to a final continuum state at $\hbar\omega_{XUV} - I_P$, and the contemporary presence of an IR-Field, whose role is to *streak* up and down in energy the emitted electron, or photo-electron, during its propagation to the detector.

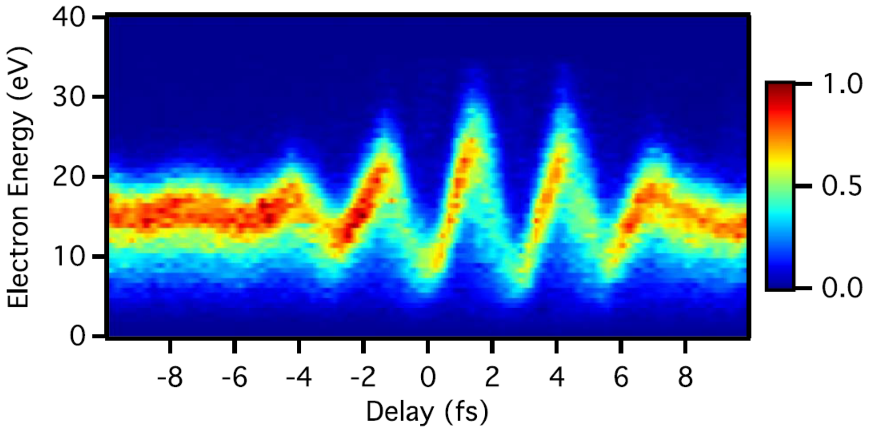

FIGURE 1.6: Experimental streaking trace of Ne, as the atomic target, interacting with an IR field and a single attosecond pulse generated with an HHG process in Ar, from [11].

Why attosecond streaking spectroscopy is important?

Photo-electron streaking traces are constantly used in modern attosecond laboratories. In fact, once a pump, XUV, and a streaking driver field are available from previous stages of the experimental setup, see Fig. 1.5, a photo-electron trace can be obtained with just two additional elements: a sample, like a gas jet of atoms or molecules, which interacts with the two fields and emits photo-electrons; and a recording device that maps the photo-electrons energy distribution, like a Time-Of-Flight (TOF) or a Velocity Map Imaging (VMI) spectrometer, see [4].

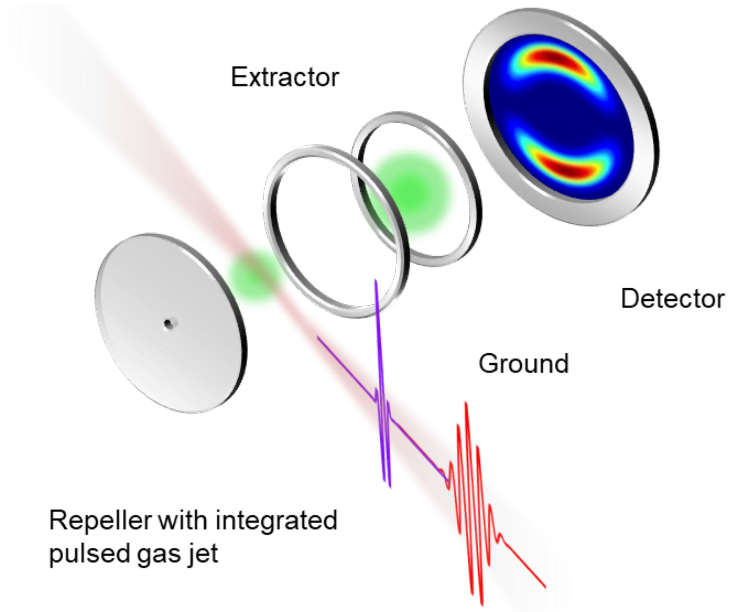

FIGURE 1.7: Possible configuration of a velocity map imaging spectrometer. The photo-electrons are emitted in the interaction zone between the gas jet and the fields. the electron arrival time is measured as well as the angular distribution for each delay-time.

Attosecond streaking spectroscopy offers a *deep insight into the physics* behind photo-ionization processes. An outstanding example, which can be measured from a streaking trace [11], is the so-called *delay in photo-emission* [13], briefly present in Chapter 2, which has also opened a great debate on *the tunneling time problem* [14].

Finally, in addition to the already discussed fundamental relevance in the investigation of ultrafast dynamics, these traces are widely used by experimental physicists *to benchmark and to optimize* the attosecond setup performances before any experiment, for example in the reconstruction of both XUV and IR pulses.

These are the reasons why, in order to give a theoretical support to the experiments running in the laboratory, I have developed a simple Matlab simulation tools, **SFEXIS**, **S**trong **F**ield **E**lectron **X**UV **I**nteraction **S**imulator, see Chapter 3, which is capable of generating a customizable *photo-electron streaking trace*, within certain approximations discussed thoroughly in Chapter 2. The software can simulate, also, a relevant collective effect, later discussed, allowing a study on the impact of these non-idealities on the expected experimental traces.

1.2.2 Attosecond Burst reconstruction from streaking traces

During the last decade, one of the most pressing challenges to the feasibility of attosecond technology was to develop techniques capable of completely characterizing the electric field of an isolated attosecond pulse or a train of attosecond pulses. Since then, photo-electron streaking traces have proven to be the most suitable starting point for reconstruction techniques, which are mostly based on the Frequency Resolved Optical Gating for Complete Reconstruction of Attosecond Burst (FROG-CRAB) method [15], even if alternatives are still under recent discussion, e.g. [16].

Starting from the FROG-CRAB general method, which was inspired by the widely-established FROG technique [17], different algorithms have been implemented, like Principal Component Generalized Projections Algorithm (PCGPA) [15], Volkov Transformed Generalized Projection Algorithm (VTGPA) [18], Ptychographic Iterative Engine (PIE), and extended Ptychographic Iterative Engine (ePIE) [19].

ePIE is an incredibly robust, fast and versatile algorithm capable of reconstructing both the IR-driving field and the attosecond XUV pulse from an input photo-electron trace. As for the other FROG-CRAB based algorithms, ePIE exploits the theoretical result from Strong Field theory of two-color interaction in the framework of single active electron (SAE) and within the dipole approximation, see Chapter 2.

Without entering the physical details, formally presented in Chapter 2, let us approach the problem from a purely mathematical perspective.

It will be shown that the probability density, $|a_{\mathbf{p}}|^2$ of detecting an emitted photo-electron with momentum **p** from a single atomic level at energy $-I_P$, for a certain delay τ between XUV and IR, is equal, in *atomic units*, to:

$$|a_{\mathbf{p}}(\tau)|^2 = \left| \int_{-\infty}^{+\infty} \mathbf{E}_{XUV}(t) \cdot \mathbf{d}[\mathbf{p} + \mathbf{A}_{IR}(t-\tau)] e^{-iS(\mathbf{p},t,\tau)+iI_P t} dt \right|^2 \tag{1.8}$$

where $\mathbf{A}_{IR}$ and $\mathbf{E}_{XUV}$ are the IR vector potential and XUV electric field respectively; $S(\mathbf{p}, \tau, t)$ is the semi-classical action defined as:

$$S(\tau, \mathbf{p}, t) = \frac{1}{2}|\mathbf{p}|^2 t - \phi_{\mathbf{p}}(t-\tau) \tag{1.9}$$

with,

$$\phi_{\mathbf{p}}(t-\tau) = -\int_t^{\infty} (\mathbf{p} \cdot \mathbf{A}_{IR}(t'-\tau) + |\mathbf{A}_{IR}(t'-\tau)|^2) dt' \tag{1.10}$$

and $\mathbf{d}[\mathbf{p} + \mathbf{A}_{IR}(t-\tau)]$ is the dipole transition element from the ground state to the continuum with momentum $\mathbf{p} + \mathbf{A}_{IR}(t-\tau)$.

Here, ePIE, similarly as other reconstruction algorithm, introduces three main approximations:

1) Central Momentum Approximation (CMA): in which we assume $\phi_{\mathbf{p}}(t-\tau) = \phi_{\mathbf{p}_C}(t-\tau)$ [2], where $\mathbf{p}_C = \omega_{XUV} - I_P$ is the unstreaked central momentum of the photo-electron trace, i.e. the central momentum of a XUV only trace, with central frequency ω_{XUV} left part of Fig.1.6.

2) The dipole term is seen as a flat function of **p**, and it is set to an unitary function.

3) We look at a 1D momentum distribution, $\mathbf{p} \to p$, therefore neglecting angular effects and assuming linearly polarized fields among the same direction.

While the first approximation is generally hard to remove, otherwise, as it will be understood later, we cannot use ePIE, the second can be slightly weakened by imposing [20]:

$$\mathbf{E}_{XUV}(t) \cdot \mathbf{d}[\mathbf{p} + \mathbf{A}_{IR}(t-\tau)] \approx E_{at}(t) \tag{1.11}$$

So, instead of neglecting the role of the dipole, we create an equivalent field composed by the XUV field and the dipole and we call it "atomic electric field" E_{at}, whose Fourier transform is:

$$\tilde{E}_{at}(\omega) = \mathcal{F}\{E_{at}(t)\} = \tilde{E}_{XUV}(\omega)\sigma_d(\omega)e^{i\varphi(\omega)} \tag{1.12}$$

therefore, as a first and rough approximation, the role of the dipole transition element is converted into a cross-section factor, $\sigma_d(\omega)$, times a phase term $\varphi_d(\omega)$. Using the above approximation Eq. 1.8 can be written as:

$$|a_p(\tau)|^2 = \Big|\int_{-\infty}^{+\infty} E_{at}(t)e^{i\phi_{\mathbf{p}C}(t-\tau)}e^{i(\frac{p^2}{2}+I_P)t}dt\Big|^2 \tag{1.13}$$

As already mentioned, a trace, like the one in Fig. 1.6, is usually represented as a function of the photo-electron energy, rather than the momentum, so in Eq. (1.13) we are missing a jacobian factor, see Chapter 2 for details.
Finally, the energy probability density of detecting a photo-electron with energy $\epsilon = \frac{p^2}{2}$, $\mathcal{A}(\epsilon, \tau)$, or the *photo-electron energy streaking trace* is given by:

$$\mathcal{A}(\epsilon,\tau) = 2\sqrt{\epsilon}\Big|\int_{-\infty}^{+\infty} E_{at}(t)e^{i\phi_{\mathbf{p}C}(t-\tau)}e^{i(\epsilon+I_P)t}dt\Big|^2 \tag{1.14}$$

A part from a rigid shift in energy of $-I_P$, Eq. (1.14) is the Fourier Transform (in atomic units!) from ϵ to t of a pulse function, $E_{at}(t)$, times a delayed pure phase gate function, $G(t-\tau)$, defined as:

$$G(t-\tau) = e^{i\phi_{\mathbf{p}C}(t-\tau)} \tag{1.15}$$

Thus, we can rewrite the previous equation as:

$$\boxed{\mathcal{A}(\epsilon,\tau) = 2\sqrt{\epsilon}\Big|\int_{-\infty}^{+\infty} E_{at}(t)G(t-\tau)e^{i(\epsilon+I_P)t}dt\Big|^2} \tag{1.16}$$

Therefore, by starting from an input streaking trace, $\mathcal{A}_{IN}(\epsilon, \tau)$, a ptychographic algorithm is capable of reconstructing $E_{at}(t)$, when $G(t-\tau)$ is known (Pie), or, as in our case, it can reconstruct both the gate and the pulse (extended Pie).
As a side comment, we observe that if the gate function is unitary, then Eq. (1.16) is, actually, equal to the replica of the XUV-spectrum (or better of the atomic field spectrum) centred at $\omega_{XUV} - I_P$. This fact enforces the "simple" interpretation of

a photo-electrons trace, mentioned at the begging of this section.
At this point, I'm presenting in the details the ePIE algorithm, which will be used and tested in Chapter 4.

The extended Ptychographic Iterative Engine (ePIE)

The ePIE algorithm works as follows:
It starts from an input spectrogram $\mathcal{S}_{IN}$:

$$\boxed{\mathcal{S}_{IN}(\omega,\tau) = \left| \int_{-\infty}^{+\infty} E_{at}(t) G(t-\tau) e^{i\omega t} dt \right|^2} \tag{1.17}$$

where both $E_{at}(t)$, $G(t-\tau)$ are unknown.
$\mathcal{S}_{IN}(\omega,\tau)$ is almost equivalent to $\mathcal{A}(\epsilon,\tau)$ of Eq. (1.16), which is usually the quantity that is measured/simulated:

$$\mathcal{S}_{IN}(\omega,\tau) = \frac{\mathcal{A}(\epsilon + I_P, \tau)}{2\sqrt{\epsilon + I_P}}$$

where the equivalence between $\epsilon \to \omega$ holds thanks to atomic units.

As initial guesses, the atomic field, $E_{at}^{(0)}(t)$, is taken as a white noise signal with a certain envelope, and the gate function, $G^{(0)}(t)$, is built through procedures like the *center of mass method* [21].
The ptychographic iterative engine is composed by a general loop, j, and a nested delay loop τ_n, so that the fields are updated every delay step, which helps improving the convergence.
Thus, for each delay τ_n and, then, for each iteration j-th, the following procedure is repeated:

- Calculation of $\mathcal{E}_j^{(0)}(t,\tau_n) = E_{at}^{(j,n)}(t) G^{(j,n)}(t-\tau_n)$, often called exit function. Note that, if we are at the first cycle the initial guess $E_{at}^{(0)}(t)$, $G^{(0)}(t)$ is used.
- The exit field Fourier transform, $\tilde{\mathcal{E}}_j^{(0)}(\omega,\tau_n)$, is computed. This is a critical step in which we need the *Central Momentum Approximation*. Indeed, without it, $G(t-\tau,\omega)$ would be a function also of ω (or better of p) see Eq. (1.10), making the computation of the exit field Fourier transform completely meaningless.
- $\tilde{\mathcal{E}}_j^{(1)}(\omega,\tau_n) = \dfrac{\tilde{\mathcal{E}}_j^{(0)}(\omega,\tau_n)}{|\tilde{\mathcal{E}}_j^{(0)}(\omega,\tau_n)|} \sqrt{\mathcal{S}_{IN}(\omega,\tau)}$, similarly to what is commonly done in a FROG reconstruction, we update only the modulus of the exit field Fourier transform exploiting the input spectrogram.
- $\mathcal{E}_j^{(1)}(t,\tau_n)$ is retrieved, the atomic field is updated. Note: if we are at the end of the delay cycle the updating occurs on $j \to j+1$.

$$E_{at}^{(j,n+1)}(t) = E_{at}^{(j,n)}(t) + \beta_E U_{j,n}(t-\tau_n)[\mathcal{E}_j^{(1)}(t,\tau_n) - \mathcal{E}_j^{(0)}(t,\tau_n)] \tag{1.18}$$

where $\beta_E \in$ is a convergence parameter $\beta_E \in$[0,1), and

$$U_{j,n}(t) = \frac{conj(G^{(j,n)}(t))}{max\{|(G^{(j,n)}(t)|^2\}}$$

At this point, a similar procedure is performed for the gate function, $G^{(j,n)}$:

- Calculation of exit field $\mathcal{E}_j^{(2)}(t,\tau_n) = E_{at}^{(j,n)}(t+\tau_n)G^{(j,n)}(t)$.
- Exit field Fourier transform, $\tilde{\mathcal{E}}_j^{(2)}(\omega,\tau_n)$, is computed.
- $\tilde{\mathcal{E}}_j^{(3)}(\omega,\tau_n) = \dfrac{\tilde{\mathcal{E}}_j^{(2)}(\omega,\tau_n)}{|\tilde{\mathcal{E}}_j^{(2)}(\omega,\tau_n)|}\sqrt{\mathcal{S}_{IN}(\omega,\tau)}$.
- $\mathcal{E}_j^{(3)}(t,\tau_n)$ is retrieved and the gate function, that contains the IR field, is calculated as:

$$G_{temp}^{(j,n+1)}(t) = G^{(j,n)}(t) + \beta_G V_{j,n}(t-\tau_n)[\mathcal{E}_j^{(3)}(t,\tau_n) - \mathcal{E}_j^{(2)}(t,\tau_n)] \tag{1.19}$$

where β_G is a convergence parameter $\beta_G \in$ [0,1), and

$$V_{j,n}(t) = \frac{conj(E_{at}^{(j,n)}(t))}{max\{|E_{at}^{(j,n)}(t))|^2\}}$$

Often an additional constraint is imposed, since the gate must result to be a pure phase object:

$$G^{(j,n+1)}(t) = e^{iarg\{G_{temp}^{(j,n+1)}(t)\}} \tag{1.20}$$

Once the nested loop is ended, $\mathcal{S}_j(\omega,\tau)$ is calculated together with an error parameter, which is used by the user to check whether the algorithm is converging to a solution or not.

$$Err = min_\gamma\left\{\sqrt{\frac{1}{MN}(\mathcal{S}_j(t,\tau) - \gamma\mathcal{S}_{IN}(t,\tau))}\right\} \tag{1.21}$$

where N is the length of the delay axis and M is the length of the ω axis.
The typically stopping condition is on the maximum number of iteration j, which can be interchanged with a stopping condition on the error. As discussed in the original work by Lucchini et al. [19], due to the lack of a theoretical framework, the convergence of the algorithm is strictly correlated by the choice of β_E and β_G, whose values must be finely searched.
However, as proved and discussed many times through the years, [20, 22] ePIE has proved to be: robust to the noise, robust to sub-sampling, reliable as the other reconstruction algorithm but faster and, in some cases, more accurate.

Due to the importance of photo-electron streaking traces in the extraction of essential information on both the fields and the sample, ePIE, and more generally,

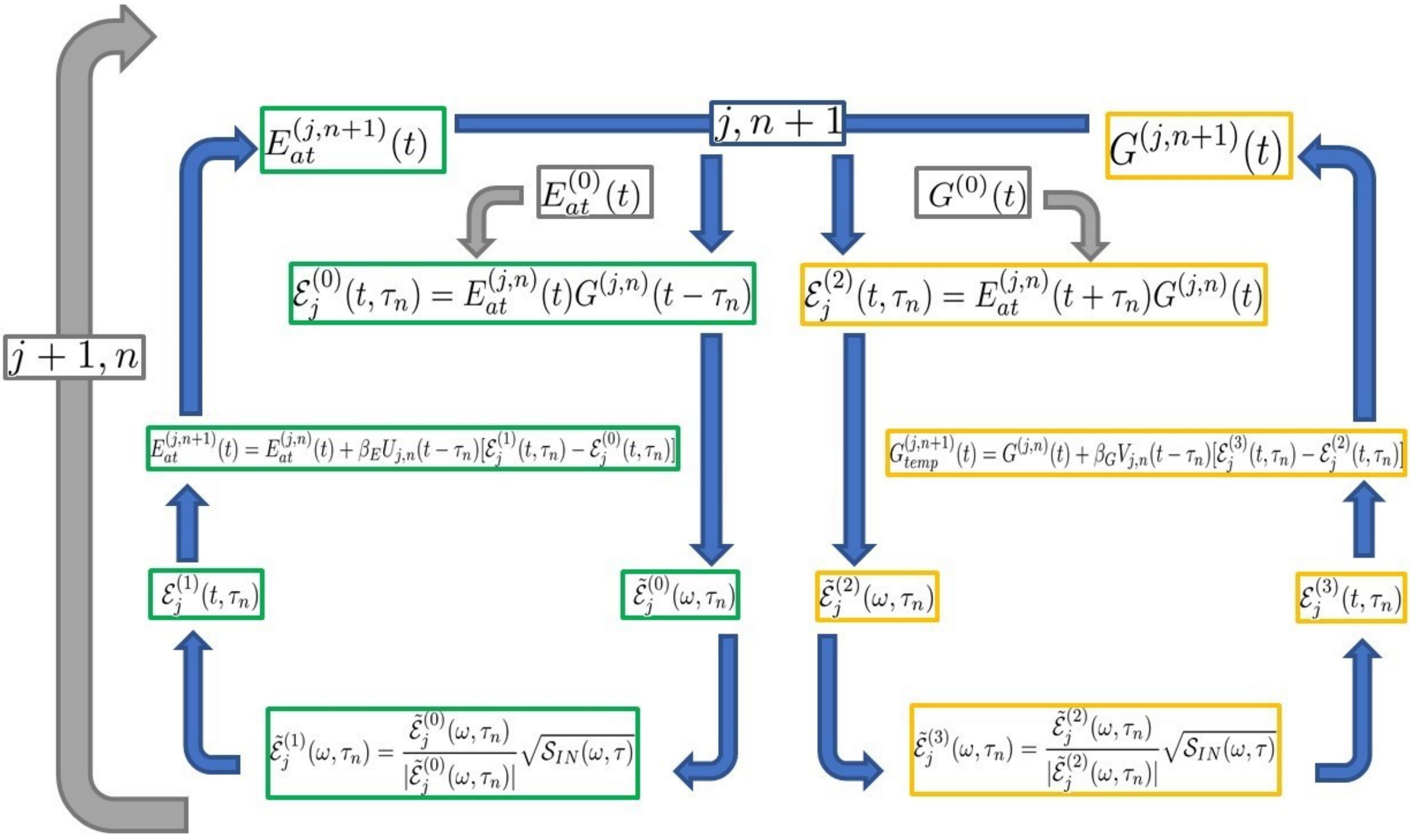

FIGURE 1.8: Schematic FlowChart of ePIE algorithm.

all reconstruction algorithms are under the spotlight of many practical discussions. All of these discussions have two fundamental aims:

1) To track down the effects, on the photo-electron trace, generated by the introduction of approximations This is usually done by simulating the physical event with and without the effect under investigation.

2) To test the reconstruction algorithm under real experimental condition (e.g. noise), which may reduce the reconstruction accuracy.

As an example, in a recent study, Gaumnitz and co-workers have studied the efficiency of the reconstruction algorithm VTGPA by including partial average over the angular distribution [23], ans so, by adding in the reconstruction the angular information hidden in Eq. (1.8).

1.3 Ensemble Effects in photo-electron streaking trace

Usually, we treat experimental photo-electron streaking trace as the result of an ideal interaction between a single atom (or molecule) and flat-profiled fields, as in Eq. (1.8). This is generally not experimentally true.
Indeed, in all the experiments involving a gas jet apparatus, the recorded photo-electron trace is a collection of the electrons emitted by an ensemble of atoms (or molecules). In other words, each photo-electron is emitted and then propagates in a different spatial region of the fields. As a consequence, it experiences different values of the pulses during the interaction with them. These phenomena, which could go under the name of *ensemble effect*, may show relevant consequences in the final energy distribution of the experimental photo-electron trace, compared to the ideal case.

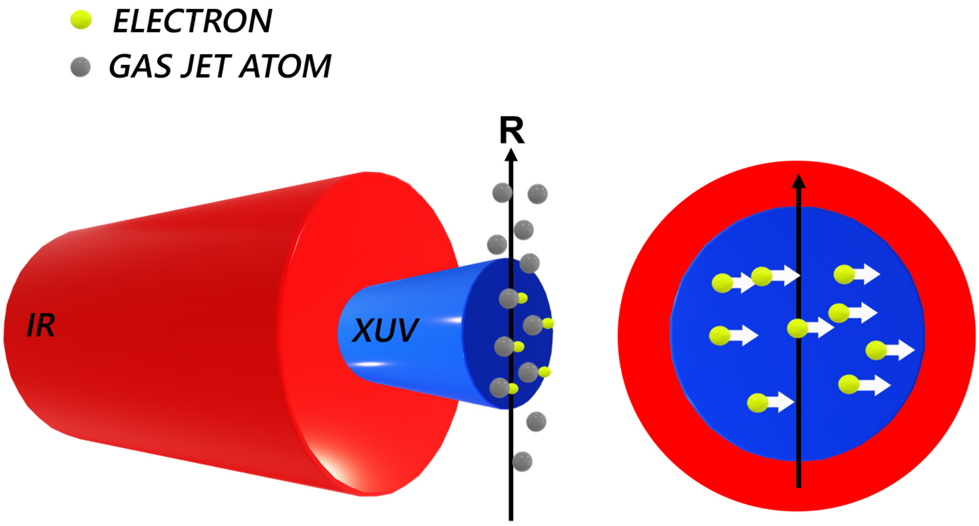

FIGURE 1.9: Schematic representation of the interaction between: a gas jet of atoms, grey spheres, that emit photo-electrons, yellow sphere; an IR field, in red; and an XUV field, in blue. The photo-electrons are emitted in different position of the XUV field and propagate with a velocity distribution observed only among the same direction of the polarization of the fields.

Up to our knowledge, both the great majority of theoretical discussion from experimental data and, as a consequence, all the reconstruction algorithm have always disregarded these effects.
However, the need for scaling down the experimentally available temporal resolution imposes a careful study over these ensemble effects to predict their impact on real photo-electron traces and the algorithm's reconstruction reliability.

As a reasonable starting assumption, we can say that within the interaction zone, usually of the order of hundreds-μm, the gas jet density is homogeneous so that we can focus only on ensemble effects caused by the fields profiles.
Then, we can divide the ensemble effects caused by non-flat fields profiles in two main classes:

a) *Average Ensemble Emission Effects*:
The photo-electron is emitted in a certain position of the XUV field profile at a certain time. Both the XUV and the IR have a well-defined amplitude value as a function of time. As a result, the recorded photo-electron trace is an average over all the possible emission positions.

b) *Average Ensemble Propagation Effects*:
After the emission, the photo-electron propagates, with a certain initial velocity distribution, over a time-varying IR-field profile. Therefore, its final velocity state, and so its final energy distribution, is the result of an effective field, function of the initial velocity, felt by the electron during its journey towards the detector.

The latter effect is much less relevant than the former.
In order to understand the impact of the second effect, let us use the following ballpark, but effective, argumentation. Let us consider a reasonable experimental condition in which we have: a certain XUV attosecond pulse with its own spatial-profile; a "classical" photo-electron emitted in a particular position of the XUV profile with a reasonable velocity distribution centred at 1 atomic unit, around $1/136$ c, where c is the speed of light; an IR that lasts about 10 fs and has a profile of radius in the order of 100 μm. In the "worst" case scenario, the electron is emitted by the XUV at the rising edge of the IR. Therefore it feels an IR field for roughly 20 fs, after that the streaking field disappear as well as its impact on the electron final energy distribution.

As a matter of fact, the velocity variations induced by an IR-field with an intensity around 10^{13} $\frac{W}{cm^2}$, is less than 5%, therefore, our classical electron propagates at an almost constant speed.
Hence, in 20 fs, an electron with constant velocity $1/136$ c propagates a length of 60 nm, which is three orders of magnitude below the chosen IR-radius, as a consequence, the IR felt by our photo-electron during all the interaction is mostly equal to the value at its emission position.

1.4 Motivation of the work

In this thesis work, I will present the study of ensemble effect on streaking traces by averaging over different photo-electron emission regions of the XUV-IR spatial profiles, as discussed in the previous section.

The streaking traces have been simulated with a two-color interaction programme, that I have personally written in Matlab. The programme is based on the theoretical results of strong-field interaction, presented thoroughly in the next chapter. The streaking traces have been, then, analyzed with the previously discussed reconstruction algorithm ePIE to test its robustness.

The motivation behind this work is, then, to investigate the impact of this unprecedentedly studied ensemble effects on the reconstruction capability of a widely used reconstruction algorithm like ePIE.
The relevance of this work is to understand which is the limit, induced by ensemble effect, of our currently available temporal accuracy in extracting sample's physical proprieties from a real attosecond streaking experiment. If those ensemble effects will results to be a bottleneck in scaling down the available experimental temporal resolution, in the future strategies to overcome this non-idealities can be found in data post-processing, similarly to what has been done in the work by Gaumnitz and co-workers for angular effects [23].

Chapter 2

Theory of semi-classical strong field interaction

LIGHT matter interaction is an extremely broad topic which embraces many fields of Physics.

In nature, both light and matter are profoundly described by the laws of quantum mechanics. However, a semi-classical approach often gives, already, an accurate description, especially when intense laser fields are involved.

This second chapter is organized as an ab-initio theoretical discussion on semi-classical strong field interaction physics. In the following pages, I have tried to keep the focus on electron photo-ionization and to provide only the most relevant tools for a fundamental understanding of photo-electron two-color spectroscopy. For the sake of simplicity, mathematical derivations are given in Appendix A and Appendix B.

2.1 Light matter interaction framework

As in any semi-classical theory, light is treated as a classical field, while the matter is described by quantum mechanics formalism.
An introduction to the fundamentals of light-matter interaction can be found in [24].
Let us now schematize the *strong field* semi-classical framework:

Matter: Single Active Electron

In our context of strong-field interaction, the systems under investigation are solids, molecules, single atoms, and free electrons, all described in a *non-relativistic framework*.

To keep the discussion as simple as possible, I am going to focus on a *single active electron* formulation (SAE) for matter. In this case, the electron is a quantum state[1] $|\psi\rangle$ which evolves according to the Shrödinger's equation,

$$\hat{H}\,|\psi\rangle = i\hbar\frac{\partial}{\partial t}\,|\psi\rangle \tag{2.1}$$

where $\hat{H}$ is the light matter interaction Hamiltonian, which is written as:

$$\hat{H} = \frac{1}{2m}(\hat{\mathbf{p}} + e\mathbf{A})^2 - e\phi \qquad (SI) \tag{2.2}$$

with $\hat{\mathbf{p}}$ the momentum operator, $(\mathbf{A}, \phi)$ the electromagnetic field four-vector potential, and e the *modulus* of the electron charge, or *elementary charge*.

Light: Classical Field

Light is treated, instead, as a classical object, described by the microscopic Maxwell's equations:

$$\begin{aligned} \nabla \times \mathbf{E} &= -\frac{\partial}{\partial t}\mathbf{B} & \qquad \nabla \cdot \mathbf{E} &= \frac{\rho}{\epsilon_0} \\ \nabla \times \mathbf{B} &= \frac{1}{c_0^2}\frac{\partial}{\partial t}\mathbf{E} + \mu_0\mathbf{J} & \qquad \nabla \cdot \mathbf{B} &= 0 \end{aligned} \tag{2.3}$$

where $(\mathbf{E}, \mathbf{B})$ is the electromagnetic field, while $(\rho, \mathbf{J})$ are the sources, respectively the density of charges and the density of current.
Light, or more precisely, an electromagnetic field can propagate in space as a wave and can interact with charged matter. This interaction goes in both senses, i.e. light changes matter and matter can change light.
Indeed, light can be absorbed, can scatter, or can be generated by matter, for example through time-fluctuations of distribution of charge[2], an oscillating dipole [1].

---

[1] Clarifications on Dirac notation are presented and discussed in Appendix A

[2] See also "The dipole radiation" @www.myquantumreality.org

The dipole radiation is one of the most studied phenomena that connect the quantum description of matter, single electron in our case, with the electromagnetic field.
The relation that connects this two realms is:

$$\rho(\mathbf{r}, t) = -e|\psi(\mathbf{r}, t)|^2 \tag{2.4}$$

where ψ is the electron wave function.

In fact, it can be shown [1], that in the *dipole approximation*[3] the field generated can be written as:

$$\mathbf{E}(\mathbf{r}, t) = \int_{-\infty}^{+\infty} d\omega \frac{\omega^2}{4\pi\epsilon_0 r}(\mathbf{n} \times \tilde{\mathbf{d}}(\omega) \times \mathbf{n}) e^{i\omega(t-\frac{r}{c_0})} + c.c. \tag{2.5}$$

where r is the modulus of the position $\mathbf{r}$, $\mathbf{n}$ is its normalized vector, and $\tilde{\mathbf{d}}$ is the Fourier transform of the *electric dipole* defined as:

$$\tilde{\mathbf{d}}(\omega) = \int_{-\infty}^{+\infty} \mathbf{d}(t) e^{-i\omega t} dt \tag{2.6}$$

$$\mathbf{d}(t) = \int_{\mathcal{R}^3} \mathbf{r}\rho(\mathbf{r}, t) d\mathbf{r} \tag{2.7}$$

If we now use Eq. (2.4) then, the classical charge distribution become:

$$\begin{aligned} \mathbf{d}(t) = -e \int_{\mathcal{R}^3} \mathbf{r}|\psi|^2 d\mathbf{r} = -e \int \mathbf{r}\psi^*(\mathbf{r}, t)\psi(\mathbf{r}, t) d\mathbf{r} = -e \int \mathbf{r} \langle\psi|\mathbf{r}\rangle \langle\mathbf{r}|\psi\rangle \, d\mathbf{r} = \\ = -e \int \langle\psi| \hat{\mathbf{r}} |\mathbf{r}\rangle \langle\mathbf{r}|\psi\rangle \, d\mathbf{r} = -e \langle\psi| \hat{\mathbf{r}}(\int |\mathbf{r}\rangle \langle\mathbf{r}| \, d\mathbf{r}) |\psi\rangle = -e \langle\psi| \hat{\mathbf{r}} |\psi\rangle \end{aligned}$$

where $\hat{\mathbf{r}}$ is the position operator, and we have exploited its completeness propriety[4].
As a result:

$$\boxed{\mathbf{d}(t) = -e \langle\psi| \hat{\mathbf{r}} |\psi\rangle} \tag{2.8}$$

In our semi-classical framework, this dipole expectation value plays a key role in many physical discussion, some of them later presented.

---

[3] Following the derivation the dipole approximation means that we are expanding the source spatial dependence, and we are stopping at the zero order. This approximation is supported in the, so called, far region.

[4] See Appendix A. In synthesis we have used the fact ($\int |\mathbf{r}\rangle \langle\mathbf{r}| \, d\mathbf{r}) = \hat{I}$, with $\hat{I}$ identity operator

In synthesis, any semi-classical theory aims to make predictions on the energy exchange between light and matter:

$L \rightarrow Q$) The electromagnetic field effects on quantum states, e.g. photo-ionization process started by weak extreme-ultraviolet light(XUV) and driven by an intense infrared (IR).

$Q \rightarrow L$) The effect of the quantum state dynamics on the electromagnetic field, e.g. the generation of extreme ultraviolet light (XUV) from an infrared light-stimulated atomic antenna (HHG).

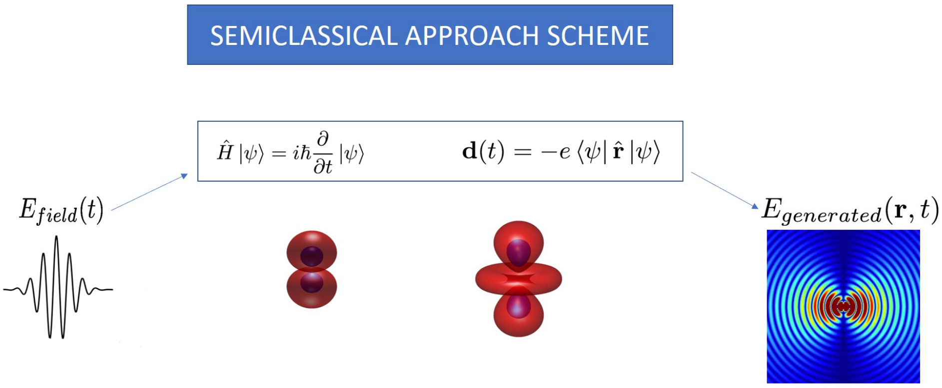

FIGURE 2.1: Example of a possible scheme in the semi-classical framework, in the blue box the quantum mechanical description is needed, while outside classical field theory can be used. In this simple case, we are interested in the generation of light by an atomic system, which behaves as an atomic antenna.

In the following, I will focus on describing the interaction between an atomic system and an electromagnetic field, from the point of view of the quantum system ($L \rightarrow Q$) deriving ab initio as much as possible, and when necessary, introducing models. This will lead us through a self-consistent path, from the general S-Matrix approach and propagators formalism to the Strong Field Approximation (SFA), upon which the simulation software I am presenting in Chapter 3 is based.
The complementary efforts of evaluating the effects of matter on the field ($Q \rightarrow L$), e.g. generation, can be easily discussed once it is known the associated time-varying dipole $\mathbf{d}$, Eq. (2.8), which is tackled in ($Q \rightarrow L$). Therefore, even if I will not enter the same theoretical details, strong-field processes, like HHG generation, where an intense IR triggers the XUV generation, can be easily described with the same formalism and analogous considerations. One has "just" to compute $\mathbf{d}$ and then to pass it to Eq. (2.3).

2.2 Time Dependent Shrödinger Equation (TDSE) solution

The most direct, and often harder, way of solving a quantum physics problem is trying to find exact solutions of Eq. (2.1).

Our objective is to describe a single electron in a single state, hence, neglecting quantum level resonances, that feels both the Coulomb interaction, V_C, from its parent ion, and an external electromagnetic field, under the dipole approximation $\mathbf{E}(\mathbf{r}, t) = \mathbf{E}(t)$ [1].
As a consequence, the validity of all the following theoretical discussion is limited by the field wavelength, λ, $\lambda << a$ where a is the typical atomic dimension, $a \approx 0.1$ nm, but also by the field intensity, as nicely schematize in Figure 2.2.

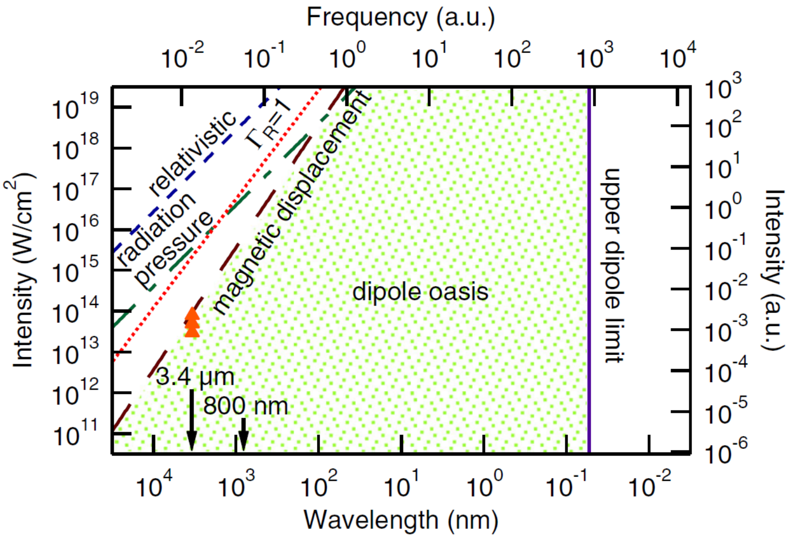

FIGURE 2.2: Region of validity of the dipole approximation: Dipole Oasis zone by [25]

From now on, *atomic units* will be used, for two main reasons:
First, atomic units allow an immediate insight on quantum scales, in fact, for instance, 1 a.u. of velocity is $\frac{1}{136}$ of the speed of light, 1 a.u. of times is approximately 23 as.
Second, atomic units are widely used in literature so that an easy check can be performed with the results.
Third, computations are generally better.
A formal introduction to atomic units is presented in Appendix C.

Let us now consider the Shrödinger equation for the single electron:

$$\boxed{\hat{H}\left|\psi\right\rangle = i\frac{\partial}{\partial t}\left|\psi\right\rangle} \qquad (a.u.) \tag{2.9}$$

In the Shrödinger picture, Eq. (2.9) has the following exact solution:

$$|\psi, t\rangle = |\psi(t)\rangle = e^{-i\int_{t_0}^{t}\hat{H}(t')dt'}\,|\psi(t_0)\rangle \tag{2.10}$$

where we are using the advanced tools of propagators [24], which will lead us to the Feynman path integral approach, and the Dirac notation [24] for quantum states.

Without entering into details, postponed in Appendix A, a propagator is an operator which gives the exact time evolution of a generic quantum state, provided that we define the operator $e^{\hat{F}}$ as $\sum \frac{1}{n!}\hat{F}^n$.

$$e^{\hat{F}} := \sum \frac{1}{n!}\hat{F}^n$$

Eq. (2.10) can be used for the calculation of Volkov states or the unperturbed hamiltonian states, both later discussed. Thus, a different shape and methodology should be followed.

In our simple semiclassical light-matter interaction framework, the single electron hamiltonian is written as:

$$\hat{H} = \frac{1}{2}(\hat{\mathbf{p}} + \mathbf{A}(t))^2 + V_C = -\frac{1}{2}\nabla^2 + V_C + \hat{\mathbf{r}}\cdot\mathbf{E}(t) \tag{2.11}$$

where the equivalence between the two hamiltonians holds for gauge invariance of the electromagnetic field. The former term is the *velocity gauge* hamiltonian, the latter is known as the *length gauge* hamiltonian, which are equivalent as proved[5] in [26]. As a matter of fact, everything is fine, provided that we can neglect the spatial dependence of the field, otherwise the length gauge hamiltonian cannot be used [26].

$$\hat{H}^{(LENGTH)} = -\frac{1}{2}\nabla^2 + V_C + \hat{\mathbf{r}}\cdot\mathbf{E}(t) \tag{2.12}$$

$$\hat{H}^{(VELOCITY)} = \frac{1}{2}(\hat{\mathbf{p}} + \mathbf{A}(t))^2 + V_C \tag{2.13}$$

The gauge invariance of both Maxwell and Shrödinger equations is a fundamental discussion that must be taken into account when moving between gauges [27, 26], the details are presented in Appendix A.

The main result is a rule that allow the "jump" between gauges:

$$\boxed{|\psi\rangle^{(LENGTH)} = e^{+i\hat{\mathbf{r}}\cdot\mathbf{A}}\,|\psi\rangle^{(VELOCITY)}} \tag{2.14}$$

Therefore, the wavefunction that solves Eq. (2.12) differs by a global phase with respect to Eq. (2.13), this result is fundamental to construct a proper gauge invariant theory.

Thanks to Eq. (2.14), once we have solved the problem in a certain gauge, no gauge inconsistency can arise.

---

[5] See also, On Light Matter Interaction @myquantumreality.org

Let us now start to make acquaintance with propagators formalism in quantum mechanics starting with a trivial discussion:

Hydrogenoid atom ground state solution

If the external field is zero, then the Eq. (2.9) becomes:

$$\hat{H}_0 \left|\psi\right\rangle = i\frac{\partial}{\partial t}\left|\psi\right\rangle \tag{2.15}$$

where $\hat{H}_0 = \frac{1}{2}\hat{\mathbf{p}}^2 + V_C$, with $V_C = -\frac{Z}{|\mathbf{r}|} = -\frac{Z}{r}$. Since $\hat{H}_0$ does not depend on time, then Eq. (2.10) becomes:

$$\left|\psi(t)\right\rangle = e^{-i\hat{H}_0(t-t_0)}\left|\psi(t_0)\right\rangle \tag{2.16}$$

The exponential operator is often indicated as:

$$\hat{U}_0 = e^{-i\hat{H}_0(t-t_0)} \tag{2.17}$$

For instance, the ground state eigensolution of Eq. (2.15) is:

$$\hat{H}_0 \left|0\right\rangle = E_0 \left|0\right\rangle$$

where $E_0 = -I_P$, with I_P the ionization potential. In general, we can say $I_P \approx \frac{1}{2n^2}Z^2$ (a.u.) [27] or $I_P \approx \frac{1}{2n^2}27.2Z^2$ eV, where Z is the atomic number and n is the principal quantum number.
If we start from the ground state, as an initial condition, then the temporal wavefunction evolution takes the well-known form:

$$\left|\psi(t)\right\rangle = \left|0\right\rangle e^{iI_P(t-t_0)} \tag{2.18}$$

Due to the completeness of the solution space, a generic state can be constructed by eigenstates superposition, adding as an exponential factor the correct time evolution factor.

2.2.1 Free electron in electromagnetic field: Volkov States

In order to further fix the ideas, and to introduce some fundamental concepts, later used, it is worthwhile to solve the single free electron propagation problem under the influence of an external electromagnetic field. This is particularly useful in any physical situation in which an electron is freed from its parent ion and propagates in space before being detected or recombining, like in the high-order harmonics generation process or the two-color interaction, both discussed later in this chapter.

In *velocity gauge* the hamiltonian for the free particle is:

$$\hat{H}_F = \frac{1}{2}(\hat{\mathbf{p}} + \mathbf{A}(t))^2 \tag{2.19}$$

The objective is to find the quantum states which solve:

$$\hat{H}_F \left|\psi\right\rangle = i\frac{\partial}{\partial t}\left|\psi\right\rangle \tag{2.20}$$

This problem can be solved rapidly with the propagator formalism, see Appendix A.2 or [27].

By introducing $\hat{U}_V(t, t_0)$ the time evolution operator, that, applied on a known initial state $\left|\psi(t_0)\right\rangle$, at a defined time t_0, evolves it into $\left|\psi(t)\right\rangle$:

$$\left|\psi(t)\right\rangle = \hat{U}_V(t, t_0)\left|\psi(t_0)\right\rangle \tag{2.21}$$

then we can write Eq. (2.20) as:

$$\hat{H}_F\hat{U}_V(t, t_0)\left|\psi(t_0)\right\rangle = i\frac{\partial}{\partial t}\hat{U}_V(t, t_0)\left|\psi(t_0)\right\rangle$$

After few steps, presented in details in Appendix A.2, the solution is:

$$\begin{aligned}\left|\psi(t)\right\rangle &= e^{-i\int_{t_0}^{t}\frac{1}{2}(\hat{\mathbf{p}}+\mathbf{A})^2}\left|\psi(t_0)\right\rangle\\ \hat{U}_V &= e^{-i\int_{t_0}^{t}\frac{1}{2}(\hat{\mathbf{p}}+\mathbf{A})^2}\end{aligned}$$

Thus, provided that we known the initial state, we have our generic solution.

To be more general, we can exploit the completeness of momentum space achieving:

$$\left|\psi(t)\right\rangle = \int_{\mathcal{R}^3}\left\langle\mathbf{p}|\psi(t)\right\rangle\left|\mathbf{p}\right\rangle d^3p \tag{2.22}$$

where $\left\langle\mathbf{p}|\psi(t)\right\rangle$ is:

$$\left\langle\mathbf{p}|\psi(t)\right\rangle = \left\langle\mathbf{p}\right| e^{-i\int_{t_0}^{t}\frac{1}{2}(\hat{\mathbf{p}}+\mathbf{A}(t))^2}\left|\psi(t_0)\right\rangle \tag{2.23}$$

As a consequence,

$$\left\langle\mathbf{p}\right| e^{-i\int_{t_0}^{t}\frac{1}{2}(\hat{\mathbf{p}}+\mathbf{A}(t'))^2dt'} = \left\langle\mathbf{p}\right| e^{-i\int_{t_0}^{t}\frac{1}{2}(\mathbf{p}+\mathbf{A}(t'))^2dt'} \tag{2.24}$$

where now $\mathbf{p}$ is the eigenstate associated to $\left|\mathbf{p}\right\rangle$.

Therefore, defined S, the semi-classical action as:

$$S(t, t_0) = \int_{t_0}^{t}\frac{1}{2}(\mathbf{p}+\mathbf{A}(t'))^2dt' \tag{2.25}$$

we can finally obtain a more usable form for a generic state time-evolution, $\left|\psi(t_0)\right\rangle$, driven by an external electromagnetic field:

$$\left|\psi(t)\right\rangle = \int\left\langle\mathbf{p}|\psi(t_0)\right\rangle e^{-iS(t,t_0)}\left|\mathbf{p}\right\rangle d^3p \tag{2.26}$$

The final solution can be seen as the decomposition of the initial state in the complete set of momentum eigensolution $\left|\mathbf{p}\right\rangle$, with time-dependent weights, or, equivalently, as the decomposition in peculiar states, namely *Volkov states* [27, 12], weighted by time independent coefficients.

$$|\Psi_{Volkov}(t)\rangle = e^{-iS(t,t_0)}\,|\mathbf{p}\rangle \tag{2.27}$$

$$|\psi(t)\rangle = \int \langle\mathbf{p}|\psi(t_0)\rangle\,|\Psi_{Volkov}(t)\rangle\,d^3p$$

The wavefunction associated to the Volkov states, Eq. (2.27), can be calculated by projecting it in the position space, see Appendix A:

$$\Psi_{Volkov}(\mathbf{r},t) = \langle\mathbf{r}|\Psi_{Volkov}(t)\rangle = \frac{1}{(2\pi)^{\frac{3}{2}}}e^{-iS(t,t_0)}e^{i\mathbf{p}\cdot\mathbf{r}} \tag{2.28}$$

where it has been used the fact that $\langle\mathbf{r}|\mathbf{p}\rangle = (2\pi)^{-\frac{3}{2}}e^{i\mathbf{p}\cdot\mathbf{r}}$.

Therefore, the solution of Eq. (2.20) is

$$\psi(\mathbf{r},t) = \frac{1}{(2\pi)^{\frac{3}{2}}}\int \phi(\mathbf{p},t_0)e^{-iS(t,t_0)}e^{i\mathbf{p}\cdot\mathbf{r}}d^3p \tag{2.29}$$

where $\phi(\mathbf{p},t_0) = \langle\mathbf{p}|\psi(t_0)\rangle$ is the initial momentum distribution at time t_0 for the electron.

In Appendix B, I have analyzed in depth the solution of Eq. (2.29) and solved it for an initially Gaussian distribution in the momentum space. By comparing the equations, it arises a deep analogy with the propagation of a Gaussian light pulse in a dispersive medium. In the following, I discuss and present the main results and the most significant physical insights that can be obtained following Appendix B:

i) Even in absence of an external field potential $\mathbf{A} = 0$, a free electron broads its position uncertainty in time[6].

ii) The initial momentum distribution is correlated to the initial spatial dispersion, due to the Heisenberg uncertainty principal. This implies that, if we have an initial localization of the electron with an uncertainty of 1 a.u. (0.05 nm), the uncertainty in momentum, and hence in absence of field, in velocity is of the same order, 1 a.u. . This means that the velocity uncertainty of an electron emitted by an atom is of the order of $\frac{1}{136}$ the speed of light. This result, clearly set boundaries on the field intensity, $< 10^{13}\frac{W}{cm^2}$, that can be accepted in a non-relativistic discussion.

iii) The overall effect of the electromagnetic field on the electron propagation is a phase term, which moves the electron center of mass and creates, what could be called, *electron chirp* which means that there is an inhomogeneous spatial distribution of momentum, as in the case of an optical pulse in which

---

[6] This can be explained easily with a classical analogy, by claiming that the initial distribution in momentum implies that the electron can propagate following different paths, and so, as the time goes by, the uncertainty in momentum create a dispersed wavefunction.

the frequency has a non uniform time distribution. This fact has consequences in the inherited chirp of an attosecond pulse. Lastly, the field has no effect on the electron spatial dispersion.

To conclude, in the velocity gauge it holds $\mathbf{p} = \mathbf{v}(t) - \mathbf{A}(t)$, thanks to that we achieve an equivalent formula, often reported in literature, for Volkov states:

$$\Psi_{Volkov}(\mathbf{r}, t) = \frac{1}{(2\pi)^{\frac{3}{2}}} e^{-iS(t,t_0)} e^{i(\mathbf{v}(t)-\mathbf{A}(t))\cdot\mathbf{r}}$$

where,

$$S(t, t_0) = \frac{1}{2} \int_{t_0}^{t} dt' (\mathbf{v}(t_0) - \mathbf{A}(t_0) + \mathbf{A}(t'))^2$$

Clearly, this whole derivation could have been performed in the *lenght gauge*, or we can simply exploit Eq. (2.14):

$$\Psi_{Volkov}{}^{(V)}(\mathbf{r}, t) = \frac{1}{(2\pi)^{\frac{3}{2}}} e^{-iS(t,t_0)} e^{i\mathbf{p}\cdot\mathbf{r}}$$
$$\Psi_{Volkov}{}^{(L)}(\mathbf{r}, t) = \frac{1}{(2\pi)^{\frac{3}{2}}} e^{-iS(t,t_0)} e^{i(\mathbf{p}+\mathbf{A}(t))\cdot\mathbf{r}}$$

Now we are ready to face a more complex configuration, in which, in addition to the field we also have a Coulomb potential.

2.2.2 Atom in electromagnetic field: S-Matrix amplitude

Let us go back to the original problem, we had a single electron, in a well-defined atomic eigenstate $|\psi(t_0)\rangle$, who feels both a *static* Hydrogenoid-Coulomb field, V_C, which can be described by Maxwell equation[7], and an electromagnetic (e.m.) wave field, in the dipole approximation.
To fix the ideas, let us start in the *length gauge*.

$$\hat{H} = \frac{1}{2}\hat{\mathbf{p}}^2 + V_C + \hat{\mathbf{r}} \cdot \mathbf{E}(t)$$

In order to reach a better form for Eq. (2.10), our hamiltonian can be partitioned in two terms:

$$\hat{H} = \hat{H}_0 + \hat{H}_I(t) \tag{2.30}$$

where $\hat{H}_0 = -\frac{1}{2}\nabla^2 + V_C$ and $\hat{H}_I = \hat{\mathbf{r}} \cdot \mathbf{E}(t)$.
It can be proved, through the Dyson's equations whose formal discussion is presented in Appendix A.2, that the exact solution of Eq. (2.1), as presented in [12, 27, 28], can also be written as:

$$|\psi(t)\rangle = -i \int_{t_0}^{t} dt' e^{-i\int_{t'}^{t} \hat{H}(t'')dt''} \hat{H}_I(t') e^{-i\int_{t_0}^{t'} \hat{H}_0(t'')dt''} |\psi(t_0)\rangle + e^{-i\int_{t_0}^{t} \hat{H}_0(t'')dt''} |\psi(t_0)\rangle \tag{2.31}$$

---

[7] See also, On light matter interaction @www.myquantumreality.org

or equivalently,

$$|\psi(t)\rangle = -i\int_{t_0}^{t} dt' e^{-i\int_{t'}^{t}\hat{H}_0(t'')dt''}\hat{H}_I(t')e^{-i\int_{t_0}^{t'}\hat{H}(t'')dt''}|\psi(t_0)\rangle + e^{-i\int_{t_0}^{t}\hat{H}_0(t'')dt''}|\psi(t_0)\rangle \tag{2.32}$$

This *exact solution* of the problem is the manifestation of something extremely curious and interesting.

Indeed, the solution to Eq. (2.1), which previously was simply written as Eq. (2.10), can now be regarded as *superposition of different quantum paths*, each one of them has a peculiar interaction time t'.
In other words, each quantum path is made by an initial evolution without the em. field, described by $\hat{H}_0$; a "kick" from that field, $\hat{H}_I(t')$, at an arbitrary time that uni-vocally characterizes the path t'; and by a final evolution driven by both the field and the Coulomb potential, $\hat{H}$. As shown by Eq. (2.32) this process is completely time-reversible, i.e. can also occur in the opposite order.

Equation (2.31) is not easy to handle, however, one can imagine using it as the starting point for numerical calculation [27], more advanced discussion [29] or several approximations [12]. In general, one can imagine to project Eq. (2.31) in a certain continuum state $|v\rangle$, so that $c_v^2(t) = |\langle v|\psi\rangle|^2$ is the probability amplitude to find at a certain time t, the electron projected in the $continuum$.

$$c_v(t) = -i\int_{t_0}^{t} dt' \langle v| e^{-i\int_{t'}^{t}\hat{H}(t'')dt''}\hat{H}_I(t')e^{-i\int_{t_0}^{t'}\hat{H}_0(t'')dt''}|\psi(t_0)\rangle + \langle v| e^{-i\int_{t_0}^{t}\hat{H}_0(t'')dt''}|\psi(t_0)\rangle \tag{2.33}$$

The latter term is not so interestin, in fact, since $\psi_0(t_0)$ is an atomic eigenstate and $\hat{H}_0$ is time independent:

$$\langle v| e^{-i\int_{t_0}^{t}\hat{H}_0(t'')dt''}|\psi_0(t_0)\rangle = e^{-iE_0(t-t_0)}\langle v|\psi_0(t_0)\rangle$$

then this object does not contain any information about the transition, and, for this reason, is usually disregarded. This is theoretically justified if one can find an orthogonal set of continuum states $|v\rangle$ with respect the bounded states.

On the other hand, the first term of Eq. (2.33) depends on the external field. Therefore, it represents the probability that an initial state, $|\psi(t_0)\rangle$, is projected by the field on a continuum level $|v\rangle$ [12, 27], or the ionization probability. This term is called *time reversed S-matrix amplitude*, a_v,

$$\boxed{a_v(t) = -i\int_{t_0}^{t} dt' \langle v| e^{-i\int_{t'}^{t}\hat{H}(t'')dt''}\hat{H}_I(t')e^{-i\int_{t_0}^{t'}\hat{H}_0(t'')dt''}|\psi(t_0)\rangle} \tag{2.34}$$

Eq. (2.34) is a fundamental result in strong field physics, and it is starting point of many discussions, approximations, and models, like the *Strong Field Approximation* (SFA), discussed below.
As a final remark, Eq. (2.34) represents both the solution in length gauge, if $\hat{H}_I = \hat{\mathbf{r}}\cdot\mathbf{E}$, but also in velocity gauge, when $\hat{H}_I = \mathbf{A}(t)\cdot\hat{\mathbf{p}} + \frac{1}{2}\mathbf{A}^2(t)$.

2.3 Strong Field Approximation (SFA)

SFA, or Keldysh-Faisal-Reiss theory, together with its extensions, is a milestone of modern physics and it is the starting point for the understanding of many physical phenomena in the field of *Attosecond Science*, like the two-color photoemission spectroscopy.

SFA has few flaws and limits, as it will be discussed later in section 2.4, especially in describing with accuracy the ionization process. This is the reason why some adjustment and extension of the theory are needed in order to make more accurate predictions in strong-field interaction physics.

In the following, I will present an elegant formulation of SFA, exploiting the result of Eq. (2.34). One of the greatest advantages of SFA is that it does not need any assumption on the interaction strength concerning the binding potential, as one would need, instead, in perturbation theory, neither any strict information on the field(s) wavelength. This allows huge flexibility and generality in the description [12], at least in the "Dipole Oasis" of Figure 2.2.
As a matter of fact, by following SFA theory, we are capable of extracting relevant information, that is used, for instance, to model the High Harmonics Generation (HHG) process[27], which is one of the possible ways of to generate attosecond pulses, or to describe the photo-ionization processes [30].

As already said, the solution to Eq. (2.34) can be interpreted as a sequence of operators acting on $|\psi(t_0)\rangle$, as discussed in [12].
In other words, the S-Matrix describes the exact probability amplitude to find the electron in a certain free state due to the interference of all possible ionization paths, each occurring at a different time t', and the subsequent contributions of both the external field and the Coulomb potential [12, 27].

Now, the *fundamental* idea, and approximation, behind SFA is to *neglect the effect of Coulombian interaction* in the latter S-Matrix evolution, after the ionization. Thus,

$$a_v^{(SFA)} = -i \int_{t_0}^{t} dt' \, \langle v| \, e^{-i\int_{t'}^{t} \hat{H}_F(t'')dt''} \hat{H}_I(t') e^{-i\int_{t_0}^{t'} \hat{H}_0(t'')dt''} \, |\psi(t_0)\rangle \tag{2.35}$$

with,

$$\hat{H} \to \hat{H}_F = \frac{1}{2}\hat{\mathbf{p}}^2 + \hat{\mathbf{r}} \cdot \mathbf{E}(t) = \frac{1}{2}(\hat{\mathbf{p}} + \mathbf{A}(t))^2 \tag{2.36}$$

It can be shown, as mentioned in [29] and proved in Appendix A, that the SFA approximation is just the first order of an expansion for the S-matrix amplitude.

Due to gauge invariance of the original problem, one could think to use, in principle, both *length gauge* and *velocity gauge* by selecting freely $\hat{H}_F$ and $\hat{H}_I$.
According to [12], this was a common approach in the literature, which have led to some inconsistency.
In principle, one could think to mix the gauges without introducing any changes in the physics of the problem. However, this is not true.
Indeed, due to the strong-field approximation, as extensively discussed by [12, 31], this approach leads to a theory that seems to be *gauge variant*!

Hence, adjustments by using Eq. (2.14), must be taken to preserve the invariance, as shown by Faisal in 2007 [29].

In the following, I am going to derive the SFA amplitude in the length gauge by using the proper gauges transformations, this result coincides with the Faisal's gauge invariant result.
As discussed by many authors in the recent years, like [32], the result of the *length gauge*, which was already known since the development of strong field theory, is, indeed, the right gauge independent result.

SFA in lenght gauge

In length gauge:

$$\hat{H}_0 = \frac{1}{2}\hat{\mathbf{p}}^2 + V_C \qquad \hat{H}_I^{(L)} = \hat{\mathbf{r}} \cdot \mathbf{E}(t) \qquad \hat{H}_F^{(L)} = \frac{1}{2}\hat{\mathbf{p}}^2 + \hat{\mathbf{r}} \cdot \mathbf{E}(t)$$

By looking at Eq. (2.35) we can imagine selecting as the final states the velocity states $|v\rangle = |\mathbf{v}(t)\rangle$.
So that, $|a_{\mathbf{v}}(t)|^2$ is almost the probability amplitude to find, at a final time t, the electron projected in the plane wave state with velocity **v**, hence with kinetic energy $E_k = \frac{1}{2}v^2$, where v is the modulus of **v**
Let us solve Eq. (2.35), in details:
Our first goal is to solve:

$$\langle \mathbf{v}(t)|\, e^{-i\int_{t'}^{t} \hat{H}_F^L(t'')dt''} = \langle \Phi(t')|^{(L)} \tag{2.37}$$

where $\langle \Phi(t')|^{(L)}$ is a generic state in the length gauge, and t' must be interpreted as a fixed parameter.
Now, $\hat{H}_F$ can be both expressed in length and velocity gauge, so in order to solve the problem in the length gauge we counter-intuitively focus, for the moment, on the velocity gauge, in fact as it will be shown late this approach leads us smoothly to the final result.
So:

$$\langle \mathbf{v}(t)|\, e^{-i\int_{t'}^{t} \hat{H}_F^V(t'')dt''} = \langle \Phi(t')|^{(V)}$$

where, now, $\langle \Phi(t')|^{(V)}$ is a generic state in the velocity gauge.
Thus, by exploiting the momentum space completeness, we can write:

$$\langle \mathbf{v}(t)|\, e^{-i\int_{t'}^{t} \hat{H}_F^{(V)}(t'')dt''} = \int \langle \mathbf{v}(t)|\tilde{\mathbf{p}}\rangle \, \langle \tilde{\mathbf{p}}|\, e^{-i\int_{t'}^{t} \hat{H}_F^{(V)}(t'')dt''} d^3\tilde{p} \tag{2.38}$$

as proved in Eq. (2.24), this is equal to

$$\langle \mathbf{v}(t)|\, e^{-i\int_{t'}^{t} \hat{H}_F^{(V)}(t'')dt''} = \int \langle \mathbf{v}(t)|\tilde{\mathbf{p}}\rangle \, \langle \tilde{\mathbf{p}}|\, e^{-i\int_{t'}^{t} \hat{H}_F^{(V)}(t'',\tilde{\mathbf{p}})dt''} d^3\tilde{p} \tag{2.39}$$

where in the last equation we have fixed the momentum in $\hat{H}_F$.
Our second goal is to evaluate:

$$\langle \mathbf{v}(t)|\tilde{\mathbf{p}}\rangle \tag{2.40}$$

We can define the *velocity operator* $\hat{\mathbf{v}}(t) = \hat{\mathbf{p}} + \mathbf{A}(t)$ as:

$$\hat{\mathbf{v}}(t)\left|\mathbf{v}(t)\right\rangle = \mathbf{v}(t)\left|\mathbf{v}(t)\right\rangle \qquad (\hat{\mathbf{p}} + \mathbf{A}(t))\left|\mathbf{v}(t)\right\rangle = \mathbf{v}(t)\left|\mathbf{v}(t)\right\rangle$$

then, $|\mathbf{v}(t)\rangle$ is a state which is formally equivalent to a peculiar $|\mathbf{p}\rangle$ that satisfies:

$$\hat{\mathbf{p}}\left|\mathbf{v}(t)\right\rangle = \mathbf{p}\left|\mathbf{v}(t)\right\rangle \qquad \hat{\mathbf{p}}\left|\mathbf{p}\right\rangle = \mathbf{p}\left|\mathbf{p}\right\rangle \qquad \mathbf{p} = \mathbf{v}(t) - \mathbf{A}(t)$$

In other word, $|\mathbf{v}(t)\rangle$ is still eigensolution of $\hat{\mathbf{p}}$ and, as a consequence, thanks to the orthonormality of momentum eigenset, we can solve Eq. (2.39)

$$\langle\mathbf{v}|\tilde{\mathbf{p}}\rangle = \delta(\tilde{\mathbf{p}} - \mathbf{p}) = \delta(\tilde{\mathbf{p}} - (\mathbf{v}(t) - \mathbf{A}(t))) \tag{2.41}$$

Finally Eq. (2.38) become:

$$\left\langle\mathbf{v}(t)\right| e^{-i\int_{t'}^{t}\hat{H}_F^{(V)}(t'')dt''} = \left\langle\mathbf{p}\right| e^{-i\int_{t'}^{t}(\mathbf{p}+\mathbf{A}(t''))^2 dt''} \tag{2.42}$$

For momentum conservation, we can write that at the initial instant t', the following relations hold for $\mathbf{v}'(t')$:

$$\mathbf{p} = \mathbf{v}(t) - \mathbf{A}(t) = \mathbf{v}'(t') - \mathbf{A}(t') \qquad \hat{\mathbf{p}}\left|\mathbf{v}'(t')\right\rangle = \mathbf{p}\left|\mathbf{v}'(t')\right\rangle$$
$$\left|\mathbf{v}'(t')\right\rangle = \left|\mathbf{v}(t) + \mathbf{A}(t') - \mathbf{A}(t)\right\rangle$$

Now, since they have the same expectation value in momentum we can interchange the state $|\mathbf{p}\rangle$ with $|\mathbf{v}'(t')\rangle$ achieving the same result of [12],

$$\left\langle\mathbf{v}(t)\right| e^{-i\int_{t'}^{t}\hat{H}_F^{(V)}(t'')dt''} = \left\langle\mathbf{v}'(t')\right| e^{-i\int_{t'}^{t}(\mathbf{p}+\mathbf{A}(t''))^2 dt''} \tag{2.43}$$

or equivalently,

$$\left\langle\mathbf{v}(t)\right| e^{-i\int_{t'}^{t}\hat{H}_F^{(V)}(t'')dt''} = \left\langle\mathbf{v}(t) + \mathbf{A}(t') - \mathbf{A}(t)\right| e^{-iS(t,t')} \tag{2.44}$$

where $S(t,t') = \int_{t'}^{t}(\mathbf{v} - \mathbf{A}(t) + \mathbf{A}(t''))^2 dt''$ is the semi-classical action.

At this point, *a common mistake* is to jump back to Eq. (2.35), but we cannot! In fact, we are still in the *velocity gauge*.
Hence, we must apply the right transformation between gauges.
So since,

$$\left\langle\mathbf{v}(t)\right| e^{-i\int_{t'}^{t}\hat{H}_F^{(V)}(t'')dt''} = \left\langle\Phi(t')\right|^{(V)} \tag{2.45}$$

thanks to Eq. (2.14), we have;

$$\left\langle\Phi(t')\right|^{(L)} = \left\langle\Phi(t')\right|^{(V)} e^{-i\hat{\mathbf{r}}\cdot\mathbf{A}(t')} = \left\langle\mathbf{v}(t) + \mathbf{A}(t') - \mathbf{A}(t)\right| e^{-i\hat{\mathbf{r}}\cdot\mathbf{A}(t')} e^{-iS(t,t')} \tag{2.46}$$

As a result, Eq. (2.35), in the length gauge, has the form:

$$a_{\mathbf{v}}(t)^{(L)} = -i\int_{t_0}^{t} e^{i(I_P(t'-t_0)-S(t,t'))}\left\langle\mathbf{v}(t) + \mathbf{A}(t') - \mathbf{A}(t)\right| e^{-i\hat{\mathbf{r}}\cdot\mathbf{A}(t')}\hat{\mathbf{r}}\cdot\mathbf{E}(t')\left|0\right\rangle dt' \tag{2.47}$$

where it has been assumed, thanks to single active electron approximation (SAE), that the initial state, $|\psi(t_0)\rangle$, is made only be the atomic ground state $|0\rangle$, see

Eq. (2.18). Equation (2.47) is often called *Keldysh amplitude* [27, 33], in agreement with [29].
Before proceeding further, it is useful to explicitly evaluate the bracket of Eq. (2.47). Hence, by exploiting the completeness of position eigenkets $|\mathbf{r}\rangle$, we obtain:

$$\langle \mathbf{v}(t) + \mathbf{A}(t') - \mathbf{A}(t)| e^{-i\hat{\mathbf{r}}\cdot\mathbf{A}(t')}\hat{\mathbf{r}} \cdot \mathbf{E}(t')\,|0\rangle = \\ = \int \langle \mathbf{v}(t) + \mathbf{A}(t') - \mathbf{A}(t)|\mathbf{r}\rangle\, e^{-i\mathbf{r}\cdot\mathbf{A}(t')}\mathbf{r} \cdot \mathbf{E}(t')\,\langle \mathbf{r}|0\rangle\, d^3r$$

The velocity state's projection in position eigenstates is tricky. However, it becomes easier if one uses the result of Eq. (2.41), see also Appendix A.
Calling $\mathbf{v}'(t') = \mathbf{v}(t) + \mathbf{A}(t') - \mathbf{A}(t)$ then,

$$\langle \mathbf{v}'(t')|\mathbf{r}\rangle = \int \langle \mathbf{v}'(t')|\tilde{\mathbf{p}}\rangle\, \langle \tilde{\mathbf{p}}|\mathbf{r}\rangle\, d^3\tilde{p} = \frac{1}{(2\pi)^{\frac{3}{2}}} e^{-i(\mathbf{v}'-\mathbf{A}(t'))\cdot\mathbf{r}} = \frac{1}{(2\pi)^{\frac{3}{2}}} e^{-i(\mathbf{v}-\mathbf{A}(t))\cdot\mathbf{r}} \tag{2.48}$$

where the last equality holds, also, for momentum conservation.
Finally,

$$\langle \mathbf{v'}(t)|\, e^{-i\hat{\mathbf{r}}\cdot\mathbf{A}(t')}\hat{\mathbf{r}} \cdot \mathbf{E}(t')\,|0\rangle = \mathbf{E}(t') \cdot \int \frac{1}{(2\pi)^{\frac{3}{2}}} \mathbf{r} e^{-i(\mathbf{v}-\mathbf{A}(t)+\mathbf{A}(t'))\cdot\mathbf{r}} \psi_0(\mathbf{r}) d^3r \tag{2.49}$$

where we have called $\psi_0(\mathbf{r}) = \langle \mathbf{r}|0\rangle$.

Thanks to these results, Eq. (2.47) assumes its contracted form,

$$a_{\mathbf{v}}(t)^{(L)} = \int_{t_0}^{t} \mathbf{E}(t') \cdot \mathbf{d}(t,t') e^{+i(I_P(t'-t_0)-S(t,t'))} dt' \tag{2.50}$$

where we have defined:

$$\mathbf{d}(t,t') = \langle \mathbf{v}'(t')|\, e^{-i\hat{\mathbf{r}}\cdot\mathbf{A}(t')}\hat{\mathbf{r}}\,|0\rangle = \int \frac{1}{(2\pi)^{\frac{3}{2}}} \mathbf{r} e^{-i(\mathbf{v}-\mathbf{A}(t)+\mathbf{A}(t'))\cdot\mathbf{r}} \psi_0(\mathbf{r}) d^3r \tag{2.51}$$

as the *dipole transition matrix element* between the ground state and a final plane wave state with momentum $\mathbf{p}_f = \mathbf{p} + \mathbf{A}(t')$, where $\mathbf{p}_f = \mathbf{v}'(t')$.
This is the reason why Eq. (2.51) is equivalently written as $\mathbf{d}[\mathbf{p} + \mathbf{A}(t')] = \mathbf{d}(t,t')$, since $\mathbf{v}(t) - \mathbf{A}(t) = \mathbf{p}$.

$$\boxed{\mathbf{d}[\mathbf{p} + \mathbf{A}(t')] = \langle \mathbf{p} + \mathbf{A}(t')|\, \hat{\mathbf{r}}\,|0\rangle = \int \frac{1}{(2\pi)^{\frac{3}{2}}} \mathbf{r} e^{-i(\mathbf{p}+\mathbf{A}(t'))\cdot\mathbf{r}} \psi_0(\mathbf{r}) d^3r} \tag{2.52}$$

From Eq. (2.52), we can finally write the transition amplitude, at time t, from an initial bounded state to a free state with momentum $\mathbf{p}$ as:

$$\boxed{a_{\mathbf{p}}(t)^{(L)} = -i \int_{t_0}^{t} \mathbf{E}(t') \cdot \mathbf{d}[\mathbf{p} + \mathbf{A}(t')] e^{+i(I_P(t'-t_0)-S(t,t'))} dt'} \tag{2.53}$$

with, as before,

$$S(t,t') = \int_{t'}^{t} \frac{1}{2}(\mathbf{p} + \mathbf{A}(t''))^2 dt''$$

As a final remark, in experiments one usually has easier access to the angular probability distribution of electrons ω_ϵ with kinetic energy between ϵ and $\epsilon + d\epsilon$. Thus, since $\epsilon = \frac{1}{2}p^2$, we write:

$$|a_{\mathbf{p}}|^2 d^3p = |a_{\mathbf{p}}|^2 dp d\Omega = \omega_\epsilon d\epsilon d\Omega \qquad d\epsilon = pdp$$

and, so:

$$\omega_\epsilon = p|a_{\mathbf{p}}|^2 \tag{2.54}$$

SFA in velocity gauge

Faisal in [29] proved that the right form in velocity gauge for the SFA amplitude which preserve the gauge invariance is:

$$a_v(t)^{(V)} = -i \int_{t_0}^{t} e^{i(I_P(t'-t_0) - S(t,t'))} \left\langle \mathbf{v}(t) + \mathbf{A}(t') - \mathbf{A}(t) \right| \hat{\mathbf{r}} \cdot \frac{\partial}{\partial t} \mathbf{A}(t') e^{-i\hat{\mathbf{r}}\cdot\mathbf{A}(t')} \left| 0 \right\rangle dt' \tag{2.55}$$

which leads to equivalent result to the one we have previously derived with Eq. (2.47).
Therefore, under some assumption on the initial and final state [32], here not discussed, no gauge ambiguity in the (SFA) is present, neither for the S-matrix higher order of approximation terms [29].

Dipole transition element simple case evaluation

The dipole transition element of Eq. (2.52) plays a key role in photo-emission processes, therefore it is a quantity of great theoretical and experimental interest. As a matter of fact, direct calculations of this object with hydrogenoid wavefunction are a well-established result [2, 34], and can be numerically calculated with a standard computer. More sophisticated models can be also included in this dipole calculation to extend the accuracy of the result, as discussed in the next section.
Let us now consider, for instance, a simple s-shell ground state, with I_P as its ionization potential (e.g. for hydrogen $I_P = \frac{1}{2}$ a.u.), in absence of an external field we have:

$$\mathbf{d}[\mathbf{p}] = \langle \mathbf{p} | \hat{\mathbf{r}} | 0 \rangle = -i \frac{2^{\frac{7}{2}}}{\pi} (2I_P)^{\frac{5}{4}} \frac{\mathbf{p}}{(\mathbf{p}^2 + 2I_P)^3} \tag{2.56}$$

If we turn on the radiation field $\mathbf{E}(t)$, then the dipole transition element, from an s-state to a plane wave takes the form:

$$\mathbf{d}[\mathbf{p} + \mathbf{A}(t')] = -i \frac{2^{\frac{7}{2}}}{\pi} (2I_P)^{\frac{5}{4}} \frac{\mathbf{p} + \mathbf{A}(t')}{((\mathbf{p} + \mathbf{A}(t'))^2 + 2I_P)^3} \tag{2.57}$$

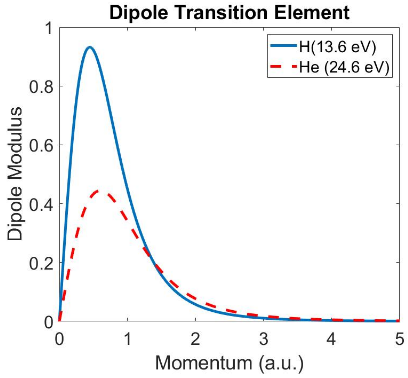

FIGURE 2.3: Numerical evaluation of Eq. (2.56) profile in the momentum space, fixed direction, for Helium(2s) and Hydrogen(1s) at $A(t') = 0$, absence of external field. In that case the momentum is equal to the velocity of the free electron state at every time.

This object, now, has a certain time profile, that will be integrated into Eq. (2.53).

Since **p** is conserved in time, it can be always regard as the final electron velocity after the interaction so when $\mathbf{A}(+\infty) = 0$, in that case $\mathbf{p} = \mathbf{v} - \mathbf{A}(+\infty) = \mathbf{v}$.

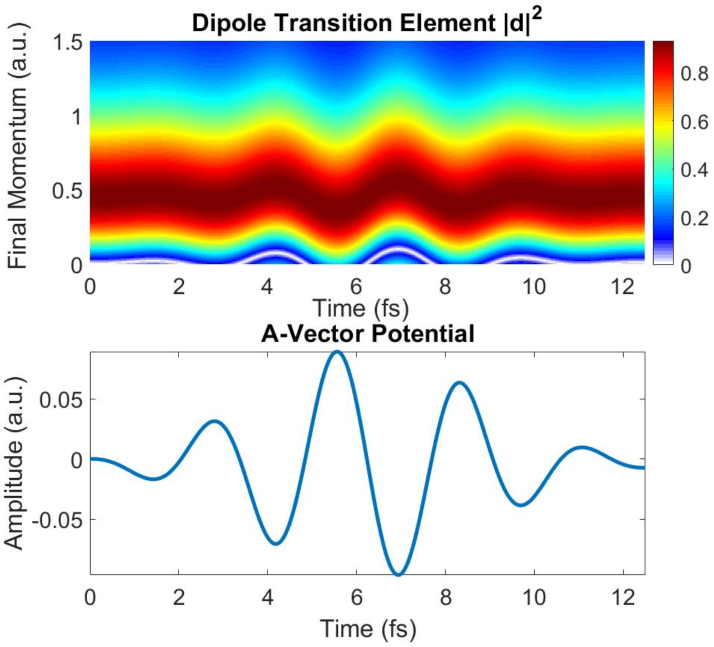

FIGURE 2.4: Numerical evaluation of Eq. (2.57) for 1s atom. At a fixed time t', the field shifts the transition probability to different final state The equation is solved for an external pulse with $I_{peak} \approx 10^{13} \frac{W}{cm^2}$, $\lambda = 800$ nm, for H.

Therefore, at least within SFA, once it is known the dipole transition element for a generic initial state, to use it in Eq. (2.53) we have to perform a simple time-shift of an amount which is given by the field vector potential $\mathbf{A}(t')$.

2.4 Beyond SFA

At this point, before any practical discussion, we must put under questioning the validity of SFA. Although SFA can be seen as the first-order approximation of TDSE exact solution, its theoretical elegance and its wide use in several experimental applications have pushed researchers to find a correction to the standard SFA, rather than dismiss it. This is an active research direction with many models that are periodically tested and discussed, as reported in this excellent 2019 review work [35]. The main SFA flaws can be divided into three main categories:

- *Direct Coulomb potential effect*:
  In Eq. (2.36) we explicitly neglect the Coulomb potential in the latter wavefunction evolution stage. This has a huge impact on the capability of describing the ionization from the parent ion. Therefore, some corrections are needed.

- *Indirect Coulomb potential effect*:
  This is a silent approximation, that was made to derive Eq. (2.53). We implicitly accepted Volkov plane waves to be our final state after the interaction. As discussed later, these objects are not real solutions to the atom-field interaction problem, and, hence, they cannot be the real state in which the electron is projected during the interaction.

- *Many electrons and internal resonance effects*:
  After all, the single active electron (SAE) and the ionization from a single state are both naive portraits of a real multi-electron atom; hence, we expect further effects taking place, see Chapter 12 of [36].

In the following, I will try to sketch, without entering into any formal details the general framework of SFA correction that can be found in the literature. For simplicity, I will remain in a SAE description, neglecting all kinds of electronic correlation effects, which often play just a minor role in the interaction.

2.4.1 Tunneling and Above threshold ionization

Strong Field Approximation tells us the ionization probability from a well-defined bound state to the plane wave continuum states, however, by directly neglecting the presence of the Coulomb potential it cannot provide any information on *how* this process occurs.

$$W_E^{(SFA)}(t) = \int_{\mathbf{R}^3} a_{\mathbf{p}}(t) d\mathbf{p} \tag{2.58}$$

$W_E^{(SFA)}$ is the total ionization probability predicted by SFA, and $a_{\mathbf{p}}(t)$ is taken from Eq. (2.53).

Therefore, to understand whether SFA is an accurate description or not of this total ionization, one must confront Eq. (2.58) with more general theories of ionization [36]. In general, depending on both the laser frequency and its intensity, we can identify three main ionization mechanism:

1) **Multiphoton ionization**:
   Multi-photon ionization is a strong ionization regime in which the electron can absorb multiple photons before escaping in the continuum [12]. If the number of absorbed photons is high enough to bring the electron into a large velocity state, then the multi-photon regime is named *Above Threshold Ionization* (ATI) [37].

2) **Tunnel Ionization**:
   Tunnelling is a purely quantum phenomenon where the electron exploits its ability to pass through the Coulombian potential barrier, which is bent by the electric component of the incident radiation. This second ionization channel was first discussed by Landau and Lifsits [38] by solving the Shrödinger equation in the presence of a strong static electric field. Keldysh later formalized the extension to a time-varying field in 1960 [33].

Keldysh theory of strong-field ionization, which is the seminal work for SFA, is judged as one of the most successful non-perturbative treatment of strong laser-atom interaction [28]. One exceptional achievement is the capability of predicting which ionization channel is the most efficient under certain physical conditions through a simple parameter, γ, called *Keldysh parameter*.

$$\gamma = \frac{\omega}{eE_0}\sqrt{2mI_P} \tag{2.59}$$

where E_0 is the maximum amplitude of the electromagnetic field, ω is the ionizing field frequency, and I_P is the ionization potential for the atom involved in the interaction.
It can be shown that, if $\gamma >> 1$ we are in the *non-adiabatic regime*, in this case, the multi-photon regime is the most efficient ionization channel. Calculations can show that, in this regime, SFA is less accurate in the description [12], and some significant adjustments are often needed [39]. On the contrary, if $\gamma << 1$ we enter the *adiabatic regime* in which tunnel ionization is the main character. In this framework, SFA is widely used with the addition of some coulombian pre-factor to take into account the presence of the tunnelling process. In the adiabatic regime, thanks to SFA, we can easily gain further insights into the zoo of strong-field phenomena, as an outstanding example HHG process, mentioned in Chapter 1.

3) **Direct Ionization**:
   The third case was, historically, one of the first studied ionization mechanism with the advent of Quantum Mechanics.
   Direct ionization takes place when the frequency of the field is big enough to allow the single-photon-ionization process to occur. In this simple case, especially if the field is not so intense[8], SFA can still be used to describe the physical problem adequately, however, the effort is pointless because the same results can be achieved with much simpler perturbation theory. However, as it will be shown later in section 2.5, when both a weak high-frequency field (e.g. XUV), and an intense strong field (e.g. IR) are involved

---

[8] Otherwise, we fall again in the multi-photon regime.

in a two-color interaction, a basic SFA formulation becomes extremely successful.

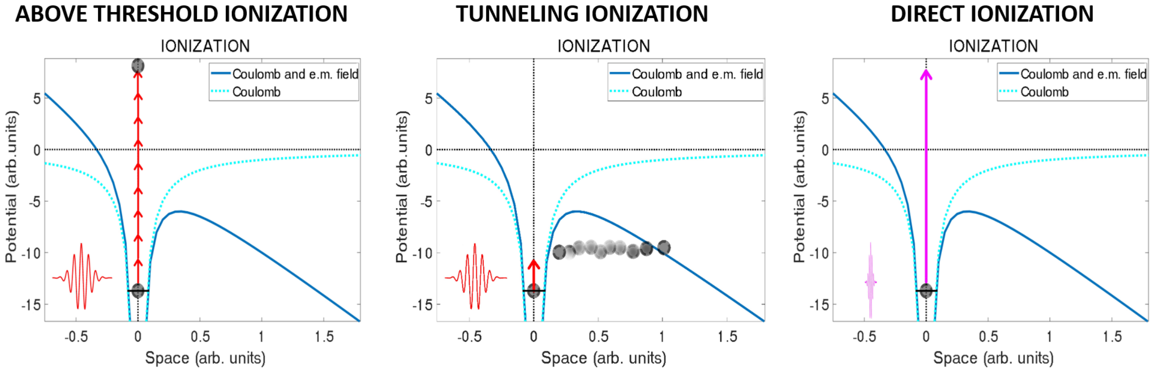
ABOVE THRESHOLD IONIZATION

TUNNELING IONIZATION

DIRECT IONIZATION

FIGURE 2.5: Schematic of the three main ionization channels from a single state in a single active electron framework.

As a final remark, one should remember that all ionization channels are always present in a strong field interaction. This becomes particularly relevant in the experiments in which one wants to study the consequences of just one ionization mechanism. Therefore, a careful choice of both the radiation and the sample ionization potential must be done in order to avoid unwanted path mixing.

2.4.2 Coulomb-Volkov wavefunction

In the presence of an electromagnetic field, the Shrödinger equation becomes:

$$(i\frac{\partial}{\partial t} - \frac{1}{2}(\hat{\mathbf{p}} + \mathbf{A}(t))^2 - V_C)\,|\psi(t)\rangle = 0 \tag{2.60}$$

Therefore, if we want to describe an ionized electronic state, its unbounded wavefunction must be a solution of this equation, similarly with what I did in 2.2.1 with Volkov states.
As it is clear by the previous statement, Volkov waves of Eq. (2.27), which is a plane wave with a time-dependent exponential factor[9], are not good solutions. Indeed, due to the presence of the Coulomb potential, they cannot satisfy Eq. (2.60). Therefore, in order to include this relevant fact in SFA we must choose a different final state, $|v\rangle$ in Eq. (2.35), which should still be a solution of the Volkov propagator, but, at the same time, it should contain information on its original state in the parent ion, we call it $\psi_{\mathbf{p}}^{(VC)}$ *Coulomb-Volkov wavefunction* [40, 41].

$$a_{\mathbf{p}}^{SFA} = -i\int_{t_0}^{t} dt' e^{-i\int_{t'}^{t}\hat{H}_F(t'')dt''}\left\langle \psi_{\mathbf{p}}^{(VC)}\right| \hat{H}_I(t')e^{-i\int_{t_0}^{t'}\hat{H}_0(t'')dt''}\,|\psi(t_0)\rangle$$

---

[9] In our case, discussed in 2.3, the Volkov factor naturally emerges from the action of $\hat{H}_F$ on the plane wave $|v\rangle$.

which become:

$$a_{\mathbf{p}}(t)^{(SFA)} = -i \int_{t_0}^{t} \left\langle \psi_{\mathbf{p}}^{(VC)} \right| \hat{H}_I(t) \left|0\right\rangle e^{+i(I_P(t'-t_0)-S(t,t'))} dt' \tag{2.61}$$

Coulomb-Volkov wavefunction are not solution of Eq. (2.60), but they have the advantage to be orthogonal to the atomic state. The most suitable form for $\left\langle \psi_{\mathbf{p}}^{(VC)} \right|$ is a central matter of several recent papers [40, 41], in which many similar models are used. To mention one, in a 2019 works [42] suggest using as a final state the exact scattering state by solving directly Eq. (2.60).

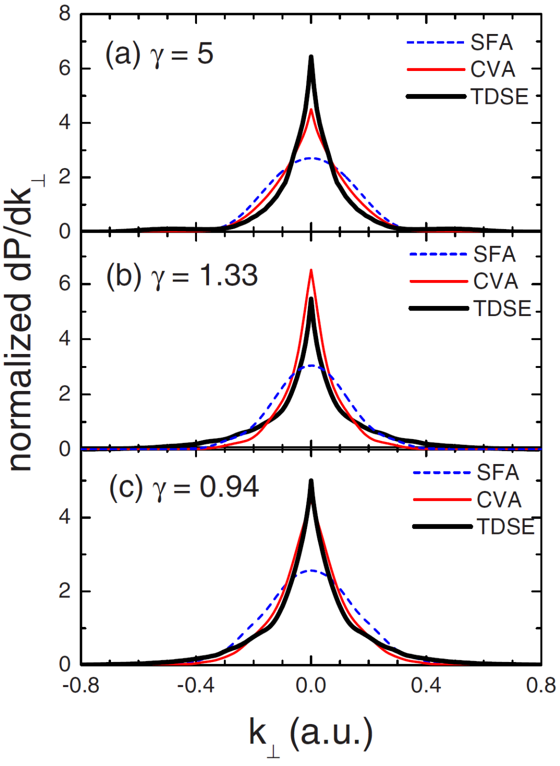

FIGURE 2.6: Example of the prediction capability of Coulomb Volkov Approximation in SFA (CVA). In the figure, it is plotted for different values of the Keldysh parameter γ the normalized transversal momentum distributions for electron in the continuum, computed via SFA (dotted blue line), via TDSE (thick black solid line), and using CVA (thick red solid line). From [41]

In conclusion, it has been shown that SFA can be dressed with several improvements to increase its accuracy and its prediction capability. However, for processes in which the main ionization mechanism is a direct ionization, and the role of the strong field is to drive the freed electron, as in a two-color interaction, we can use with confidence SFA as a more than reasonable starting point [27].

2.5 Two-colors interaction: XUV and IR

Let us now go back to a simple SFA-based description of light matter phenomena. In the following, we will look at the interaction between a single atom (SAE) and two fields: a weak XUV, $(\mathbf{E}_{XUV}, \mathbf{A}_{XUV})$ and an intense IR, $(\mathbf{E}_{IR}, \mathbf{A}_{IR})$, this is an extremely common experimental configuration, as discussed in Chapter 1.
Using Eq. (2.53), we obtain:

$$a_{\mathbf{p}}(t) = -i \int_{t_0}^{t} (\mathbf{E}_{IR}(t') + \mathbf{E}_{XUV}(t')) \cdot \mathbf{d}[\mathbf{p} + \mathbf{A}_{XUV}(t') + \mathbf{A}_{IR}(t')] e^{+i(I_P(t'-t_0) - S(t,t'))} dt' \tag{2.62}$$

with

$$\begin{aligned} S(t,t') &= \int_{t'}^{t} \frac{1}{2}(\mathbf{p} + \mathbf{A}_{XUV}(t'') + \mathbf{A}_{IR}(t'))^2 dt'' \\ \mathbf{d}[\mathbf{p} + \mathbf{A}_{IR}(t') + \mathbf{A}_{XUV}(t')] &= \langle \mathbf{p} + \mathbf{A}_{IR}(t') + \mathbf{A}_{XUV}(t') | \, \hat{\mathbf{r}} \, | 0 \rangle \end{aligned}$$

We can split Eq. (2.62) in two distinct contributions:

$$\begin{aligned} &a_{\mathbf{p}}(t) = a_{\mathbf{p}}^{(SFI)}(t) + a_{\mathbf{p}}^{(DI)}(t) \\ &a_{\mathbf{p}}^{(SFI)}(t) = -i \int_{t_0}^{t} \mathbf{E}_{IR}(t') \cdot \mathbf{d}[\mathbf{p} + \mathbf{A}_{XUV}(t') + \mathbf{A}_{IR}(t')] e^{+i(I_P(t'-t_0) - S(t,t'))} dt' \\ &a_{\mathbf{p}}^{(DI)}(t) = -i \int_{t_0}^{t} \mathbf{E}_{XUV}(t') \cdot \mathbf{d}[\mathbf{p} + \mathbf{A}_{XUV}(t') + \mathbf{A}_{IR}(t')] e^{+i(I_P(t'-t_0) - S(t,t'))} dt' \end{aligned} \tag{2.63}$$

The first term, $a_{\mathbf{p}}^{(SFI)}(t)$, is the contribution to the photo-electron emission due to strong field ionization by IR, in which we are including ATI process as well as tunnel ionization, see previous section, whereas, the second one, $a_{\mathbf{p}}^{(DI)}(t)$ describes the direct ionization triggered by the XUV pulse.
Before using Eq. (2.63), let us introduce few manipulations and simplifications, here listed:

A) We assume that XUV and IR are both linearly polarized in the same direction.

B) In the weak XUV and strong IR regime, we can safely claim that $|\mathbf{A}_{IR}| >> |\mathbf{A}_{XUV}|$. Thus, we can neglect the contribution of XUV vector potential in all the terms.

C) The initial observation time, t_0, occurs long before the interaction, so we can set $t_0 \to -\infty$. Moreover, we can disregard all the phase-term containing it without introducing any error on the final photo-electron distribution.

D) The semiclassical action can be manipulated so that:

$$S(t,t') = \frac{1}{2} \int_{t'}^{t} (\mathbf{p} + \mathbf{A}_{IR}(t''))^2 dt'' = \frac{1}{2} p^2 (t - t') + \int_{t'}^{t} \mathbf{p} \cdot \mathbf{A}_{IR}(t'') + A_{IR}^2(t') dt''$$

E) In experiments, one usually acquires a photo-electron trace long after the interaction has finished, hence, we can say that $t \to +\infty$.

As a result neglecting all the non-relevant phase terms,

$$a_{\mathbf{p}}^{(DI)} = -i \int_{-\infty}^{+\infty} \mathbf{E}_{XUV}(t') \cdot \mathbf{d}[\mathbf{p} + \mathbf{A}_{IR}(t')] e^{i(W_p + I_P)t'} e^{i\phi_{\mathbf{p}}(t')} dt' \tag{2.64}$$

while,

$$a_{\mathbf{p}}^{(SFI)} = -i \int_{-\infty}^{+\infty} \mathbf{E}_{IR}(t') \cdot \mathbf{d}[\mathbf{p} + \mathbf{A}_{IR}(t')] e^{i(W_p + I_P)t'} e^{i\phi_{\mathbf{p}}(t')} dt' \tag{2.65}$$

with $W_p = \frac{1}{2}p^2$ and $\phi_{\mathbf{p}}(t') = -\int_{t'}^{\infty} \mathbf{p} \cdot \mathbf{A}_{IR}(t'') + A_{IR}^2(t'')dt''$.
The last step to be made, in order to properly match the structure of *photo-electron streaking trace* discussed in Chapter 1, is to explicit the delay between the IR and XUV pulses in Eq. (2.64).
So,

$$\boxed{a_{\mathbf{p}}^{(DI)}(\tau) = -i \int_{-\infty}^{+\infty} \mathbf{E}_{XUV}(t) \cdot \mathbf{d}[\mathbf{p} + \mathbf{A}_{IR}(t - \tau)] e^{i(W_p + I_P)t} e^{i\phi_{\mathbf{p}}(t-\tau)} dt} \tag{2.66}$$

To make forecast on the final photo-electron distribution arising from Eq. (2.65) is not an easy task since all the terms oscillate at the same frequency ω_{IR}, on the contrary Eq. (2.66) is way simpler to be interpreted. Indeed, $\mathbf{E}_{XUV}$ is something centered in energy at ω_{XUV}, $\hbar\omega_{XUV}$ in S.I. units, modulated by low frequency, ω_{IR}, terms, $\mathbf{d}e^{i\phi_{\mathbf{p}}}$, therefore, we expect the center of the photo-electron trace to be centered at a final energy of $\omega_{XUV} - I_P$, $\hbar\omega_{XUV} - I_P$ in S.I. units plus or minus a modulation factor that goes as ω_{IR}.

As a comment, in a real experiment both the two macro-paths, strong field ionization (ATI and tunneling), Eq. (2.65), and the already discussed direct ionization, Eq. (2.66) manifest themselves. In order to avoid unwanted interference, the two regions must be kept apart by choosing a suitable sample, for the interaction, and by properly engineering the radiations, both XUV and IR.

From the next chapter, I am presenting a simulation software which basically solves Eq. (2.66), which is a quantum path superposition integral of XUV-ionization process driven by an intense IR field, also referred in literature as Laser Dressed Photo-ionization [30]. Therefore, from now on I will devote all the efforts only on the discussion of Eq. (2.66), being, now, fully aware of the environment that has generated this formula.

Central Momentum Approximation (CMA)

In Chapter 1, a fundamental, yet critical, approximation was made to run some reconstruction algorithms like FROG-CRAB, or ePie, is the Central Momentum Approximation.
Now we are ready to fully comprehend it. Starting from Eq. (2.66), hereby simply

indicated as $a_{\mathbf{p}}$:

$$a_{\mathbf{p}}(\tau) = -i\int_{-\infty}^{+\infty} \mathbf{E}_{XUV}(t)\cdot\mathbf{d}[\mathbf{p}+\mathbf{A}_{IR}(t-\tau)]e^{i(W_p+I_P)t}e^{i\phi_{\mathbf{p}}(t,\tau)}dt'$$

We can take $e^{i\phi_{\mathbf{p}}(t')}$ and $\mathbf{d}[\mathbf{p}+\mathbf{A}_{IR}(t')]$, we can neglect the momentum dependence, $\mathbf{p}$, by saying that its contribution is almost equal to the value of these two function at $\mathbf{p} = \mathbf{p}_C = \omega_{XUV} - I_P$, with ω_{XUV} central frequency of the XUV. This approximation allows us to exploit a generic Fourier Transform based algorithm, indeed, our trace is the Fourier transform of the XUV field times the dipole transition element modulated by the IR through a phase term.

$$a_{\mathbf{p}}^{(CMA)}(\tau) = -i\int_{-\infty}^{+\infty} \mathbf{E}_{XUV}(t)\cdot\mathbf{d}[\mathbf{p}_C+\mathbf{A}_{IR}(t-\tau)]e^{i(W_p+I_P)t}e^{i\phi_{\mathbf{p}_C}(t-\tau)}dt \qquad (2.67)$$

2.5.1 Photo-ionization time delay and atomic phase

Before concluding this chapter, let us discuss shortly a fundamental result that have pushed research effort in Attosecond Science.
Since the first experimental measurement of an apparent relative-delay in photo-ionization of Ne-2s and Ne-2p, retrieved from streaking trace [13], a great debate has opened on the true meaning behind this event [14].

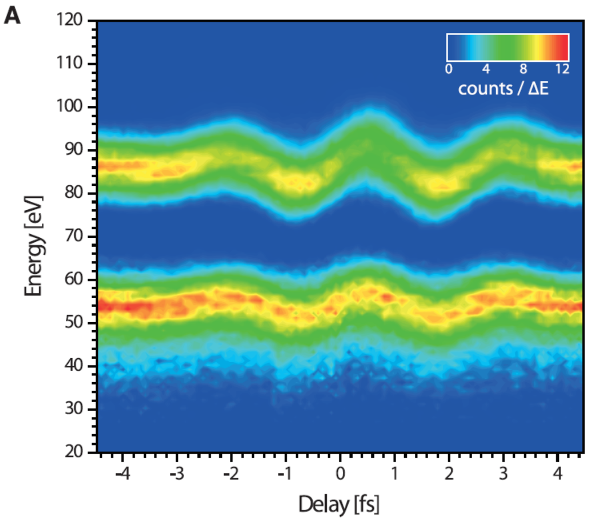

FIGURE 2.7: Experimental streaking measurement of relative delay in photo-emission from the ionization of Ne-2s and Ne-2p, from [13]. A delay of $21(5)$ as was estimated by the analysis of the streaking trace.

A delay in photo-ionization is defined as the change in the ejection time of a photo-electron pulse with respect to the interaction time [13]. In other words, it works as if the photo-electron waits a particular time after the interaction before "jumping" in the continuum.
This clearly has an uncertain theoretical meaning since, as we have just discussed in previous sections, the concept of interaction time is fuzzy. After all, the final

electron distribution in a streaking experiment, like in Eq. (2.66), is the product of an interference process between many different quantum paths, which co-exist at different time indistinguishably.
In order to comprehend the physical origin of this phenomenon and how to evaluate it, we will strongly simplify the discussion on two-color interaction by exploiting the Central Momentum Approximation as in Eq. (2.67).
A more comprehensive discussion can be found in [43], and in a recent review work [44], however, some open questions are still in search for an answer.

In a naive picture of two-colors interaction, the XUV-radiation emits a "replica" in energy of the photo-electron, while the IR field streaks it up and down following $e^{i\phi_{\mathbf{p}_C}(t-\tau)}$, as a function of the delay between the two pulses.
The role of the dipole transition element, like $\mathbf{d}[\mathbf{p}_C + \mathbf{A}_{IR}(t-\tau)]$ in Eq. (2.67), was simply regarded as a cross-section factor, $\sigma(p)$, that tell us how much a dipole-transition is probable, like in the Fermi-Golden Rule [24]. This is the reason why, is often set as unitary.
As discussed in the work [45], this is just half of the picture. Indeed, thanks to attosecond physics we have, finally, experimental access also to the phase of the dipole transition matrix element projected in a momentum state in the direction $\mathbf{n}$:

$$\mathbf{d}[\mathbf{p}] = \langle \mathbf{p} | \, \hat{\mathbf{r}} \, | i \rangle = \sigma(\mathbf{p}) e^{i\varphi(\mathbf{p})} \mathbf{n} \tag{2.68}$$

where the initial state $|i\rangle$ is an atomic bound state, while the final state, $|f\rangle$, as discussed in section 2.4, can be a simple plane wave state of momentum $\mathbf{p}$, a Coulomb-Volokov state, a partial wave or a suitable scattering state.
Rewriting Eq. (2.68) as a function of the final electron state energy, ϵ, and forgetting about any angular information hidden in Eq. (2.68),

$$d[\epsilon] = \sigma(\epsilon) e^{i\varphi(\epsilon)} \tag{2.69}$$

The atomic phase $\varphi(\epsilon)$ of Eq. (2.69) is ultimately responsible of an observed time delay in the photo-electron "replica" of the XUV pulse, as I will discuss in a while. This, however, is still not enough and other effects, like electron correlation or internal resonance have a role in the delay, fortunately they can be modeled as addition phase term in Eq. (2.69), this allows to extend the predictions on photo-ionization time-delays [45].
In our simplified picture, we can say that the dipole element times the XUV-field are almost equivalent to an "atomic field", $E_{at}(t)$ whose Fourier transform, in final electron energy ϵ is:

$$\tilde{E}_{at}(\epsilon) = \mathcal{F}(E_{at}(t)) = d(\epsilon)\tilde{E}_{XUV}(\omega) = \sigma(\epsilon) e^{i\varphi(\epsilon)} \tilde{E}_{XUV}(\epsilon + I_P) \tag{2.70}$$

where, thanks to atomic units, $\omega_{XUV} = \epsilon + I_P$.
In this way, Eq. (2.67) become:

$$a(\epsilon)^{(CMA)}(\tau) \approx -i2\sqrt{\epsilon} \int_{-\infty}^{+\infty} \mathbf{E}_{at}(t) e^{i\phi(t-\tau)} e^{i(\epsilon+I_P)t} dt \tag{2.71}$$

which, now, totally resemble a Fourier transform of the atomic field times an IR-gate function.
We define *Wigner-delay* as [45]:

$$\tau_W(\epsilon) = \frac{\partial\varphi(\epsilon)}{\partial\epsilon} \tag{2.72}$$

Now, if we set to unitary the cross-section, and we expand the atomic phase φ around the center of the photo-electron trace, neglecting higher order term we obtain:

$$\tilde{E}_{at}(\epsilon) = e^{i\varphi_0 + i\tau_W(\epsilon + I_P)}\tilde{E}_{XUV}(\epsilon - I_P) \tag{2.73}$$

As a result, the time profile of the atomic field, here evaluated with its Fourier transform $\tilde{E}_{at}(\epsilon)$, has an additional phase quantity that has the same role of a standard group delay in dispersive media [5]. The photo-emission delay is then simply a shift in time of the resulting streaking trace with respect to an ideal trace generated without this atomic phase term.

In conclusion, this delay can be experimentally observed by confronting the relative delay between different atomic levels as they did in Fig. 2.7, and can be reconstructed by evaluating the spectral phase of the reconstructed atomic field with respect to a reference input XUV field.

Chapter 3

Simulation of attosecond spectroscopy traces

In this chapter, I will present the Matlab code, SFEXIS, Strong Field Electron XUV Interaction Simulations, that I have developed for the simulation of streaking traces, and, more in general, to all kind of two-color strong-field interactions traces. The programme is based on the numerical resolution of the two-color SFA equation, extensively discussed in Chapter 2.
The purposes of these simulations are two-fold:

1) To serve as support for the experiments (i.e., to give access to basic information on the possible experimental outcome by changing some input variables)

2) To serve as a first step for the implementation of ensemble effects in the streaking trace, which is the goal of this thesis work.

This code is inspired by a previously existing version, with some significant upgrades in the calculation speed and fields customization. An additional feature is to include the dipole transition element, which can be either calculated with a simple quantum-mechanical model, as I will discuss in Section 3.1.3, or inserted by the user.

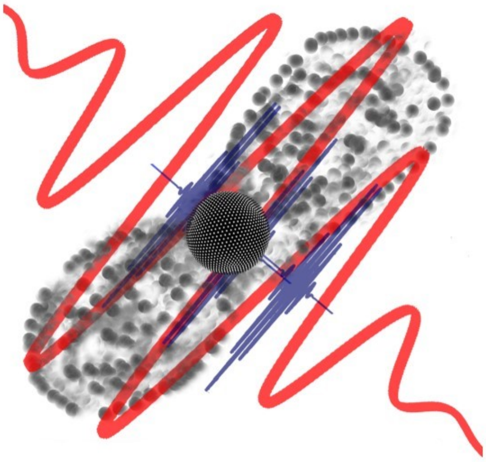

FIGURE 3.1: Sketch of two color interaction with quantum path interference of the different photo-electron ionization time.

3.1 Numerical simulation of two-color interaction

Let us restart, from the result of the two-color interaction, which describes the probability of detecting a photo-electron in a free-particle state with momentum **p**, in atomic units:

$$a_{\mathbf{p}} = -i \int_{-\infty}^{+\infty} \mathbf{E}_{XUV}(t) \cdot \mathbf{d}[\mathbf{p} + \mathbf{A}_{IR}(t)] e^{i(W_p + I_P)t} e^{i\phi_{\mathbf{p}}(t)} dt' \tag{3.1}$$

where $W_p = \frac{1}{2}p^2$ and $\phi_{\mathbf{p}}(t') = -\int_{t'}^{\infty} \mathbf{p} \cdot \mathbf{A}_{IR}(t'') + A_{IR}^2(t'')dt''$.
To solve Eq. (3.1) numerically, we first need to initialize the simulation parameters:

- **IR field**: The user selects the central pulse wavelength, λ, duration (in FWHM), the spectral dispersion parameters up to the third order, and the carrier-envelope phase (CEP). From the spectral definition of the field, through an over-sampled fast Fourier Transformed the exact time profile is calculated. The IR peak intensity is also a free parameter.

- **XUV field**: The central frequency of the harmonic spectrum together with the parameters dispersion (GDD, TOD) and the CEP are set as input variables. Besides, the code allows for simulating an experiment with a single attosecond pulse or with a train of attosecond pulse.

- **Atomic Species**: In the current version of the programme, I have included the ionization potentials of argon, neon, and helium.

- **Dipole**: This is the main novelty of the code I have developed. The previous existing versions of the streaking simulation programmes in the laboratory worked under the approximation of unitary dipole and central momentum approximation. In this programme, a simple model for the transition dipole element using Eq. 3.1 has been included. Alternatively, the user can keep the dipole to unitary value or can load the dipole from an external file.

- **Resolution**: The user can select the desired temporal, spectral, delay resolution, without any constraints, except for the available memory.

Moreover, the programme uses the calculated vector potential, for both IR and XUV, to set up an easy error check by calculating the vector potential discrete-time integral. In fact, ideally, the integration over the vector potential of any field should be as close to zero as possible. Deviation from this behavior generates numerical errors in the final trace.
The XUV field and the final photo-electrons trace are normalized to one, since, in this work, I am not interested in the photo-emission efficiency, but rather, on the dynamical behaviors.

3.2 Models for the dipole transient element

As discussed in Chapter 2, the dipole in Eq. (3.1) has two main roles:

1 To introduce a cross-section factor that tells us how efficient is the photo-emission process.

2 To introduce a phase factor that is responsible for the photo-emission delay phenomenon.

The current version of SFEXIS evaluates Eq. (3.5) in a 1D framework, thus, assuming linearly polarized fields and 1D momentum distribution, the extension to more complex profiles is just a matter of coding effort. The dipole transition element can be calculated from a simple model or imported, as an external input, from more advanced calculations, like [46].

The "simple" model is a 1D dipole transition element, in the same direction of the fields polarization, z-axis in our case, evaluated between a bound hydrogenoid state, numerically calculated using the hydrogenoid wavefunction, optimized depending on the atomic species chosen to be studied (Ar, Ne, He), and a plane wave state of momentum p_z.

$$\mathbf{d}[p_z] = \langle p_z | \, \hat{\mathbf{r}} \, | 0 \rangle \tag{3.2}$$

where he plane wave state is given by:

$$\langle p | z \rangle = e^{i p_z z} \tag{3.3}$$

and the ground state, here expressed in spherical coordinates (r, θ, ϕ) for simplicity, is given by:

$$\langle 0 | \mathbf{r} \rangle = Y_l^m(\theta, \phi) R_{nl}(a, r) \tag{3.4}$$

with $a = \frac{1}{Z_{eff}}$, effective Bohr radius, (n, l, m) quantum numbers, $Y_l^m(\theta, \phi)$ spherical harmonics, and $R_{nl}(a, r)$ the radial part. At the end $\mathbf{d}[p_z]$ is taken only in the z-direction.

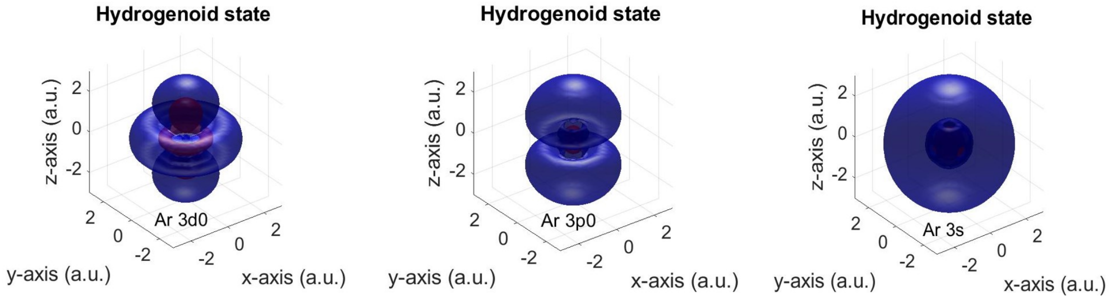

FIGURE 3.2: Numerically calculated hydrogneoid wavefunction for Ar. In the figures two iso-probability surface are plotted. Argon 3p with m=0 is used in next discussion as the ground state for photo-electron emission calculations.

The choice of plane wave-state as a final state is just an approximate model. Indeed, as discussed in Chapter 2, a photo-electron that is emitted from its parent ion ends up in a final scattering state with momentum p that should, in general, includes information on both information on the electromagnetic fields and the Coulomb potential.
In literature different models can be found [46, 42].
Therefore, selecting the most appropriate final state is relevant because only with more advanced models we can predict the existence of atomic delays, mentioned in the last part of Chapter 2, and we can understand the result of an attosecond measurement.

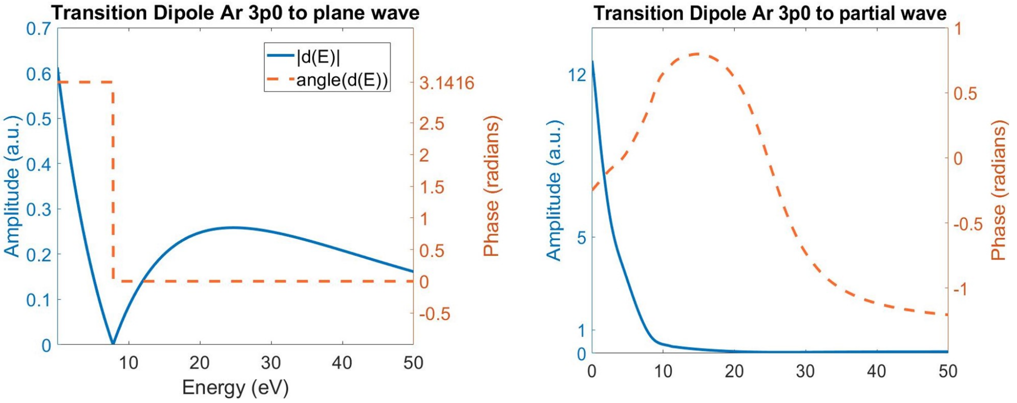

FIGURE 3.3: On the left-hand side panel, a numerically calculated dipole for Ar 3p0 using a simple plane wave model. The phase of the dipole is flat; therefore, we do not expect any atomic delay, see Chapter 2. On the right-hand side a dipole calculated with the model discussed in [46], *courtesy of Prof. C.D.Lin and co-worker*. The model used by [46] is a single electron model, that assumes that the electron is ejected from the 3p0 shell of Ar into a partial-wave state. The dipole phase, clearly, shows a non-flat profile, causing a delay in the photo-emission trace.

In [46], for instance, partial-wave state, free-states with the presence of a Coulomb potential are used.
Both models, shown in Figure 3.3, presents some limitations.
One one hand, as shown later, the ground-state-to-plane-wave model produces reasonable photo-electrons streaking trace, but its phase profile too naive and is not capable of predicting any photo-emission delay. One the other hand, the partial wave model used by [46], has a clear non-flat phase profile, but its dipole amplitude grows fast for lower energy, producing a streaking that does not match with experimental evidence [47]. As shown in the next figure, we can make a trade-off between the two models and combine the amplitude of the plane-wave model with the phase of the partial-wave one. This "mixed" model will help us to evaluate in the last chapter also the effect of volume effect on photo-emission delay.
In conclusion, all models are based on a single active electron description; hence, they cannot predict many-body effects. After all, Ar is a multi-electron atom.

Thus, more advanced calculations should be performed to reach an experimentally accurate model.

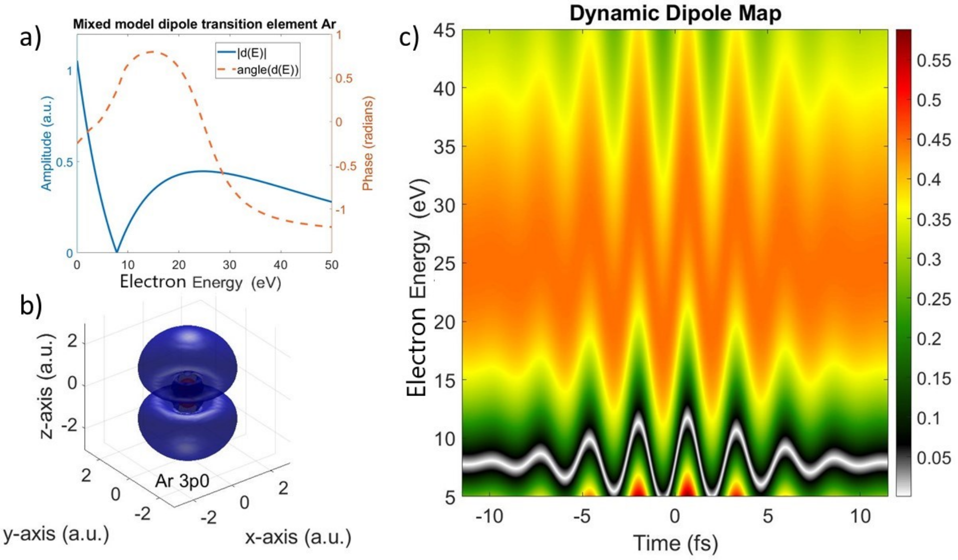

FIGURE 3.4: a) Numerical calculation of Ar dipole transition element with the "mixed" model. The amplitude has been calculated with a plane-wave based model, while, for the phase, it has been used the partial-wave based model of [46] $d(p)$.; b) Ar 3p0 wavefunction; c) Ar "dynamic" dipole amplitude, $|d(p + A_{IR}(t))|$, evaluated with a transformed limited IR field of FWHM=10 fs and peak intensity 5 10^{12} $\frac{W}{cm^2}$.

Once the dipole transition element is calculated/imported the programme calculates $d[p + A_{IR}(t)]$ by exploiting a Fourier time-shifting technique. Now, that all the input parameters are fixed, the programme evaluates the following expression at different XUV-IR delays:

$$\boxed{a_p(\tau) = -i \int_{-\infty}^{+\infty} E_{XUV}(t-\tau) d[p + A_{IR}(t)] e^{i(W_p + I_P)t} e^{i\phi_p(t)} dt'} \tag{3.5}$$

3.3 Simulation of photo-electron traces

In the following pages, I am going to present how SFEXIS is capable of reproducing, under different input conditions, the photo-electron traces that can be found in the literature and can be obtained from an experiment.
The main criterion that has guided the parameter choice is to be as close as possible to the experimental conditions available in the lab.

3.3.1 Single Attosecond Pulse: Streaking Trace

As already discussed in Chapter 1, when a single attosecond XUV pulse interacts with an atom, photo-electrons are emitted with kinetic energy centred at the XUV central frequency minus the atomic ionization potential. If a Strong Field IR is also present, the photo-electron is streaked up and down in energy. As a result, from the superposition of all the possible quantum-path, each with a different accumulated Volkov phase, and by exploring different delays between the IR driving pulse and the XUV fields, the streaking trace appears, as shown in Figure 3.5.

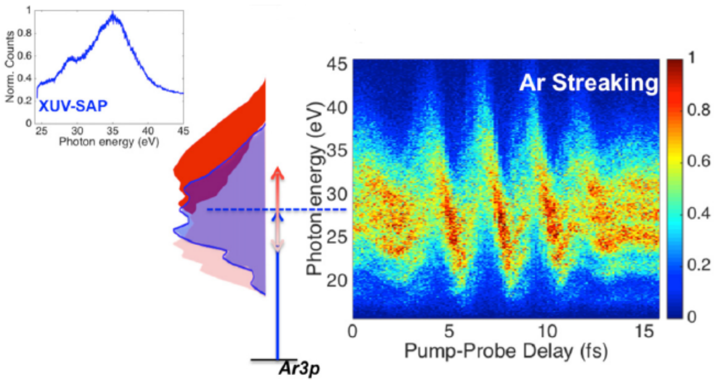

FIGURE 3.5: A single attosecond pulse, with XUV spectrum shown on the left panel, that interacts with an Ar atom, produces a photo-electron energy distribution, central panel (blue area). If an intense IR field is present, then the spectrum "streaks" following the IR vector potential(red areas) producing a streaking trace. In the right panel an experimental streaking trace recorded in Ar [47].

From Eq. (3.5) we can simulate a streaking trace feeding the programme with an attosecond pulse, as shown in Figure 3.9.

As discussed in the previous section, my programme can also include the evaluation of the dipole transition element, which can be calculated from a simple model implemented at the moment in SFEXIS or uploaded from an external file. As shown in Figure 3.7, the model used in [46] generates a highly distorted streaking trace. This is, mainly, due to the high slope that the modulus of the dipole shows in the low-energy region. As a result, since this trace is harder to reconstruct with ePIE, it will not be used in the next chapter.

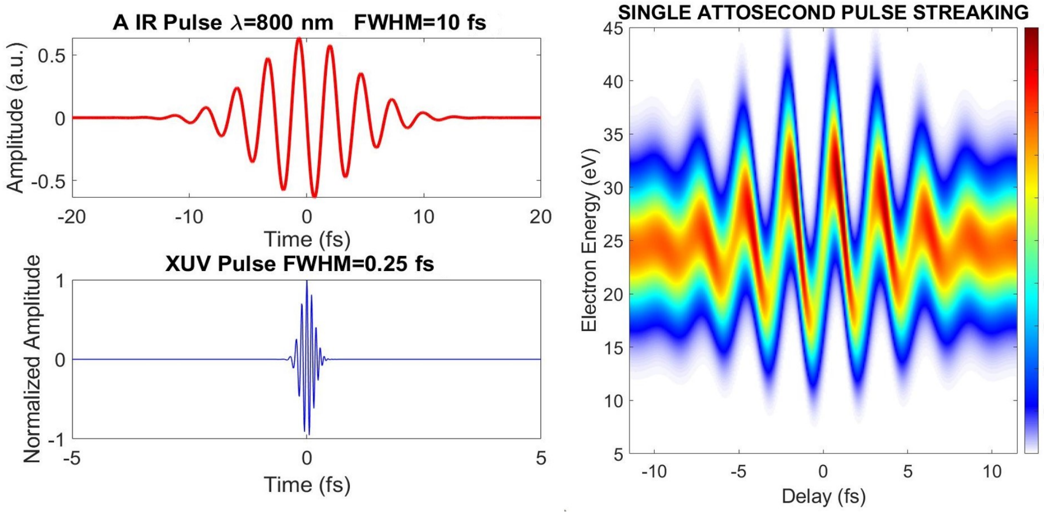

FIGURE 3.6: Example of Streaking trace calculated with SFEXIS for Argon with a peak intensity of the IR of I=5 10^{12} $\frac{W}{cm^2}$, the IR is a transform-limited pulse (no GDD nor TOD) with FWHM=10 fs and central frequency 800 nm. The XUV is centred at the 25-th harmonics of the IR, and has FWHM=250 as and GDD=0.01 fs^2. The trace is simulated without any model for the dipole, hence fixed at unitary value. Resolutions: time, 10 as, delay, 50 as, energy 0.05 eV.

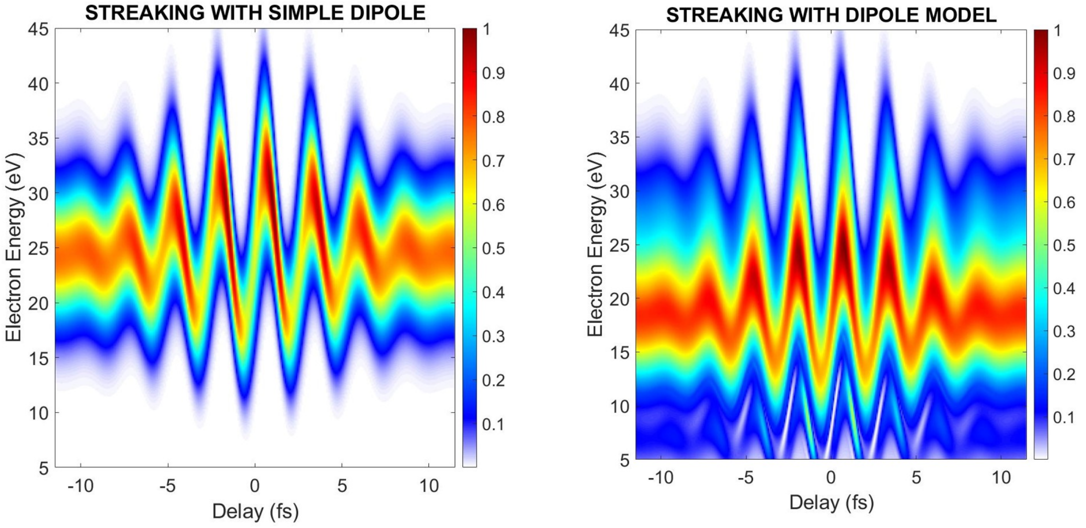

FIGURE 3.7: On the left panel, a simulated streaking trace of argon with a single attosecond pulse of 250 as, GDD=0.01 fs^2 centred at the 25-th harmonics, and with a transform-limited IR at 800 nm, FWHM 10 fs and peak intensity 5 10^{12} $\frac{W}{cm^2}$ and a simple dipole model. On the right panel, instead, the same simulation is run, with, this time the dipole calculated as in [46]. The resolution in time is 10 as, in energy 0.05 eV, while the delay is 100 as. In this case, a lower delay resolution is necessary due to memory limitation.

3.3.2 Attosecod Train of Pulses (RABBITT) and Long XUV Pulse

Another typical photo-electron experiment is the so-called Resonant Attosecond Beating By Interference of Two-photon Transitions (RABBITT), which is used as the streaking trace for investigating attosecond photo-emission delay in different atomic or molecular species [47]. A RABBITT experiment is the result of the interaction of a train of attosecond pulses (ATP) with an intense field on a target. Hence, it can be seen as the coherent interference of several streaking traces, each obtained from a certain pulse of the train.

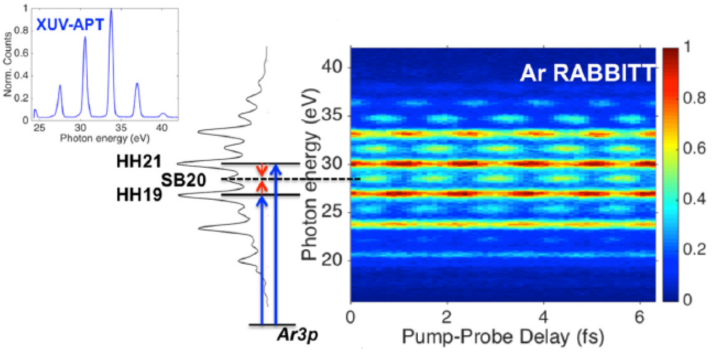

FIGURE 3.8: The spectrum of an HHG generated train of attosecond pulse is composed only by odd-harmonics of the fundamental frequency, right panel. As a result of the coherent sum of many streaking, a RABBITT shows peculiar period patterns that repeat within a period of two times the IR frequency, left panel. These patterns are also centred at an energy that lies between two harmonics, *as if* the electron absorbs an additional IR photon at only certain delays between the IR and the XUV. From [47].

Due to the RABBIT nature, it can be perfectly described by Eq. (3.5), and, so simulated by the programme, as shown in Figure 3.9.

In the Attosecond Research Center laboratories, we are capable of generating XUV pulses of a few fs, so I have tried to give the programme a 15 fs XUV field. The resulting photo-electron trace can be again used to characterize the pulse used or to discuss simple molecules electron-dynamics [22].
As expected, in Figure 3.10, the photo-electron trace shows what are usually called sidebands at an energy equal to the central XUV frequency, minus the ionization potential, of course, plus or minus the energy of an IR photon.

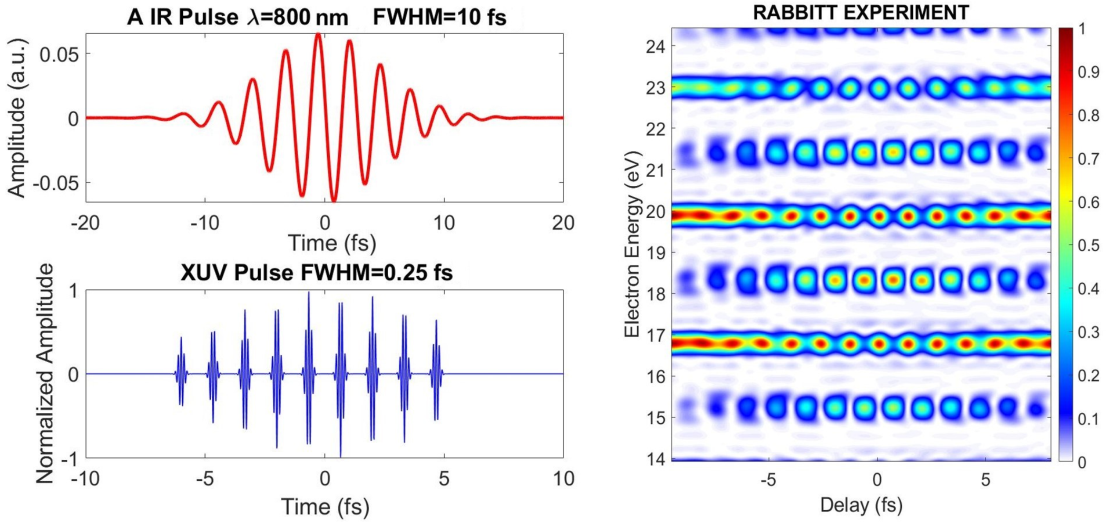

FIGURE 3.9: RABBITT simulation with SFEXIS obtained with a transformed limited 10 fs (FWHM) IR centered at 800 nm, with an intensity peak of I=5 10^{11} $\frac{W}{cm^2}$. The XUV ATP has an odd-harmonics spectrum centered on the 25-th harmonics of the fundamental, the height of the single-pulse peaks is normalized to the IR envelope profile. Each single attosecond pulse is transformed limited and has a FWHM of 250 as.

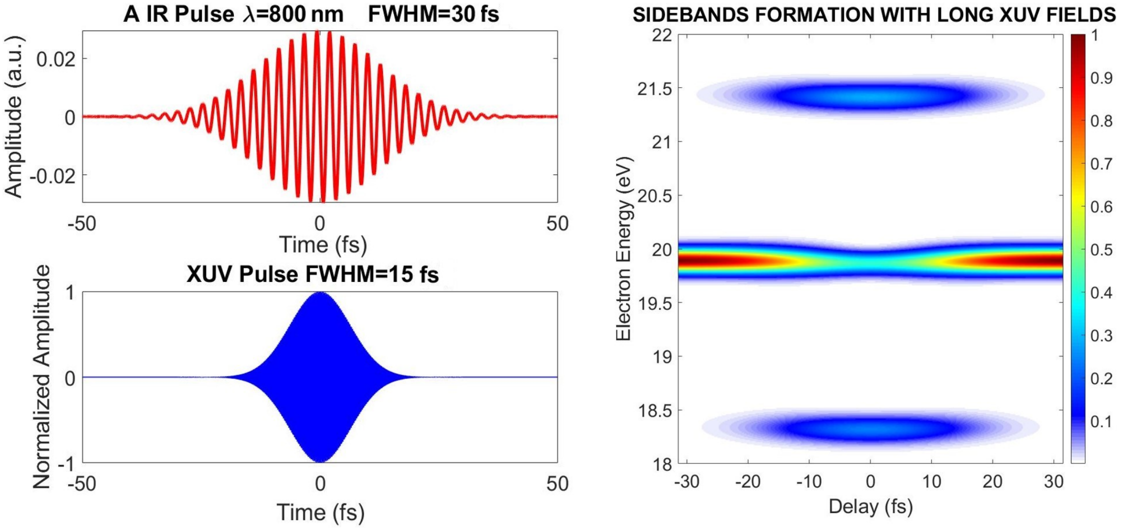

FIGURE 3.10: Sidebands formation simulated in SFEXIS with a transformed limited IR field, centered at $\lambda = 800$ nm, with FHWM=30 fs and peak intensity at I= 10^{11} $\frac{W}{cm^2}$. The XUV pulse is transformed limited centered at the 25-th harmonics of the fundamental and has a duration of 15 fs.

Chapter 4

Investigation of ensemble effect in streaking spectroscopy

In this chapter I will present the final discussion on the ensemble effects in attosecond streaking and how it affects the retrieval of the pulse information.
It is essential to highlight that the inclusion of collective effects is novel and has been rarely studied in literature. Section 4.1 deals with the criteria used to include the spatial effects in the simulation programme presented in Chapter 3.
The simulation of different streaking traces considering collective effects is then presented.

In section 4.2, a discussion on the impact of ensemble effects in the retrieval of the temporal pulse profile is provided. To this end, I have tested a programme based on ePIE with the simulated traces. The robustness of the reconstruction and the resolution limits are studied.

In the last part of section 4.2.1, a preliminary study on the consequence of ensemble effect on the photo-emission delay will be considered. For a better and more accurate evaluation, higher resolution of the simulations (lower than 10 as) and finer model for the dipole transition element will be used.

4.1 Simulations of ensemble effects in streaking traces

As discussed in Chapter 1, an experimental streaking trace generated by the interaction between XUV-IR and a gas jet of atoms, or molecules, is the result of an averaging over many collected photo-electrons, generated in different spatial position. Since we can reasonably infer that the emitted photo-electrons are independent of each other, then, each point of the XUV-IR-atom interaction zone can be regarded, per se, as a single "streaking experiment" with a well-defined time-varying field amplitude. As a consequence, a reasonable way to model the overall photo-electron streaking trace is to sum over all the possible "streaking points" using the local XUV intensity as a weight. So, regions that feel higher XUV peak values will contribute more to the final streaking than regions exposed to a lower XUV intensity. Similarly, by assuming concentricity and cylindrical symmetry for XUV and IR, we can reduce our weighted sum to a 1D radial average, in this way, "streaking points" with higher radius will contribute more than points closer to the centre.
Let us call $W(\epsilon, \tau)$ the emission averaged streaking trace, and $W(\epsilon, \tau, r_i)$ the streaking trace calculated at the "streaking points" defined by the radial position r_i. Then, for a discrete vector of N elements with resolution Δr

$$W(\epsilon, \tau) = \sum_{i=0}^{N} W(\epsilon, \tau, r_i) E^{(R)}_{XUV}(r_i) 2\pi r_i \Delta r \tag{4.1}$$

where $E^{(R)}_{XUV}(r_i)$ is the normalized XUV radial profile.
In this model, for simplicity, the ensemble effect are studied on a 2D-interaction sheet. The generalization to a 3D profile is straightforward.

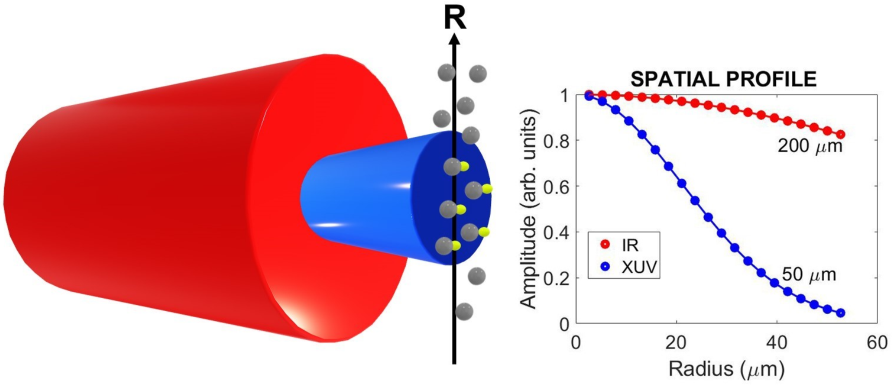

FIGURE 4.1: Schematic representation of the interaction between: a gas jet of atoms, grey spheres, which emits electrons, yellow spheres; an IR field, in red; and an XUV field, in blue. Each point of the right panel is a SFEXIS simulation that is then averaged following Eq. (4.1). The lengths indicated in the left panel are the simulated radial FWHM of the XUV-IR profiles.

The study of ensemble effects has been performed by simulating the interaction between Ar, $I_P = 15.75962$ eV, a transform limited IR field $\lambda_{IR} = 800\ nm$, and a single attosecond XUV pulse centered at the 25-th harmonics of the IR. The work is organized in 4 distinct main simulations:

Main Simulations Settings					
Simulation ID	FWHM_{XUV} (as)	FWHM_{IR} (fs)	GDD_{XUV} (fs^2)	Dipole	E_{IRpeak} ($\frac{W}{cm^2}$)
1	250	10	0	NO	$5\ 10^{12}$
2	250	10	0.01	NO	$5\ 10^{12}$
3	250	10	0	YES	$5\ 10^{12}$
4	250	10	0.01	YES	$5\ 10^{12}$

TABLE 4.1: List of the parameters used in each of the four main simulations.

The ensemble effects and the reconstruction capability are tested with and without the presence of the group delay dispersion (GDD), and with and without the presence of the dipole transition element, predicted by the theory of strong-field interaction.

For each on of the main simulations, then, five different radials Full-Width at Half Maximum (rFWHM) have been explored, mimicking experimental condition, for IR: [25 μm, 50 μm, 100 μm, 200 μm, FLAT]. The XUV field is, instead, fixed at 50 μm. This value has been chosen to the typical radial profile available in our lab. Each individual XUV-IR configuration is scanned in a SFEXIS simulation over 20 radial "streaking points", see Figure 4.1, and, then, averaged using Eq. (4.1).

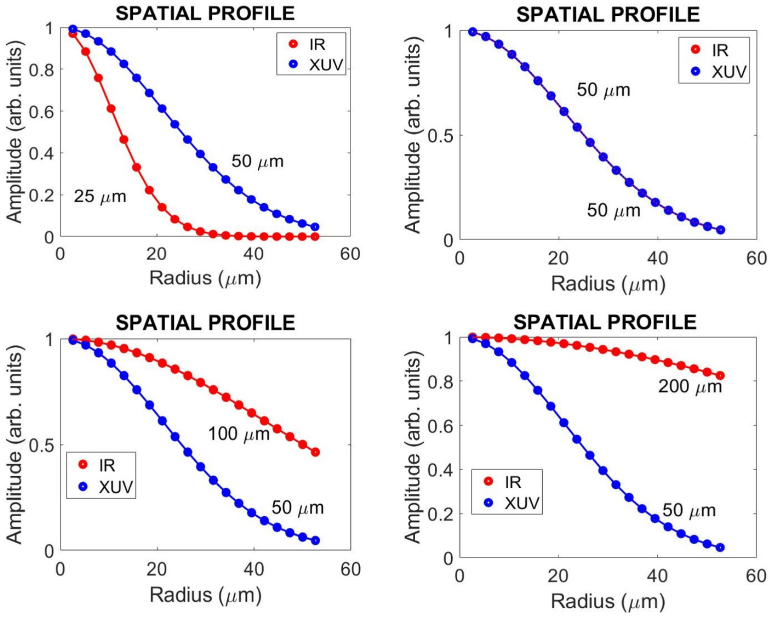

FIGURE 4.2: For each main simulation, different configurations of the IR are explored, keeping the XUV FWHM fixed. Each vertical couple of blue and red points in each image is a SFEXIS simulation. These scans are repeated for each one of the main simulations listed in table 4.1.

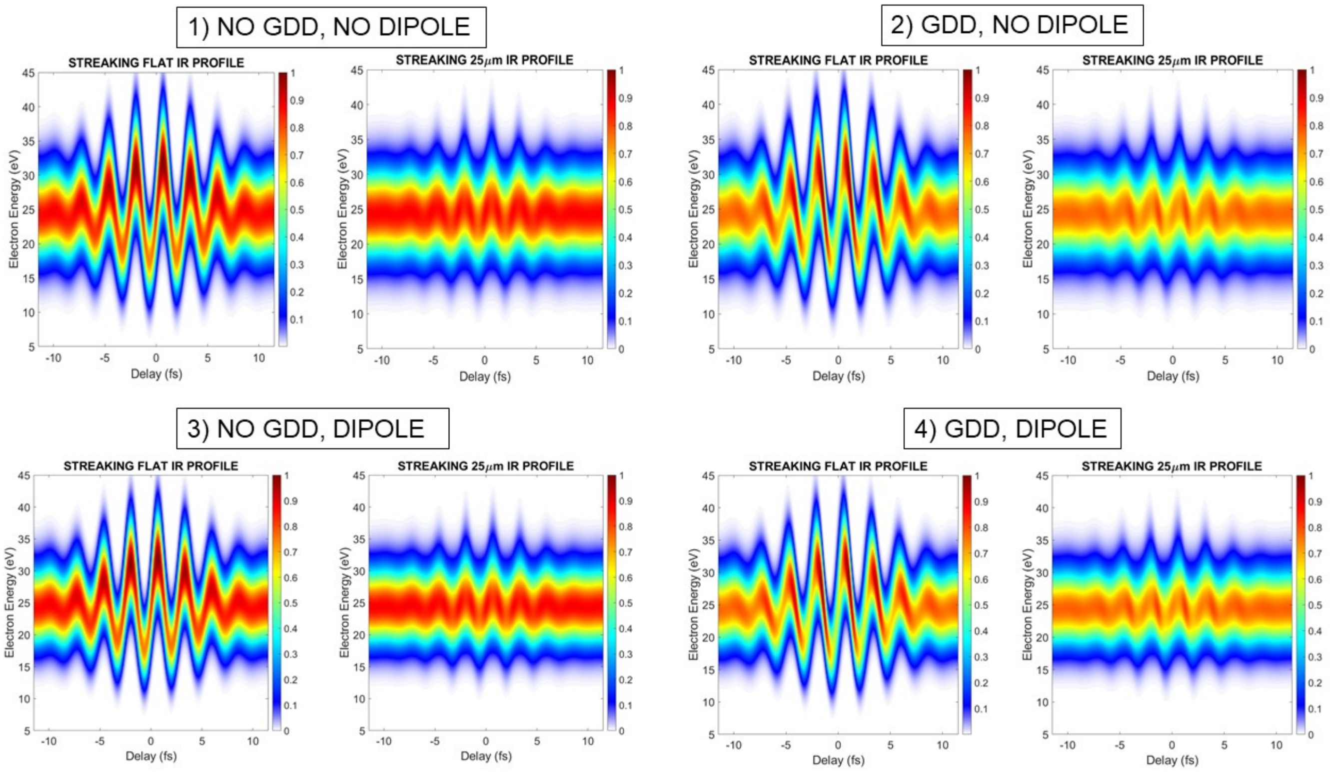

FIGURE 4.3: Result of all the 4 main simulations: flat streaking profile vs streaking with $25\mu m$ of IR radius. The relative variation between the two traces can reach the 60%.

As shown in Figure 4.3, the **main ensemble effects** on the streaking trace due to a non-flat IR-XUV profile are: a *reduction of the trace sharpness* and fewer electron counts at the delays at which the streaking amplitude is maximum or, *streaking peak bleaching*. While the latter effect is harder to predict a priori, the former is reasonable. Indeed, for the flat profile case each "streaking point" sees an IR always at its peak value, while, in a 25-μm condition, the radial IR profile intensity fades quicker than the XUV radial intensity profile. As a consequence, the majority of streaking points will see a weaker IR field resulting in a reduced averaged streaking effect, giving thus smoother trace.

In the following, I will present the ensemble effects analysis concentrating only on one out of the four simulations. Similar considerations hold for the others as well.

4.1.1 Analysis of ensemble effects in a SFEXIS simulation

Let us consider the simulation with the higher degree of complexity, in which we are including both the effect of the XUV dispersion, GDD, and the transition dipole element.

Simulation ID	FWHM$_{XUV}$ (as)	FWHM$_{IR}$ (fs)	GDD$_{XUV}$ (fs^2)	Dipole	E$_{IRpeak}$ ($\frac{W}{cm^2}$)
4	250	10	0.01	YES	5 10^{12}

In this simulation, the dipole term has been calculated with the simple model as the transition element from the atomic bound state 3p0 of Ar to plane wave state. While the dipole phase is flat, hence, we do not expect any atomic delay, the dipole amplitude, or cross-section, is not.

Therefore, we can foresee, as later discussed, some effects on the reconstructed effective atomic field spectral amplitude, which is composed by the product between the XUV field spectral amplitude and the dipole cross-section, as discussed in Chapter 2.

The presence of a positive GDD in a 250-as XUV pulse creates a left-to-right asymmetry in the streaking profile, in which the photo-electron counts become higher on the streaking falling edges and lower on the streaking rising edges.

The orientation of this GDD-effect depends on the delay axis convention. It is, therefore, reversed when the delay axis is flipped. This simple fact becomes relevant when passing a streaking trace from SFEXIS to ePIE. Indeed, while SFEXIS works with a delayed XUV, ePIE delays the IR fields, therefore reversing the sign of the delay axis.

Scans Simulation Resolution	
dE (eV)	0.05
dt (as)	10 as
$d\tau$ (as)	60 as

In Figure 4.4, I am reporting the result of the analysis on the ensemble effect. I have plotted the relative difference (i.e. subtraction of both traces) between the ensemble averaged streaking trace, for a specific radial condition, and the trace obtained with a flat IR radial profile. All simulations are normalized with respect to the flat streaking trace. We can observe that the relative difference is higher in the upper zone of the trace, up to 60$\%$ in the 25-μm case. For higher radii the relative difference drops quickly, and, for the 200-μm case, the difference between the flat and the ensemble-averaged streaking is, in the worst case, around 6 $\%$, which is hard to be perceived without an analysis tool.

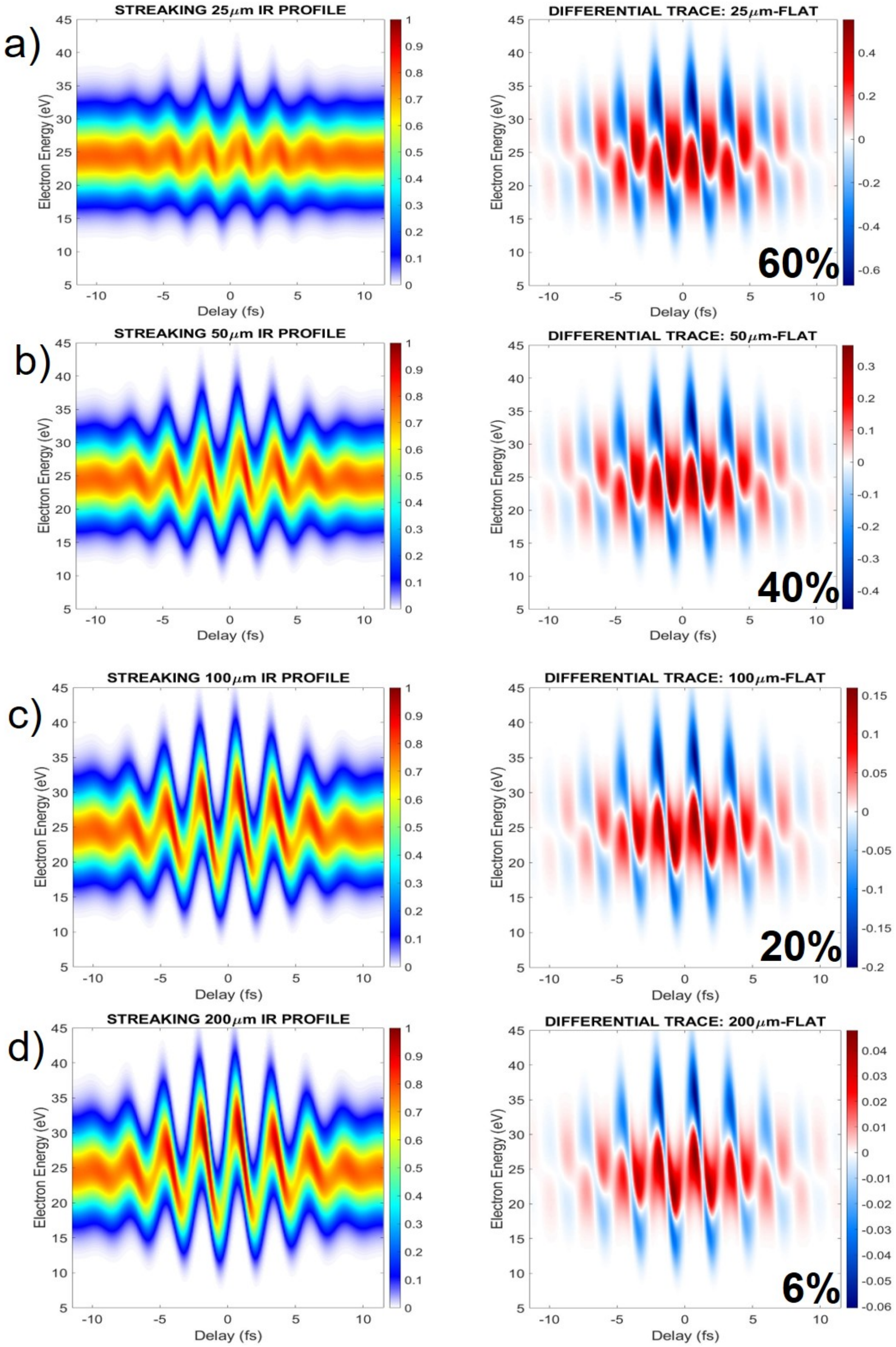

FIGURE 4.4: Result of ensemble effects analysis in Ar with dipole and with GVD. A clear emptying of the streaking peaks can be observed in all the figures. The differences in the traces go from 6 % in panel d), to 60% in panel a). The streaking traces are plotted as normalized energy density profile, therefore including a jacobian factor of $\sqrt{\epsilon}$, with ϵ being the electron energy.

4.2 ePIE robustness against ensemble effect

At this point, our question is simple:

> *Do ensemble effects change the accuracy of the reconstruction software ePIE in the process of information gathering from an input photo-electron streaking trace?*

As discussed in Chapter 1, ePIE is capable of retrieving both IR and XUV fields from an input streaking trace. Therefore, I have tested its robustness with the results of the four main SFEXIS's simulations, within the chosen temporal resolution, number of iterations, and delay axis step, as shown in the following table.

ePIE parameters	
ePIE Iterations	2000
dt (as)	26
$d\tau$ (as)	134

The results are organized in table 4.3 by reporting the betas parameter used for the reconstruction, see Chapter 1; the initial guess for the field amplitude A_0, which is a key parameter to make the convergence faster and more accurate; and the results of the reconstruction. The reported results are: the reconstructed XUV group delay, τ_g, which, when present, should include the atomic delay; the XUV GDD; and the two FWHMs, in amplitude, of the XUV and IR field. These values are extracted from a proper spectral phase and spectral amplitude fitting, in the XUV case, and from a temporal envelope fitting, in the IR case.

We can observe that the reconstructed group delay is below the time resolution in all the analyzed cases, therefore, as expected the presence of our simple dipole does not delay the photo-emission, since the dipole phase is flat in energy and, thus, as discussed in Chapter 1, the Wigner Delay is 0 as. In order to see and to test the robustness of reconstructing delays in photo-emission, more advanced model should be used, like [45].
The reconstructed XUV GDD is retrieved with a good degree of accuracy, in the worst case we have a relative error around the 4% with a GGD=0.0096 fs^2 instead of GDD=0.01 fs^2.
The FWHM$_{XUV}$ is tricky, in fact, as shown in table 4.3 we have a good convergence, with an accuracy below the available time-resolution, only for traces calculated without dipole. However, the registered change in the reconstructed XUV duration is not an effect caused by the ensemble effect. In fact, it is the manifestation of a non-flat dipole, whose role is to narrow the frequency bandwidth of the atomic field, E_{at} in Chapter 1, which is the real effective field reconstructed by ePIE. Therefore, we can claim that, due to the stability against the ensemble effect of the reported FHWM$_{XUV}$ the robustness of ePIE in the XUV reconstruction is proved. The FWHM$_{IR}$ is also retrieved with a relatively good degree of accuracy, worst case 4% of error, however, as it will be shown in the example, at a lower IR radius the final shape of the IR profile becomes less accurate. This effect is probably introduced by the incapability of ePIE to reconstruct the asymmetry introduced by the ensemble effect.

1) **Argon No Dipole No GDD**

	$25\mu m$	$50\mu m$	$100\mu m$	$200\mu m$	FLAT
β_R	0.095	0.095	0.095	0.095	0.095
β_P	0.045	0.045	0.045	0.045	0.045
A_0	2.5	3.5	3.5	4.5	4.5
τ_g (as)	-14	-14	-16	-12	-10
GDD$_{XUV}$ (fs^2)	1.7e-6	1e-6	4e-6	5.9e-6	6e-6
FWHM$_{XUV}$(fs)	0.2518	0.2515	0.2518	0.252	0.2519
FWHM$_{IR}$ (fs)	9.60	9.89	10.06	10.01	10.01

2) **Argon No Dipole GDD**

	$25\mu m$	$50\mu m$	$100\mu m$	$200\mu m$	FLAT
β_R	0.011	0.095	0.095	0.095	0.095
β_P	0.04	0.045	0.045	0.045	0.045
A_0	2	3.5	3.5	4.5	4.5
τ_g (as)	3	4.2	3.6	0.1	2
GDD$_{XUV}$ (fs^2)	0.0097	0.0099	0.0101	0.01	0.01
FWHM$_{XUV}$(fs)	0.2520	0.2519	0.2520	0.2521	0.2521
FWHM$_{IR}$ (fs)	10.34	10.21	10.04	9.985	10.01

3) **Argon with Dipole No GDD**

	$25\mu m$	$50\mu m$	$100\mu m$	$200\mu m$	FLAT
β_R	0.095	0.095	0.095	0.095	0.095
β_P	0.042	0.045	0.045	0.045	0.045
A_0	2	3.5	3.5	4.5	4.5
τ_g (as)	14.05	3.80	6	0.6	0.6
GDD$_{XUV}$ (fs^2)	3e-7	3e-6	5e-6	7e-6	7e-6
FWHM$_{XUV}$(fs)	0.2708	0.2708	0.2709	0.271	0.271
FWHM$_{IR}$ (fs)	9.717	9.98	10.06	10.01	9.983

4) **Argon with Dipole with GDD**

	$25\mu m$	$50\mu m$	$100\mu m$	$200\mu m$	FLAT
β_R	0.095	0.095	0.095	0.095	0.095
β_P	0.042	0.045	0.045	0.045	0.045
A_0	2.5	3.5	3.5	4.5	4.5
τ_g (as)	14.05	3.80	6	0.6	0.6
GDD$_{XUV}$ (fs^2)	0.0096	0.0099	0.0101	0.01	0.01
FWHM$_{XUV}$(fs)	0.2709	0.2709	0.271	0.271	0.271
FWHM$_{IR}$ (fs)	10.4	9.83	10.01	9.985	9.985

TABLE 4.2: ePIE results for the four main simulations. In those simulation a simple dipole model, with flat phasee profile, has been used.

A relative error as a reconstruction accuracy figure can be evaluated as:

$$REError(\%) = 100\left|\frac{RValue - IValue}{IValue}\right| \tag{4.2}$$

where $RValue$ is the reconstructed value at a certain rFHWM, and $IValue$ is the input value.

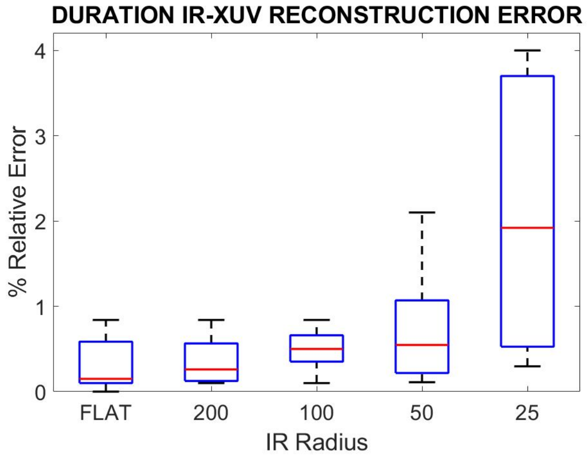

FIGURE 4.5: Boxplot of the reconstruction error in the FWHM of IR and XUV. In the case with the dipole, an atomic field FWHM=0.2680 has an estimation of the ideal value for the error calculation. An increase of the reconstruction error can be observed for decreasing value of the IR radius.

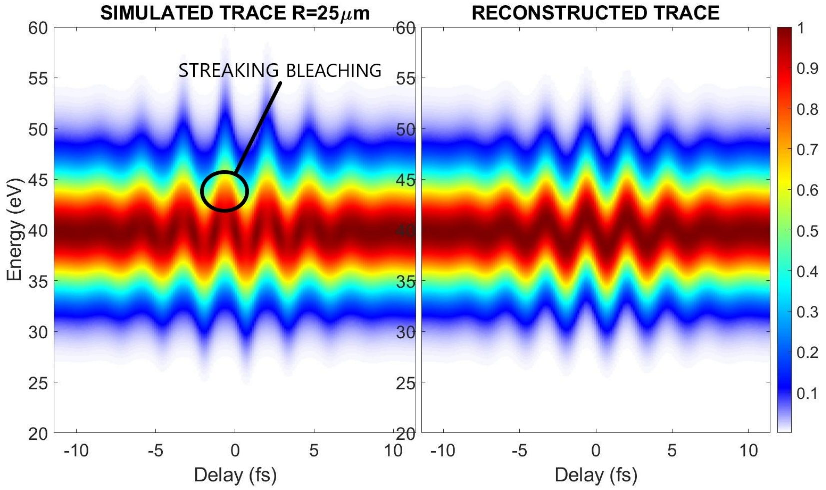

FIGURE 4.6: Confrontation between a simulated trace at 25 μm and the ePIE reconstructed trace, main simulation 3, Argon with Dipole and without any GDD$_{XUV}$. In the left panel, the " streaking emptying" ensemble effect can be observed. This effect is completely absent in the reconstructed trace, right-hand side panel. ePIE algorithm cannot reconstruct this spacial asymmetry in the trace. This effect causes a higher inaccuracy, averagely 400 as, in the reconstruction of the temporal IR-field FWHM, as well in a less precise retrieved electric field profile. The streaking trace is plotted without the jacobian factor, and as a function of the photon energy, as the ePIE software required as an input to work properly.

4.2.1 Analysis of ensemble effects in an ePIE reconstruction

In the following, I will present an example of a trace reconstruction with ePIE, using the same the simulation of the previous example sub-section: Argon with a simple dipole transition element, calculated from 3p0 to plane wave state and GDD in the XUV field.
As shown in Figure 4.7, after feeding ePIE with SFEXIS's traces, a good trace convergence can be observed for rFWHMs of 100 μm and 200 μm. Instead, for 50 μm and 25 μm, by comparing the simulation with the reconstructed trace some differences can be easily perceived by the eye. In particular, ePIE is unable to reconstruct asymmetric features in streaking traces, this is an already reported general fact [19], which is reasonably a consequence of the approximations behind the algorithm, like the Central Momentum Approximation. Finally, the evaluation of the ensemble effects are presented in Figure 4.8, by plotting for each of the non-flat case the difference with the ePIE-reconstructed flat trace. In Figure 4.9, the spectral phase and spectral amplitude of the reconstructed field (XUV times a dipole term) are shown together with the fitting curve used to retrieve the GDD. As already discussed, the "wrong" reconstructed value for the XUV FWHM is a consequence of the introduction of a transition dipole element which brings, in our simulated case, the reconstructed duration from 250 as to 270 as. This is a relevant effect in experiments that can be, however, removed in post-processing, if an accurate model for the dipole transition element is known a priori.

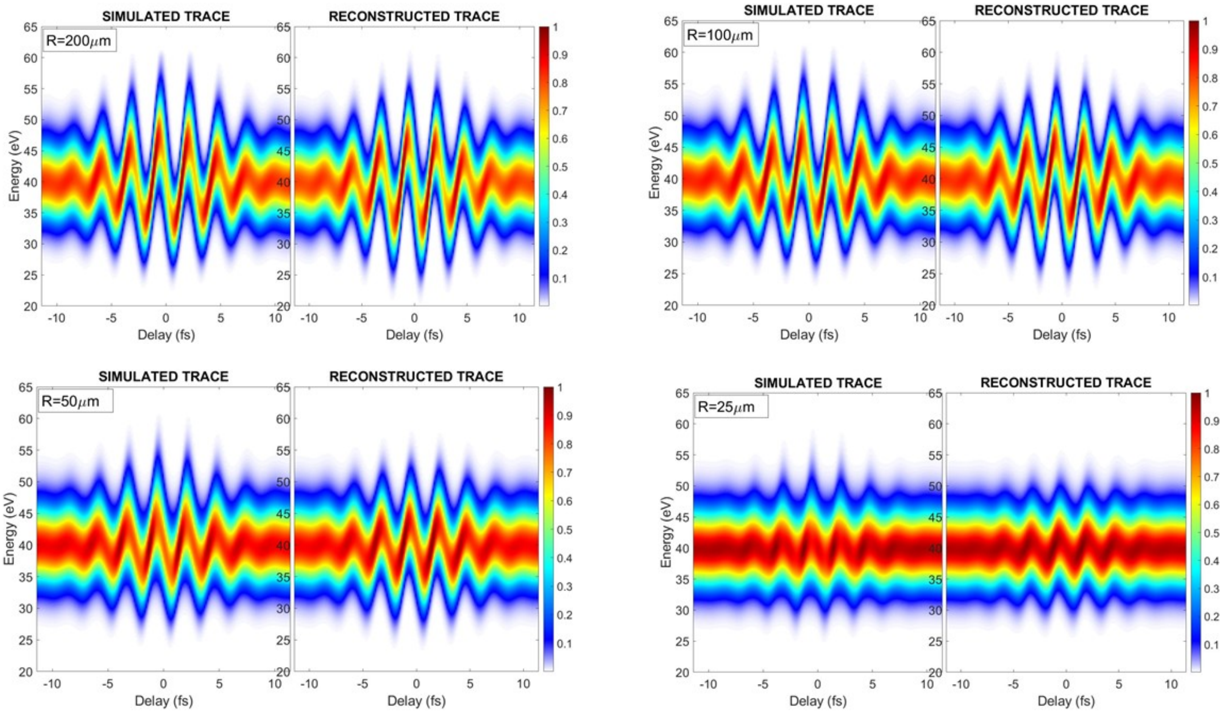

FIGURE 4.7: Simulated trace in SFEXIS, simulation number 4, vs Reconstructed trace in ePIE for different IR radius. Without the jacobian factor and as a function of the photon energy.

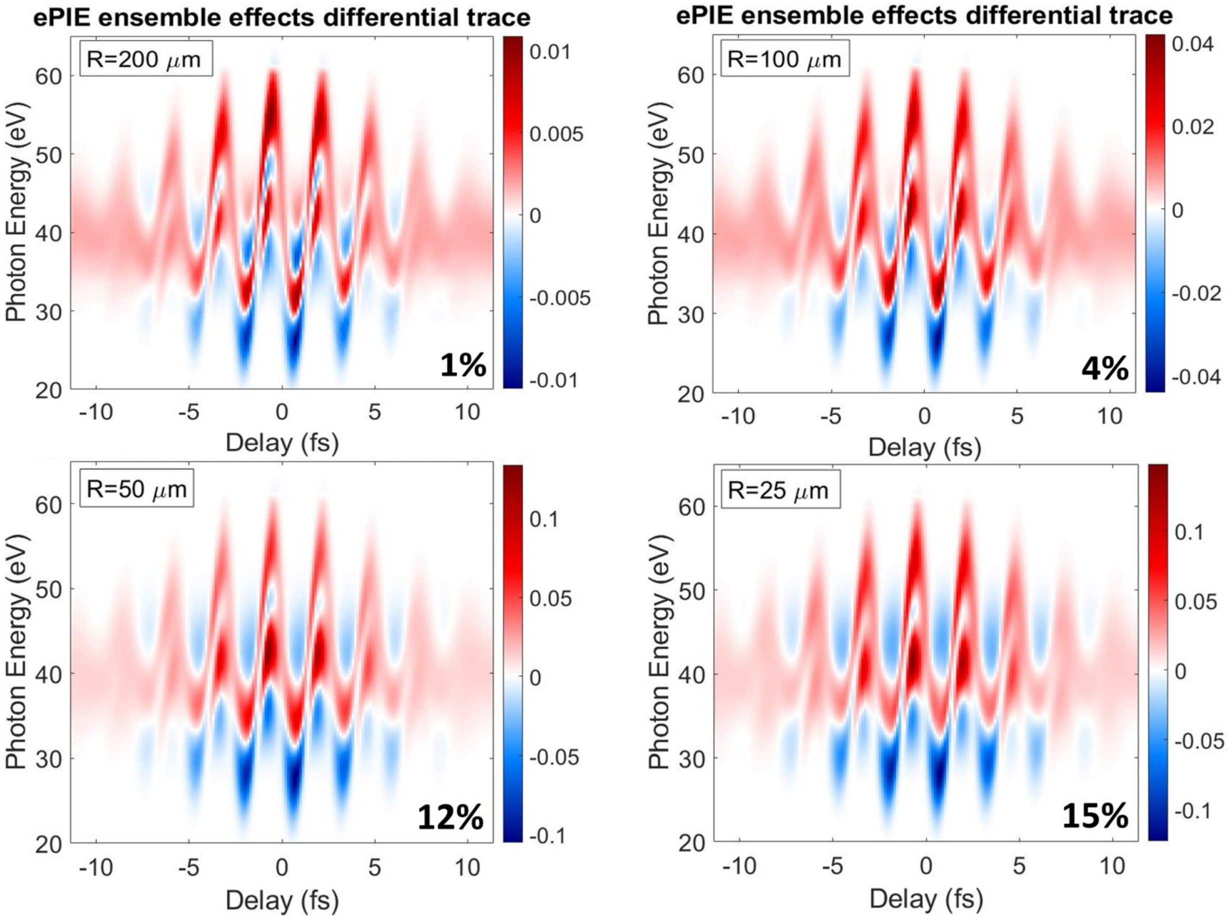

FIGURE 4.8: Evaluation of ensemble effect relative reconstruction error by evaluating the difference between the reconstructed field in the flat case and the field with a given rFHWM. As it can be observed by comparing this figure to Figure 4.4 where the ensemble effects introduce a distortion in the real trace up to the 60%, ePIE reconstruction is robust and keeps the reconstruction closer to the ideal case, with a relative error up to the 15%.

In Figure 4.10, instead, the reconstructed IR pulse, extracted from the gate function, is presented for different radius, from the flat case down to 25 μm . The algorithm retrieves the IR profile with a higher degree of accuracy, at least within the chosen temporal resolution, for 100 μm and 200 μm. A discrepancy between the retrieved and original electric fields is observed for lower radius, 50 μm and 25 μm. As already presented in table 4.3, the induced error on the IR FHWM does not overcome the 4% of relative error.

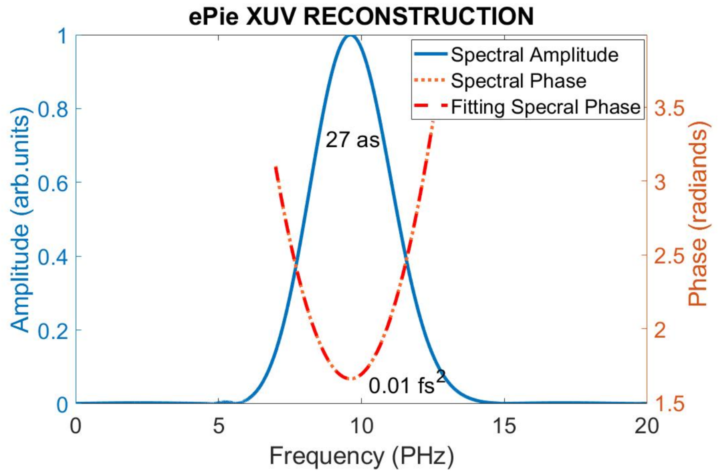

FIGURE 4.9: Reconstructed XUV (atomic field) spectrum in phase and in amplitude at rFWHM of 100 μm.

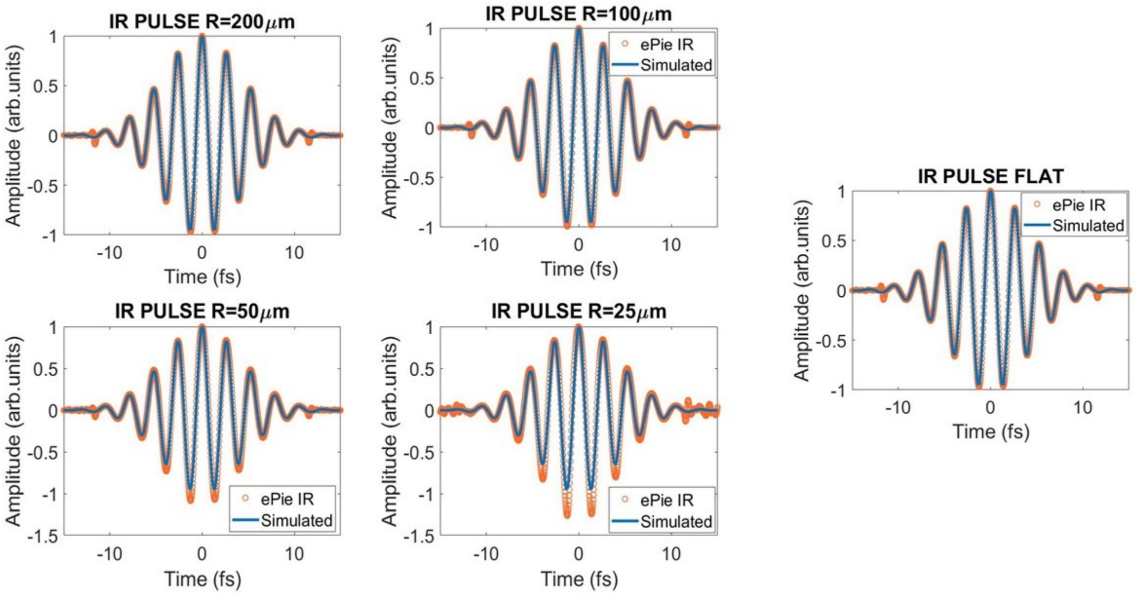

FIGURE 4.10: Comparison between ePIE reconstructed IR field and simulated IR-field for different value of the IR radius.

Ensemble effect on photo-emission delay

An additional fifth-simulation will now be considered.
This time, as presented and discussed in Chapter 3, the "mixed" model for the dipole transition element will be used. This allows us to evaluate the impact of ensemble effect on photo-emission delay, since the phase of the dipole is no more flat.
From the discussion in Chapter 1, we know that ePIE reconstructs an atomic field $\tilde{E}_{at}$, of the form:

$$\tilde{E}_{at}(\epsilon) = \mathcal{F}(E_{at}(t)) = d(\epsilon)\tilde{E}_{XUV}(\omega) = \sigma(\epsilon)e^{i\varphi(\epsilon)}\tilde{E}_{XUV}(\epsilon + I_P) \tag{4.3}$$

The photo-emission delay is, then, evaluated through the Wigner time-delay, τ_W, which, as discussed in Chapter 2 is defined as

$$\tau_W(\epsilon) = \frac{\partial \varphi(\epsilon)}{\partial \epsilon} \tag{4.4}$$

τ_W can be seen as a group delay applied on the XUV, τ_g, which will be our photo-emission delay. Thus, we write:

$$\tilde{E}_{at}(\omega) = \mathcal{F}(E_{at}(t)) \approx \sigma(\omega) e^{i\tau_g(\omega - \omega_{XUV})} \tilde{E}_{XUV}(\omega) \tag{4.5}$$

which now can be evaluated as in Figure 4.9.
We can also estimate the input photo-emission delay of value by evaluating the slope at the central electron energy of the XUV, around 23 eV, from Figure 4.11. As a result, the input photo-emission delay should be approximately -30 as .

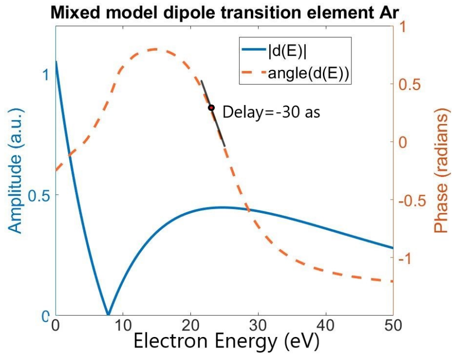

FIGURE 4.11: Mixed model for the dipole transition element, discussed in Chapter 3. The photo-emission delay is evaluated as the slope centred at 23 eV, the central frequency of the XUV attosecond pulse minus the ionization potential of the interaction species.

As before ePIE reconstruct accurately all the spectral parameter from the XUV GDD to the FWHM of the IR. The reconstruction accuracy on the photo-emission delay is this time less accurate with an error up to the 17%, which correspond to 11 as, a big time for accurate attosecond measurements.

Argon with mixed dipole and GDD

	$25\mu m$	$50\mu m$	$100\mu m$	$200\mu m$	FLAT
β_R	0.095	0.095	0.095	0.095	0.095
β_P	0.043	0.045	0.045	0.045	0.045
A_0	2	3	4	4	4
τ_g (as)	-19.1	-26.4	-23.7	-23.2	-24.4
GDD$_{XUV}$ (fs^2)	0.0096	0.0099	0.0103	0.01	0.01
FWHM$_{XUV}$(fs)	0.2708	0.2708	0.271	0.271	0.271
FWHM$_{IR}$ (fs)	10.54	10.2	10.04	10.01	10.01

TABLE 4.3: ePIE results for the "mixed" dipole simulation.

4.3 ePIE robustness conclusions

In conclusion of this Chapter, if our objective is to have access just to the fields' information hidden in a photo-electron streaking trace, FWHM$_{IR}$ FHWM$_{XUV}$ and GDD, then, *ePIE is robust to the ensemble effect*.

Indeed, even in the worst-case scenario 25 μm, in which we are introducing trace variation up to the 60% with respect the flat case, ePIE reconstruction relative error on the reconstructed trace (evaluated as the difference between the flat case and the non-flat case) does not overcome the 15%, while the relative error on the field parameters, evaluated as the difference between the input value and the reconstructed value, is at most around the 4%, see Figure 4.5.

Therefore, we can claim that in an attosecond photo-electron experiment, where a quantum dynamics of few-hundreds of attosecond is investigated, the ensemble effects introduce just a minor error which can be neglected in most of the case, or eventually tackled in data post-processing.

For higher needed time-resolution of tens of attosecond, as for the reconstruction of photo-emission delay, ePIE presents a higher level of inaccuracy, around 20% of relative error with respect the expected result, which corresponds to 10 as in the presented case.
This is could be due to one, or a combination of the following causes:

- The time resolution used for the ePIE reconstructions, which is limited by our simulation time resolution, which was limited by available computation power, is not high enough to give us accurate information on the atomic delay.
- The approximations on which ePIE is based, like CMA, are an additional source of errors, that do not allow an accurate reconstruction of photo-emission delay; hence a different approach to time-delay reconstruction should be used.
- For a short pulse with a bandwidth that spans 10 eV, the expansion used in Eq. (4.5) to calculate the photo-emission delay may not be an accurate way of estimating the photo-emission delay, since higher-order terms in the phase may also influence the reconstruction accuracy.

Chapter 5

Future Development and Conclusions

In this thesis work, I have developed a code for the simulation of photo-electron streaking traces capable of including ensemble effects. Moreover, I have implemented an improved model for the calculation of the dipole transition moment (the existing software worked under the approximation of a unitary dipole moment).
Ensemble effects have been up to now neglected in literature since most codes work under the approximation of a flat spatial profile. While this approximation is justified, for a single atom interaction or a small XUV focus with respect the IR, in real experiments it could lead to an inaccurate result, so its effects must be studied.
The programme I have implemented overcomes this bottleneck by computing and, then, averaging many streaking traces for each position of the intensity profiles, for given beams radii. The so-generated streaking traces have been used to test the robustness of the reconstruction algorithm ePIE.

In particular, I have presented the limits of the reconstruction algorithm ePIE against this non-ideality. I have demonstrated that in the worst-case scenario (a Gaussian profile of the IR field with a FWHM of 25 μm), the retrieved pulses are estimated within an error of 4%. In spite of being a relatively small error, it could be particularly important when proprieties like photo-emission delays are evaluated, in fact a lower reconstrucion accuracy have been estimated around the 20%.

Future developments of this work include:

1) To decrease the temporal resolution of the simulations and use more advance models to evaluate the impact of ensemble effects on retrieved photo-emission delay.

2) To simulate the volume (3D) effects on photo-electron streaking traces, including the field wavefronts.

In fact, so far, I have studied 2D ensemble effects of fields with just a non-flat amplitude profile. Hence, I have disregarded the impact of IR and XUV real phase profiles, which are not flat, and, also, the possible 3D ensemble effects, or volume effects caused by a 3D gas jet.
If these ensemble effects become a bottleneck in scaling down the temporal resolution, then, strategies to overcome them in post-processing will be also discussed

and implemented in ePIE, similarly, as Gaumnitz and co-workers did for angular averaging [23] in a similar reconstruction algorithm.

Appendix A

Quantum Mechanics Tools

In the following, I will cover different and important results that are used extensively throughout this work, and are the guide for a correct and formal discussion on semiclassical light-matter interaction.
Many discussions and demonstrations have been re-adapted from [24, 48] and [38]. Other results, instead, have been derived by my self and, therefore, to my knowledge, lack of literature support. However, they are strengthened by the math used, the physical meaning behind, and the coherence of the final result with the existing one.

As final comments, in all the discussion the *Shrödinger picture* and atomic units are adopted.

A.1 Quantum States and Operator Spectrum

The collection of all the possible values that a generic quantum object can assume, in a certain problem framework, is called *eigenvalues spectrum*.
In quantum physics we can have:

- Continuous set of eigenvalues, *continuous spectrum*
- Discrete set of eigenvalues, *discrete spectrum*
- Mixed set of eigenvalues [38], continuous and discrete spectrum are present in different non-overlapping spectral regions.

The latter case is common in many problems where an electromagnetic field interacts with a quantum system, as Landau did for a static electric field [38], but it also appears in a more general discussion on scattering states and partial waves, see Chapter 6 [24].

This is, in general, not easy and, therefore, one, usually, never encounters this mixed states, but, instead, use a redundant (non-orthogonal) basis system, e.g. free electron states and the atom bound states.

The ket space

In the modern formulation of quantum mechanics (QM) [24, 48], a state is postulated to be an entity $|\alpha\rangle$ which contains complete information about the physical system that is describing. This entity is called ket-state $|\alpha\rangle$ and it belongs to a certain Hilbert space, in which we have constructed the scalar product as $\langle\alpha|\beta\rangle = \langle\beta|\alpha\rangle^*$.

A state is something profoundly different from its representation in a certain basis set, like the familiar wavefunction representation, discussed later.

Indeed, not all quantum system posses a wavefunction representation, like, for instance, spin-state or a photon-state, see [49, 50].
This split between the state and its representation is clarified later by discussing the different spectra in the Dirac notation. As a marginal note, despite its elegance, Dirac notation *does not give* any new meaning to a non-relativistic semi-classical atom-light interaction system, and therefore a wavefunction formulation is still appropriate in the description, see [38].

Discrete spectrum

Let us consider a set of eigenstates forming a complete discrete spectrum f_n for a certain quantum operator $\hat{f}$. Then, $|\alpha_n\rangle$ is the state in which a certain physical quantity, associated with the operator $\hat{f}$, assumes the value f_n and, hence, satisfies:

$$\hat{f}\,|\alpha_n\rangle = f_n\,|\alpha_n\rangle \tag{A.1}$$

Thanks to completeness propriety [24], a generic state, which belongs to the same space, can be written as a superposition of $|\alpha_n\rangle$.

$$|\psi\rangle = \sum_n a_n |\alpha_n\rangle \tag{A.2}$$

with, according to Bohm's interpretation of QM:

$$\langle\psi|\psi\rangle = 1$$

As a consequence of the orthogonality for the eigenstates of Eq. (A.1), we have the trivial result:

$$\langle\alpha_n|\alpha_m\rangle = \delta_{nm} \tag{A.3}$$

where δ_{nm} is the Kronecker delta.
Hence, it holds

$$\langle\psi|\psi\rangle = \sum_n a_n^* \langle\alpha_n|\psi\rangle \sum_n a_n^* a_n = 1 \tag{A.4}$$

Usually the problem is backwardly formulated, hence we have a certain operator, and we want to derive completeness and orthogonality of its eigenstates. This is not an easy task and particular care must be used[1]. What physicists usually rely on is that the eigensolution of a given quantum problem forms a complete basis set in a well-defined Hilbert space.

Continuous spectrum

Let us now consider f as a physical quantity with, instead, a complete and continuous spectrum of eigenvalues f, and with associated eigenstates $|\psi_f\rangle$. As before, we are solving a certain eignevalues problem

$$\hat{f}\,|\psi_f\rangle = f\,|\psi_f\rangle \tag{A.5}$$

In analogy with the discrete case, we can generalize the completeness in the following way:

$$|\psi\rangle = \int c(f)\,|\psi_f\rangle\,df \tag{A.6}$$

Mind that since the quantum interpretation of $|\psi\rangle$ must remain the same, i.e. normalization,

$$\langle\psi|\psi\rangle = 1$$

then the only compatible option is:

$$\langle\psi_f|\psi_{f'}\rangle = \delta(f - f') \tag{A.7}$$

---

[1] See footnote at page 38 of [24].

where $\delta(f-f')$ is the Dirac delta.
This implies:

$$\int |c(f)|^2 df = 1 \tag{A.8}$$

$|c(f)|^2 df$ is so the probability density that $|\psi\rangle$ is in the state in which the physical quantity is between f and $f+df$.
It follows:

$$c(f) = \langle \psi_f | \psi \rangle \tag{A.9}$$

Mixed spectrum

A mixed spectrum is a peculiar condition in which we have two different regimes that solves the same equation depending on the region of interest [38]. As a matter of fact, the completeness of this space can be written as:

$$|\psi\rangle = \sum a_n |\alpha_n\rangle + \int c(f) |\psi_f\rangle \, df \tag{A.10}$$

and for orthogonality:

$$\begin{aligned}\langle \alpha_n | \alpha_m \rangle &= \delta_{nm} \\ \langle \psi_f | \psi_{f'} \rangle &= \delta(f-f') \\ \langle \psi_f | \alpha_n \rangle &= 0\end{aligned}$$

A.1.1 Basis change and wavefunction representation

Position space

Let us consider the full set of position ket, which solves

$$\hat{\mathbf{r}} |\tilde{\mathbf{r}}\rangle = \tilde{\mathbf{r}} |\tilde{\mathbf{r}}\rangle \tag{A.11}$$

where $\hat{\mathbf{r}}$ is the operator position introduced in Appendix A, and $\tilde{\mathbf{r}}$ is the particle position, which is a vector in $\mathcal{R}^3$.

Without too much regard on the true meaning of this quantum state, $|\tilde{\mathbf{r}}\rangle$, let us apply all the aforementioned results on a continuous basis. If we can claim that the position ket is a complete basis of the functional space [24, 48], then:

$$\langle \tilde{\mathbf{r}} | \tilde{\mathbf{r}}' \rangle = \delta(\tilde{\mathbf{r}} - \tilde{\mathbf{r}}') \tag{A.12}$$

and for Eq. (A.9)

$$|\psi\rangle = \int \langle \mathbf{r} | \psi \rangle \, |\mathbf{r}\rangle \, d\mathbf{r} \tag{A.13}$$

where $\langle \mathbf{r} | \psi \rangle = \psi(\mathbf{r})$.
Moreover, due to Eq. (A.8), $|\psi(\mathbf{r})| d^3 r$ become the probability that the state is projected in the position state identified by $\mathbf{r}$ and $\mathbf{r} + d\mathbf{r}$.
As a consequence, $\langle \mathbf{r} | \psi \rangle = \psi(\mathbf{r})$ assume the meaning of the system *wavefunction*.

Then, a generic expectation value is be calculated as:

$$\langle\psi|\,\hat{A}\,|\psi\rangle = \int \langle\psi|\mathbf{r}\rangle\,\hat{A}(\mathbf{r})\,\langle\mathbf{r}|\psi\rangle\,d\mathbf{r} = \int \psi^*(\mathbf{r})\hat{A}(\mathbf{r})\psi(\mathbf{r})d\mathbf{r} \tag{A.14}$$

Momentum space

We can proceed in an analogous way with the conjugated variable of position, momentum $\hat{\mathbf{p}}$.

$$\hat{\mathbf{p}}\,|\tilde{\mathbf{p}}\rangle = \tilde{\mathbf{p}}\,|\tilde{\mathbf{p}}\rangle \tag{A.15}$$

where $|\tilde{\mathbf{p}}\rangle$ is the quantum state with momentum $\tilde{\mathbf{p}}$
Then, it is also true that:

$$\langle\tilde{\mathbf{p}}|\tilde{\mathbf{p}}'\rangle = \delta(\tilde{\mathbf{p}} - \tilde{\mathbf{p}}') \tag{A.16}$$

With similar argumentation as before, we can write the generic quantum state $|\psi\rangle$ as a superposition of momentum states weighted by $\langle\mathbf{p}|\psi\rangle$ $\mathbf{p}$:

$$|\psi\rangle = \int \langle\mathbf{p}|\psi\rangle\,|\mathbf{p}\rangle\,d\mathbf{p} \tag{A.17}$$

here $\langle\mathbf{p}|\psi\rangle = \phi(\mathbf{p})$ is the wave-function in the momentum space, p-space, or, in other terms $|\phi(\mathbf{p})|^2 d\mathbf{p}$ is the probability to find the quantum states with momentum between $\mathbf{p}$ and $\mathbf{p} + d\mathbf{p}$.

It is now natural to ask themselves, which is the representation of $|\mathbf{r}\rangle$ in the p-space $|\mathbf{p}\rangle$, and viceversa.

The former sounds a bit strange, but it answers the question which is the momentum projection of a quantum state with a well-defined position, the latter, instead, tells which is the projection in the position space of a quantum state with a well-defined momentum.
For completeness of the p-space, it holds,

$$|\mathbf{r}\rangle = \int \langle\mathbf{p}|\mathbf{r}\rangle\,|\mathbf{p}\rangle\,d\mathbf{p} \tag{A.18}$$

In order to find the expression $\langle\mathbf{p}|\mathbf{r}\rangle$, we focus on the 1D projection in the x-direction.

Let us evaluate the matrix element [24], of the

$$\langle x|\,\hat{\mathbf{p}}\,|p_x\rangle = -i\frac{\partial}{\partial x}\langle x|p_x\rangle \tag{A.19}$$

where we have exploited the definition of momentum operator[48] in the x-position space.
But, it is also true that:

$$\langle x|\,\hat{\mathbf{p}}\,|p_x\rangle = p_x\,\langle x|p_x\rangle$$

As a consequence,

$$p_x \langle x|p_x\rangle = -i\frac{\partial}{\partial x}\langle x|p_x\rangle \tag{A.20}$$

The solution is straightforward,

$$\langle x|p_x\rangle = c_1 e^{ip_x x} \tag{A.21}$$

with c_1 a constant.
Since the three dimension of space and momentum are independent, we have

$$\langle \mathbf{r}|\mathbf{p}\rangle = \langle x|p_x\rangle \langle y|p_y\rangle \langle z|p_z\rangle = c_3 e^{i\mathbf{p}\cdot\mathbf{r}} \tag{A.22}$$

with c_3 another constant.
By definition of scalar product in quantum mechanics:

$$\langle \mathbf{p}|\mathbf{r}\rangle = c_3^* e^{-i\mathbf{p}\cdot\mathbf{r}} \tag{A.23}$$

The normalization constant, c_3, can be retrieved imposing:

$$\langle \mathbf{r}|\mathbf{r}\rangle = \int \langle \mathbf{r}|\mathbf{p}\rangle \langle \mathbf{p}|\mathbf{r}\rangle \, d\mathbf{p} = 1 \tag{A.24}$$

where, once again we have used the completeness of momentum space $\mathcal{I} = \int |\mathbf{p}\rangle\langle\mathbf{p}|\, d\mathbf{p}$, where $\mathcal{I}$ is the identity operator.
As a result,

$$\langle \mathbf{r}|\mathbf{p}\rangle = \frac{1}{(2\pi)^{\frac{3}{2}}} e^{+i\mathbf{p}\cdot\mathbf{r}} \tag{A.25}$$

$$\langle \mathbf{p}|\mathbf{r}\rangle = \frac{1}{(2\pi)^{\frac{3}{2}}} e^{-i\mathbf{p}\cdot\mathbf{r}} \tag{A.26}$$

We are now able to write a fundamental relation between the wavefunction in position space and the wavefunction in the momentum space:

From,

$$|\psi\rangle = \int \langle \mathbf{p}|\psi\rangle |\mathbf{p}\rangle \, d\mathbf{p} = \int \langle \mathbf{r}|\psi\rangle |\mathbf{r}\rangle \, d\mathbf{p}$$

It easy to show that

$$\psi(\mathbf{r},t) = \frac{1}{(2\pi)^{\frac{3}{2}}} \int \phi(\mathbf{p},t) e^{i\mathbf{p}\cdot\mathbf{r}} d\mathbf{p} \tag{A.27}$$

We are now ready to discuss the Shrödinger equation in different projection spaces, which is extremely useful when dealing with tunneling phenomena. The general form of Shrödinger equation, in atomic units, is:

$$\hat{H}|\psi\rangle = i\frac{\partial}{\partial t}|\psi\rangle \tag{A.28}$$

So far we didn't say anything about time, according to the standard interpretation of quantum mechanics, time is not an observable; it is, just, a scalar parameter.

This is the reason why, in the interaction and Shrödinger picture a state is often indicated as $|\psi, t\rangle$ or $|\psi(t)\rangle$.

Shrödinger equation: position projection

The spatial projection of Eq. (A.28) is:

$$\langle \mathbf{r}| \hat{H} |\psi(t)\rangle = i\frac{\partial}{\partial t} \langle \mathbf{r}|\psi(t)\rangle = i\frac{\partial}{\partial t}\psi(\mathbf{r}, t) \tag{A.29}$$

where we have used in the last term the result achieved in previous discussion on position space.

Now, if the hamiltonian $\hat{H}$ can be written as:

$$\hat{H}(\hat{\mathbf{r}}, \hat{\mathbf{p}}, t) = \hat{H}_A(\hat{\mathbf{r}}, t) + \hat{H}_B(\hat{\mathbf{p}}, t) \tag{A.30}$$

then, we can exploit linearity and the completeness of position space, and, hence, write:

$$\int \langle \mathbf{r}| \hat{H} |\tilde{\mathbf{r}}\rangle \langle \tilde{\mathbf{r}}|\psi\rangle \, d\tilde{\mathbf{r}} = \int \langle \mathbf{r}| \hat{H}_A(\hat{\mathbf{r}}, t) |\tilde{\mathbf{r}}\rangle \langle \tilde{\mathbf{r}}|\psi\rangle \, d\tilde{\mathbf{r}} + \int \langle \mathbf{r}| \hat{H}_B(\hat{\mathbf{p}}, t) |\tilde{\mathbf{r}}\rangle \langle \tilde{\mathbf{r}}|\psi\rangle \, d\tilde{\mathbf{r}} =$$
$$= \int \hat{H}_A(\tilde{\mathbf{r}}, t) \langle \mathbf{r}|\tilde{\mathbf{r}}\rangle \langle \tilde{\mathbf{r}}|\psi\rangle \, d\tilde{\mathbf{r}} + \int \hat{H}_B(-i\hbar\frac{\partial}{\partial \tilde{r}}, t) \langle \mathbf{r}|\tilde{\mathbf{r}}\rangle \langle \tilde{\mathbf{r}}|\psi\rangle \, d\tilde{\mathbf{r}} = \hat{H}\psi(\mathbf{r}, t)$$

As a result:

$$\boxed{\hat{H}\psi(\mathbf{r}, t) = i\frac{\partial}{\partial t}\psi(\mathbf{r}, t)} \tag{A.31}$$

we have, then, achieved the basic quantum mechanics Shrödinger equation, which is a partial differential equation that takes as an input a complex function (wavefunction!), in space and time.

Shrödinger equation: momentum projection

We can follow a similar procedure in the momentum space and, thus, evaluates:

$$\langle \mathbf{p}| \hat{H} |\psi(t)\rangle = i\frac{\partial}{\partial t} \langle \mathbf{p}|\psi(t)\rangle = i\phi(\mathbf{p}, t) \tag{A.32}$$

with $\phi(\mathbf{p}, t)$ the wavefunction in momentum space. If, as before, the hamiltonian $\hat{H}$ can be written as:

$$\hat{H}(\hat{\mathbf{r}}, \hat{\mathbf{p}}, t) = \hat{H}_A(\hat{\mathbf{r}}, t) + \hat{H}_B(\hat{\mathbf{p}}, t) \tag{A.33}$$

Then,

$$\langle \mathbf{p}| \hat{H} |\psi(t)\rangle = \langle \mathbf{p}| \hat{H}_A(\hat{\mathbf{r}}, t) |\psi(t)\rangle + \langle \mathbf{p}| \hat{H}_B(\hat{\mathbf{p}}, t) |\psi(t)\rangle \tag{A.34}$$

the latter term of Eq. (A.34) is easy to be tackled, indeed, for hermiticity it holds:

$$\langle \mathbf{p}| \hat{H}_B(\hat{\mathbf{p}}, t) |\psi(t)\rangle = \hat{H}_B(\mathbf{p}, t)\phi(\mathbf{p}, t) \tag{A.35}$$

the former term of Eq. (A.34) requires more effort.

The preliminary step is to introduce the following operator identity:

$$\boxed{\hat{H}_A(\hat{\mathbf{r}},t)=\int\tilde{H}_A(\tilde{\mathbf{p}},t)e^{+i\tilde{\mathbf{p}}\cdot\hat{\mathbf{r}}}d\tilde{\mathbf{p}}} \tag{A.36}$$

We have written the hamiltonian operator, as a *Fourier transform* with $\tilde{\mathbf{p}}$ a parameter and $\tilde{H}_A(\tilde{\mathbf{p}},t)$ the weight-function of the operator $e^{+i\tilde{\mathbf{p}}\cdot\hat{\mathbf{r}}}$.

This peculiar operator must interpreted as:

$$e^{+i\tilde{\mathbf{p}}\cdot\hat{\mathbf{r}}}=\sum_n\frac{(i\tilde{\mathbf{p}}\cdot\hat{\mathbf{r}})^n}{n!} \tag{A.37}$$

The identity expressed in Eq. (A.36) holds since the two operators act in the same way on states, indeed, if we evaluate the action on the position

$$e^{+i\tilde{\mathbf{p}}\cdot\hat{\mathbf{r}}}|\tilde{\mathbf{r}}\rangle=\sum_n\frac{(i\tilde{\mathbf{p}}\cdot\hat{\mathbf{r}})^n}{n!}|\tilde{\mathbf{r}}\rangle=e^{+i\tilde{\mathbf{p}}\cdot\tilde{\mathbf{r}}}|\tilde{\mathbf{r}}\rangle \tag{A.38}$$

$$\hat{H}_A(\hat{\mathbf{r}},t)|\tilde{\mathbf{r}}\rangle=H_A(\tilde{\mathbf{r}},t)|\tilde{\mathbf{r}}\rangle \tag{A.39}$$

We are now ready to evaluate the first term in Eq. (A.34):

$$\langle\mathbf{p}|\hat{H}_A(\hat{\mathbf{r}},t)|\psi(t)\rangle \tag{A.40}$$

The next step is to calculate

$$\langle\mathbf{p}|e^{i\tilde{\mathbf{p}}\cdot\hat{\mathbf{r}}}=\int\langle\mathbf{p}|e^{i\tilde{\mathbf{p}}\cdot\hat{\mathbf{r}}}|\tilde{\mathbf{r}}\rangle\langle\tilde{\mathbf{r}}|d\tilde{\mathbf{r}}=\frac{1}{(2\pi)^{\frac{3}{2}}}\int e^{i(\tilde{\mathbf{p}}-\mathbf{p})\cdot\tilde{\mathbf{r}}}\langle\tilde{\mathbf{r}}|d\tilde{\mathbf{r}} \tag{A.41}$$

where we have used the completeness of position eigenstates and the result of Eq. (A.26). It follows:

$$\langle\mathbf{p}|\hat{H}_A(\hat{\mathbf{r}})=\int\tilde{H}_A(\tilde{\mathbf{p}},t)\langle\mathbf{p}|e^{+i\tilde{\mathbf{p}}\cdot\hat{\mathbf{r}}}d\tilde{\mathbf{p}}=\int\tilde{H}_A(\tilde{\mathbf{p}},t)d\tilde{\mathbf{p}}\frac{1}{(2\pi)^{\frac{3}{2}}}\int e^{i(\tilde{\mathbf{p}}-\mathbf{p})\cdot\tilde{\mathbf{r}}}\langle\tilde{\mathbf{r}}|d\tilde{\mathbf{r}} \tag{A.42}$$

As a result,

$$\langle\mathbf{p}|\hat{H}_A(\hat{\mathbf{r}},t)|\psi(t)\rangle=\frac{1}{(2\pi)^{\frac{3}{2}}}\int\tilde{H}_A(\tilde{\mathbf{p}},t)d\tilde{\mathbf{p}}\int e^{i(\tilde{\mathbf{p}}-\mathbf{p})\cdot\tilde{\mathbf{r}}}\psi(\tilde{\mathbf{r}},t)d\tilde{\mathbf{r}}$$

Exploiting the result of Eq. (A.27)

$$\langle\mathbf{p}|\hat{H}_A(\hat{\mathbf{r}},t)|\psi(t)\rangle=\int d\tilde{\mathbf{p}}H_A(\tilde{\mathbf{p}},t)\phi(\mathbf{p}-\tilde{\mathbf{p}},t)=H_A(\mathbf{p},t)*\phi(\mathbf{p},t) \tag{A.43}$$

where $*$ is the convolution product. This time, the result is less trivial, and we have that Eq. (A.32) become

$$\boxed{i\frac{\partial}{\partial t}\phi(\mathbf{p},t) = H_A(\mathbf{p},t) * \phi(\mathbf{p}) + H_B(\mathbf{p},t)\phi(\mathbf{p})} \tag{A.44}$$

This is the Shrödinger equation in momentum space, see Chapter 8 [51], and it is an integro-differential equation, which is not simple to handle.

As one can see, the hamiltonian, which originally depends on momentum, multiplies the wavefunction, while the hamiltonian which was expressed as a function of the *position* operator is, now, convoluted with the wavefunction.

A.2 Propagators, Dyson Equation and S-Matrix

Propagators

As already mentioned, in the modern formulation of QM, time is just a parameter [24]. This is the reason why we can have multiple "pictures" to discuss the evolution of states and operators, Shrödinger Picture, Heinseber Picture, Interaction Picture.
Although a time operator cannot be defined, we can introduce a *time-evolution operator*.

Assume you have a state initially defined as $|\alpha, t_0\rangle = |\alpha(t_0)\rangle$, then the time-evolution of this state, which leads to $|\alpha, t\rangle = |\alpha(t)\rangle$, can be regard as the application of an operator on the initial states.

$$|\alpha(t)\rangle = \hat{U}(t, t_0)\,|\alpha(t_0)\rangle \tag{A.45}$$

and

$$\langle\alpha(t)| = \langle\alpha(t_0)|\,\hat{U}^{\dagger}(t, t_0) \tag{A.46}$$

where $\hat{U}^{\dagger}$ is the hermitian conjugated operator of $\hat{U}$.
What is usually done at this point is to *derive* the *Shödinger equation* by starting from postulates on the proprieties that this peculiar time operator must have, see [24].
It is, however, more natural for an experimental physicist to start from the Shödinger equation and proceeding in the other way round, hence by deriving the time operator propriety as a consequence of the postulation of the Shödinger equation . Following the latter approach, we have:

$$i\frac{\partial}{\partial t}\,|\alpha(t)\rangle = \hat{H}\,|\alpha(t)\rangle \tag{A.47}$$

By applying Eq. (A.45) we have

$$i\frac{\partial}{\partial t}(\hat{U}(t, t_0)\,|\alpha(t_0)\rangle) = \hat{H}(\hat{U}(t, t_0)\,|\alpha(t_0)\rangle)$$

Due to the fact that $|\alpha(t_0)\rangle$ does not depend anymore on time t, then we can write an identity between two operators. So, we can infer that the two operators act in the same way on the initial state.

$$i\frac{\partial}{\partial t}\hat{U}(t, t_0) = \hat{H}\hat{U}(t, t_0) \tag{A.48}$$

Eq. (A.48) is commonly called *Shrödinger equation for the time-evolution operator* [27, 24].
Let us discuss, first, the case in which $\hat{H}$ does not depend on time $\hat{H} = \hat{H}_0$.

The solution is:

$$\hat{U}(t, t_0) = e^{-i\hat{H}_0(t-t_0)} \tag{A.49}$$

where the exponential operator must be treated in the following way:

$$e^{-i\hat{H}_0(t-t_0)} = \sum_n \frac{(-i\hat{H}_0(t-t_0))^n}{n!}$$

Thus,

$$|\alpha(t)\rangle = e^{-i\hat{H}_0(t-t_0)} |\alpha(t_0)\rangle \tag{A.50}$$

The consistency of this result will be proved later in the more general case, however one can already appreciate two things.
First, if $t = t_0$

$$e^{-\hat{0}} = \hat{\mathcal{I}} \tag{A.51}$$

we obtain the identity operator $\hat{\mathcal{I}} |\alpha(t_0)\rangle = |\alpha(t_0)\rangle$.
Second, if

$$\hat{H}_0 |\alpha_n\rangle = E_n |\alpha_n\rangle$$

then,

$$|\alpha(t)\rangle = e^{-iE_n(t-t_0)} |\alpha(t_0)\rangle \tag{A.52}$$

In other words, if $|\alpha\rangle$ is eigenstate of the time-independent hamiltonian, then we retrieve the usual time-dependence for an eigenstate[2].

The time evolution operator $\hat{U}(t, t_0)$ is, generally, called *propagator*, which is of fundamental interest in numerous field of modern physics.
Indeed, it is the starting of quantum field theory, scattering theories, QED, and of course of strong field light matter interaction, as I will discuss in a moment.

Let us generalize the result of Eq. (A.49), to the case in which, $\hat{H}(t)$, the hamiltonian operator is a function of the "parameter" time.
As a consequence, the solution of Eq. (A.48) is

$$\boxed{\hat{U}(t, t_0) = e^{-i\int_{t_0}^{t} \hat{H}(t')dt'}} \tag{A.53}$$

For the sake of completeness, let us prove that Eq. (A.53) is, indeed, solution of Eq. (A.48).
Let us start from the expansion of the time-derivative of the propagator $\hat{U}$:

$$i\frac{\partial \hat{U}}{\partial t} = i\frac{\partial}{\partial t}(e^{-i\int_{t_0}^{t} \hat{H}(t')dt'}) = i\frac{\partial}{\partial t}(\sum_{n=0}^{\infty}(-i\int_{t_0}^{t} \hat{H}(t')dt')^n \frac{1}{n!}) \tag{A.54}$$

Now, exploiting the following mathematical fact:
we have that for $n \neq 0$:

$$\frac{\partial}{\partial x}[\int_0^x f(y)dy]^n = \frac{\partial}{\partial x}[F(x) - F(0)] = \frac{\partial F(x)}{\partial x}[F(x) - F(0)]^{n-1} n$$

---

[2] In the Shrödinger picture, of course.

where x, y are parameters, and F, is the primitive of f.

$$\frac{\partial F(x)}{\partial x} = f(x)$$
$$[F(x) - F(0)] = \int_0^x f(y)dy$$

This implies:

$$\frac{\partial}{\partial x}[\int_0^x f(y)dy]^n = nf(x)(\int_0^x f(y)dy)^{n-1} \tag{A.55}$$

In the case in which $n = 0$, then, the derivative is clearly zero, so we end up in a trivial condition that does not create any problem.
So, by applying this result to Eq. (A.54) we achieve:

$$i\frac{\partial}{\partial t}\hat{U} = i\sum_{n=1}^{+\infty}\frac{(-i)^n}{n!}n\hat{H}(t)[\int_{t_0}^t \hat{H}(t')dt']^{n-1} = \hat{H}(t)\sum_{n=1}^{+\infty}\frac{(-i)^{n-1}}{(n-1)!}[\int_{t_0}^t \hat{H}(t')dt']^{n-1}$$

As a consequence, by re-scaling the summation to 0 we obtain the wanted result:

$$\boxed{i\frac{\partial}{\partial t}\hat{U} = \hat{H}\hat{U}} \tag{A.56}$$

Thus, proved the consistency of the result, we are ready to comment this very important outcome:

Through Eq. (A.53) we achieved a general exact solution for every non-relativistic quantum mechanical problem

Indeed, provided that we known the initial state, its evolution is given by

$$\boxed{|\alpha(t)\rangle = e^{-i\int_{t_0}^t \hat{H}(t')dt'}|\alpha(t_0)\rangle} \tag{A.57}$$

Despite its beauty, Eq. (A.57) its useless in most of the cases, with very few exceptions, as mentioned in Chapter 2, see also Appendix B.

Dyson Equations

The general goal, as mentioned in [12], is always to substitute the operator $\hat{H}(t')$ with a functional, which could depend, in general, on both time and space.
In order to achieve this goal, the brilliant idea [28, 27] was to reformulate the whole problem in easier terms, by splitting the hamiltonian in different contributions.

Let us now focus on the sub-set of problems that are of interest in strong field physics framework:

$$\hat{H} = \hat{H}_0 + \hat{H}_I(t) \tag{A.58}$$

Thus, we are discussing problems which composed by an time-independent hamiltonian, $\hat{H}_0$, which is typically kinetic energy term plus the Coulomb interaction, and by $\hat{H}(t)$, the interaction hamiltonian, which is an electro-magnetic field dependent term, typically in the dipole approximation[3].

Let us re-introduce the time-independent propagator $\hat{U}_0(t, t_0)$ as:

$$i\frac{\partial}{\partial t}\hat{U}_0(t, t_0) = \hat{H}_0\hat{U}_0(t, t_0) \tag{A.59}$$

Our goal is to find a better form for Eq.(A.57) by solving Eq.(A.56) in a different way.

First Dyson Equation

Thus, starting from Eq. (A.56), we write:

$$i\frac{\partial}{\partial t}\hat{U}(t, t_0) = \hat{H}\hat{U}(t, t_0) = (\hat{H}_0 + \hat{H}_I(t))\hat{U}(t, t_0)$$

it follows,

$$(i\frac{\partial}{\partial t} - \hat{H}_0)\hat{U}(t, t_0) = \hat{H}_I(t)\hat{U}(t, t_0) \tag{A.60}$$

In order to find a better looking solution for Eq. (A.60), we tackle the following bad-looking problem first:

$$(i\frac{\partial}{\partial t} - \hat{H}_0)\hat{G}_0(t, t') = \delta(t - t') \tag{A.61}$$

According to Green function theory [52] (Green operators, in our case), if we know $\hat{G}_0(t, t')$, then the exact solution of Eq.(A.60) can be written as [27, 28].

$$\hat{U} = \hat{U}_0(t, t_0) + \int_{t_0}^{t} \hat{G}_0(t, t')\hat{H}_I(t')\hat{U}(t', t_0)dt' \tag{A.62}$$

where we have added also the homogeneous solution term for the differential equation $\hat{U}_0$ from Eq. (A.59).

Let us now find the right form of $\hat{G}_0$ in an heuristic way under the $t > t'$ causality condition, which means that the perturbation happens before our final evolution time t, for a different and more advanced discussion see [28].

Defined the operator $\hat{G}_0(\omega, t')$, used in a different context by R.Loudon[49], as:

$$\hat{G}_0(t, t') = \frac{1}{2\pi}\int_{-\infty}^{+\infty} \hat{G}_0(\omega, t')e^{i\omega t}d\omega \tag{A.63}$$

---

[3] So that we can neglect any spatial dependence.

Then from Eq. (A.61):

$$(i\frac{\partial}{\partial t} - \hat{H}_0)\int \hat{G}_0(\omega, t')e^{i\omega t}d\omega = \delta(t - t') \tag{A.64}$$

and for linearity,

$$\int i\frac{\partial}{\partial t}(\hat{G}_0(\omega, t')e^{i\omega t}) - \hat{H}_0\hat{G}_0(\omega, t')e^{i\omega t}d\omega = \int(-\omega - \hat{H}_0)\hat{G}_0(\omega, t')e^{i\omega t}d\omega$$

If we Fourier transform the delta shifted at t', then Eq. (A.64) become:

$$\int(-\omega - \hat{H}_0)\hat{G}_0(\omega, t')e^{i\omega t}d\omega = \int e^{-i\omega t'}e^{i\omega t}d\omega \tag{A.65}$$

By imposing the equality between the integrands, we can retrieve the following equation:

$$\hat{G}_0(\omega, t') = -\frac{e^{-i\omega t'}}{\omega + \hat{H}_0} \tag{A.66}$$

Finally,

$$\hat{G}_0(t, t') = -\frac{1}{2\pi}\int \frac{1}{\omega + \hat{H}_0}e^{i\omega(t-t')}d\omega \tag{A.67}$$

If we apply the standard residual calculus[52] to Eq. (A.67) then, provided that $t > t'$, which as mentioned above is the physically meaningful condition, we achieve:

$$\hat{G}_0(t, t') = -ie^{-i\hat{H}_0(t-t')} = -i\hat{U}_0(t, t') \tag{A.68}$$

As a consequence,

$$\boxed{\hat{U}(t, t_0) = \hat{U}_0(t, t_0) - i\int_{t_0}^{t} \hat{U}_0(t, t')\hat{H}_I(t')\hat{U}(t', t_0)dt'} \tag{A.69}$$

Following this simple, and, to my knowledge, new approach the same equation that it would have been achieved with more advanced mathematical tools is derived.
Eq. (A.69) is called *first Dyson equation* [28].

Second Dyson Equation

It is less easy to show that also a *second Dyson equation* exists, which is the "time-reversed" with respect Eq. (A.69), since the different operators are now applied in the opposite way.
An heuristic way of proving it is by starting from:

$$\hat{H}_0 = \hat{H} - \hat{H}_I(t)$$

then,

$$i\frac{\partial}{\partial t}\hat{U}_0(t, t_0) = \hat{H}_0\hat{U}(t, t_0) = (\hat{H} - \hat{H}_I)\hat{U}_0(t, t_0)$$

Therefore, we can write:

$$(i\frac{\partial}{\partial t} - \hat{H})\hat{U}_0(t,t_0) = -\hat{H}_I\hat{U}_0(t,t_0) \tag{A.70}$$

At this point, we have reached a similar condition as in Eq. (A.60), hence:

$$(i\frac{\partial}{\partial t} - \hat{H}(t))\hat{G}_1(t,t') = \delta(t-t') \tag{A.71}$$

Exploiting, as before, Green function theory, we can write:

$$\hat{U}_0(t,t_0) = \hat{U}(t,t_0) - \int_{t_0}^{t} \hat{G}_1(t,t')\hat{H}_I(t')\hat{U}_0(t',t_0)dt'$$

or equivalently,

$$\hat{U}(t,t_0) = \hat{U}_0(t,t_0) + \int_{t_0}^{t} \hat{G}_1(t,t')\hat{H}_I(t')\hat{U}_0(t',t_0)dt' \tag{A.72}$$

where this time, $\hat{U}$ is our homogeneous solution for Eq. (A.71).
Finally, we can prove by substitution that the solution of Eq. (A.71) is:

$$\hat{G}_1(t,t') = -ie^{-i\int_{t'}^{t}\hat{H}(t'')dt''} = -i\hat{U}(t,t') \tag{A.73}$$

Indeed, as for Eq. (A.54), for t>t':

$$i\frac{\partial}{\partial t}e^{-i\int_{t'}^{t}\hat{H}(t'')dt''} = \hat{H}(t)\hat{U}(t,t')$$

As a result, we have obtained the *Second Dyson equation*:

$$\boxed{\hat{U}(t,t_0) = \hat{U}_0(t,t_0) - i\int_{t_0}^{t} \hat{U}(t,t')\hat{H}_I(t')\hat{U}_0(t',t_0)dt'} \tag{A.74}$$

In conclusion, thanks to Dyson Equations, in particular, the second one we have a very general equation to describe the time evolution of a quantum state $|\alpha\rangle$:

$$\boxed{|\alpha(t)\rangle = \hat{U}_0(t,t_0)|\alpha(t_0)\rangle - i\int_{t_0}^{t} \hat{U}(t,t')\hat{H}_I(t')\hat{U}_0(t',t_0)|\alpha(t_0)\rangle\, dt'} \tag{A.75}$$

This result, which we have given for granted in Chapter 2, now has a formal justification.

S-Matrix

In this last part, I'm going to present the strong field approximation, as a zero-order term solution of a more complicated object, whose braket, matrix element evaluated on a certain basis set, goes under the name of time-reversed *S-Matrix*[27].

Due to Eq. (A.58)

$$\hat{H} = \hat{H}_0 + \hat{H}_I(t)$$

however, it is also true that

$$\hat{H} = \hat{H}_F(t) + \hat{V}_C \tag{A.76}$$

where $\hat{V}_C$ is the coulomb potential operator and H_F is the free electron hamiltonian under and external electromagnetic field.

We, also, know that:

$$\hat{U}(t, t_0) = e^{-i\int_{t_0}^{t} \hat{H}(t')dt'}$$

hence,

$$\hat{U}(t, t_0) = \hat{U}_0(t, t_0) - i \int_{t_0}^{t} e^{-i\int_{t'}^{t} \hat{H}(t'')dt''} \hat{H}_I(t')\hat{U}_0(t', t_0)dt'$$

Now, for Eq. (A.76) it holds:

$$e^{-i\int_{t'}^{t} \hat{H}(t'')dt''} = e^{-i\int_{t'}^{t} \hat{H}_F(t'')dt''} e^{-i\int_{t'}^{t} \hat{V}_C dt''}$$

Due to the time-independence of the Coulomb potential we have $e^{-iV_C(t-t')}$, then a reasonable way of expanding the S-Matrix could be by exploiting the definition of an exponential operator as:

$$\hat{U}(t, t_0) = \hat{U}_0(t, t_0) - i \int_{t_0}^{t} e^{-i\int_{t'}^{t} \hat{H}_F(t'')dt''} (\sum_{n=0}^{\infty} \frac{(-i\hat{V}_C(t-t'))^n}{n!}) \hat{H}_I(t')\hat{U}_0(t', t_0)dt' \tag{A.77}$$

its zeroth term of V_C expansion is exactly the starting point of *Strong Field Approximation* (SFA), which in fact neglect the Coulomb potential.

$$\boxed{\hat{U}^{(0)}_{SFA}(t, t_0) = \hat{U}_0(t, t_0) - i \int_{t_0}^{t} e^{-i\int_{t'}^{t} \hat{H}_F(t'')dt''} \hat{H}_I(t')\hat{U}_0(t', t_0)dt'} \tag{A.78}$$

Higher order terms are the corrections of the approximated result that can be obtained with SFA.

For instance, the first order correction is:

$$\hat{U}^{(1)}(t, t_0) = -\int_{t_0}^{t} e^{-i\int_{t'}^{t} \hat{H}_F(t'')dt''} (t-t')\hat{V}_C \hat{H}_I(t')\hat{U}_0(t', t_0)dt' \tag{A.79}$$

Appendix B

Volkov electron pulses

A full quantum picture of an electron propagating freely in space under an electromagnetic field is a fundamental and necessary step in the understating of any Attosecond phenomena.
This is the reason why, in the following, I'm going to deepen in the proprieties of *Volkov states*, introduced in Chapter 2, by calculating and the plotting the time evolution of an electron wave-function under external field.
The resolution of this simple problem will highlight few interesting correlations between the electron propagation and the dispersion of a pulse in a dispersive medium.

Free propagation

Let us start with the simplest situation: free electron propagation with $\mathbf{E} = 0$, absence of electric field.

$$-\frac{\nabla^2}{2}\left|\psi\right\rangle = i\frac{\partial}{\partial t}\left|\psi\right\rangle \tag{B.1}$$

Exploiting the propagators, introduced in Chapter 2 and discussed in Appendix A, we can write the evolution, $|\psi(t)\rangle$ of a generic initial state, $|\psi(t_0)\rangle$ as

$$|\psi(t)\rangle = e^{-i\frac{1}{2}\hat{\mathbf{p}}^2(t-t_0)}\left|\psi(t_0)\right\rangle \tag{B.2}$$

As a matter of fact, if the initial state is $|\tilde{\mathbf{p}}\rangle$, eigenstate of momentum, then,

$$\langle\tilde{\mathbf{p}}|\, e^{-i\frac{1}{2}\hat{\mathbf{p}}^2(t-t_0)} = e^{-i\frac{1}{2}\tilde{\mathbf{p}}^2(t-t_0)}\,\langle\tilde{\mathbf{p}}| \tag{B.3}$$

Now, thanks to the completeness of $\hat{\mathbf{p}}$, Eq. (B.2) become:

$$|\psi(t)\rangle = \int_{\mathcal{R}^3} \langle\tilde{\mathbf{p}}|\psi(t_0)\rangle\, e^{-i\frac{1}{2}\tilde{\mathbf{p}}^2(t-t_0)}\,|\tilde{\mathbf{p}}\rangle\, d\tilde{\mathbf{p}} \tag{B.4}$$

For practical purposes we may want to look at the wavefunction, i.e. spatial projection of the ket-state, hence:

$$\psi(\mathbf{r},t) = \langle\mathbf{r}|\psi(t)\rangle = \frac{1}{(2\pi)^{\frac{3}{2}}}\int_{\mathcal{R}^3} \phi(\tilde{\mathbf{p}},t_0)e^{-i\frac{1}{2}\tilde{\mathbf{p}}^2(t-t_0)}e^{i\tilde{\mathbf{p}}\cdot\mathbf{r}}d\tilde{\mathbf{p}}$$

where $\phi(\tilde{\mathbf{p}}, t_0)$ is the wavefunction in momentum space a time t_0, and,

$$\langle \mathbf{r} | \tilde{\mathbf{p}} \rangle = \frac{1}{(2\pi)^{\frac{3}{2}}} e^{i\tilde{\mathbf{p}}\cdot\mathbf{r}} \tag{B.5}$$

see for details Appendix A.
Therefore,

$$\boxed{\psi(\mathbf{r}, t) = \frac{1}{(2\pi)^{\frac{3}{2}}} \int_{\mathcal{R}^3} \phi(\tilde{\mathbf{p}}, t_0) e^{-i\frac{1}{2}\tilde{\mathbf{p}}^2(t-t_0)} e^{i\tilde{\mathbf{p}}\cdot\mathbf{r}} d\tilde{\mathbf{p}}} \tag{B.6}$$

Eq. (B.6) is the general solution of any free space propagation problem, provided that we know the momentum profile ϕ at time $t = t_0$.

The careful observer with a background in optics may recognize in Eq. (B.6) the solution of a plane wave pulse whose propagating in an isotropic dispersive linear medium, [5].
Indeed, given **E** electric field and $\mathbf{k}(\omega) = k_0 + k_L(\omega - \omega_0) + \frac{GVD}{2}(\omega - \omega_0)$ wave vector, with GVD, group velocity dispersion, ω_0 carrier frequency, we have:

$$\mathbf{E}(z, t) = \frac{1}{4\pi} \int \tilde{\mathbf{E}}(\omega - \omega_0, z = 0) e^{-ik_L(\omega-\omega_0)z} e^{-ik_0 z} e^{-i\frac{1}{2}GVD(\omega-\omega_0)^2 z} e^{i\omega t} d\omega \tag{B.7}$$

A comparison between Eq. (B.7) and Eq. (B.6) leads to some interesting observation: *First* in quantum mechanics the role of time is the same of the space for a classical electromagnetic wave.
As a consequence, we expect that, as the time passes, our electron wave packet, or electron pulse, spatially expands as an electromagnetic wave pulse temporally broads.
Second the amplitude of the electron momentum spectrum $|\phi(\mathbf{r}, t)|$, i.e. the momentum distribution, conserves itself during the propagation, as a light pulse conserves its frequency spectrum amplitude, due to the linearity of the medium. What will change, for both, light pulse and electron pulse is the spectrum phase, [5].
Thus, we expect a progressively lost of a transformed limited condition, where the electron wave-packet has it minimum spatial extension and, consequently, the creation of a positive spatial chirp.

For the sake of simplicity, let us now solve Eq. (B.6) for gaussian wave packet.

$$\phi(\mathbf{p}, t_0) = \frac{1}{\sqrt{2\sigma_{px}\pi}} e^{-\frac{(p_x - p_{0x})^2}{4\sigma_x^2}} \frac{1}{\sqrt{2\sigma_{py}\pi}} e^{\frac{(p_y - p_{0y})^2}{4\sigma_y^2}} \frac{1}{\sqrt{2\sigma_{pz}\pi}} e^{\frac{(p_z - p_{0z})^2}{4\sigma_z^2}} \tag{B.8}$$

where σ_{pi} is the initial standard deviation in the i-th dimension ($i = x, y, z$) centered at p_{0i}.
To simplify even further, let's focus on just one dimension, in fact the 3D calculation is then straightforward.

So,

$$\psi(x,t) = \frac{1}{(2\pi)^{\frac{1}{2}}} \frac{1}{\sqrt{2\sigma_{px}\pi}} \int e^{-\frac{(p_x - p_{0x})^2}{4\sigma_x^2}} e^{-ip_x^2(t-t_0)} e^{ip_x x} dp_x$$

and,

$$\psi(x,t) = \frac{1}{(2\pi)^{\frac{1}{2}}} \frac{1}{\sqrt{2\sigma_{px}\pi}} \int e^{-\frac{p_x^2}{4\sigma_x^2}} e^{-\frac{p_{0x}^2}{4\sigma_x^2}} e^{\frac{2p_x p_{0x}}{4\sigma_x^2}} e^{-ip_x^2(t-t_0)} e^{ip_x x} dp_x$$

As a matter of fact,

$$I(x) = const \int_{\mathcal{R}} e^{-ax^2+bx^2+c} dx = \sqrt{\frac{\pi}{a}} e^{\frac{b^2}{4a}+c}$$

where in our case $a = (\frac{1}{4\sigma_{px}^2} + \frac{i}{2}(t-t_0)), b = (ix + \frac{2p_{0x}}{4\sigma_{px}^2})$ and $c = \frac{-p_0^2}{4\sigma_{px}^2}$.
By exploiting the previous equation, after few steps of calculations, which are very similar to the ones presented in appendix C of [5], one can achieve:

$$\psi(x,t) = N(t) exp(-\frac{(x - p_{0x}(t-t_0))^2}{\frac{1}{\sigma_{px}^2} + 4(t-t_0)^2\sigma_{px}^2}) exp(+i\frac{2x^2(t-t_0)\sigma_{px}^2 + \frac{1}{\sigma_{px}^2} x p_{0x}}{\frac{1}{\sigma_{px}^2} + 4(t-t_0)^2\sigma_{px}^2}) \tag{B.9}$$

The first term is a normalization factor, the second term provides us the propagation law for the probability amplitude of the electron wave-packet, the last pure-phase term is instead what could be called *Electron Chirp*.

At this point, we can make two observations:

1) The center of mass of the electron propagates following the classical trajectory $x(t) = p_{0x}(t-t_0)$.

2) The uncertainty on the position of Eq. (B.9) is proportional, at time t_0, to the inverse of the momentum uncertainty σ_{px},

$$2\sigma_x^2 = \frac{1}{\sigma_{px}^2} + 4(t-t_0)^2\sigma_{px}^2 \tag{B.10}$$

then, it broadens in time as a function of σ_{px}. In other words, the bigger is the uncertainty on the momentum the faster the wave-packet spreads in space.

The broadening has fundamental consequences on the efficiency of HHG process, indeed, as mentioned in Chapter 1, the more the electron wave function is broadened, the less intense is the recombination probability, in a three-step model framework, or the emitting-dipole magnitude in a more advanced formulation.

Electron Chirp

The electron chirp is a manifestation of a spatial distribution in the momentum which is embedded in the phase term of Eq. (B.9),

$$\phi_{eChirp}(x,t) = \frac{2x^2(t-t_0)\sigma_{px}^2 + \frac{1}{\sigma_{px}^2 x p_0}}{\frac{1}{\sigma_{px}^2} + 4(t-t_0)^2\sigma_{px}^2}$$

In fact, at time $t = t_0$, the distribution of momentum was homogeneous, as in the case of frequency distribution in a transformed limited light pulse [5], while for $t \neq t_0$ different portion of the wave-function has different expectation value for the momentum.

Now, we can exploit the analogy with the light pulse chirp, and we can introduce the "expectation value" of momentum in (x, t) as:

$$p_{spatialx}(x,t) = \frac{\frac{p_{0x}}{\sigma_{px}^2} + 4x(t-t_0)\sigma_{px}^2}{\frac{1}{\sigma_{px}^2} + 4(t-t_0)^2\sigma_{px}^2} \tag{B.11}$$

By this definition we can conclude the electron-chirp for a free electron as an always positive quantity. This is a trivial result, indeed, the "quantum trajectories" with higher initial momentum propagates faster and accumulates in the "rising edge" of the wave-packet.

This electron chirp, in the context of high harmonics generation for attosecond pulse generation, is an object which could have relevant consequences in the natural attosecond chirp, i.e. the chirp possessed by the attosecond chirp reflects proprieties of this electron wave packet chirp.

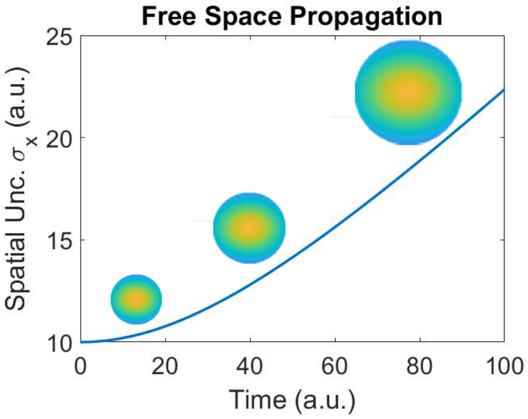

FIGURE B.1: Numerical simulation for the spatial uncertainty, i.e. the standard deviation of the gaussian in Eq. (B.10).

Propagation with an electromagnetic field

At last, it is worthwhile to discuss the propagation of a free electron with a given initial distribution.

Let us, first, spend a few words on the task from a purely physical perspective: From the electromagnetic wave perspective, an interaction with an electron in a free state cannot lead to photon absorption.
This is a purely energetic and momentum conservation requirement; hence, the only possible interaction is of the kind of Compton scattering. In this condition, the wave, after the interaction with the electron, loses a part of its energy, and, thus, slightly changing its frequency.
This justifies why in a fully quantum free electron picture, the electron velocity, and, as a consequence, its energy, can change continuously .

Let us now enter the mathematical formulation of the problem.
We have found in Chapter 2, that, the solution of

$$\hat{H}_F \left|\psi(t)\right\rangle = i\frac{\partial}{\partial t}\left|\psi(t)\right\rangle \tag{B.12}$$

where $\hat{H}_F = \frac{1}{2}(\hat{\mathbf{p}} + \mathbf{A}(t))^2$, is:

$$\left|\psi(t)\right\rangle = \int \left|\Psi_{VOLKOV}(\mathbf{p}, t, t_0)\right\rangle \left|\phi(\mathbf{p}, t_0)\right\rangle d\mathbf{p} \tag{B.13}$$

a superposition of Volkov wavefunctions, weighted by the wavefunction in the momentum space $\phi(\mathbf{p}, t_0)$.

$$\left|\Psi_{VOLKOV}(\mathbf{p}, t, t_0)\right\rangle = e^{-\frac{i}{2}S(t,t_0)}\left|\mathbf{p}\right\rangle \tag{B.14}$$

where S is the quantum phase or semi-classical action, with $\mathbf{p}$ a fixed, and, hence, time-independent quantity.

$$S = \frac{1}{2}\int_{t_0}^{t}(\mathbf{A}(t') + \mathbf{p})^2 \tag{B.15}$$

For practical purposes we can evaluate the final wavefunction, $\psi(\mathbf{r}, t)$, by projecting Eq. (B.13) in the space eigenkets,

$$\psi(\mathbf{r}, t) = \frac{1}{(2\pi)^{\frac{3}{2}}}\int_{\mathcal{R}^3} e^{-\frac{i}{2}\int_{t_0}^{t} A^2(t)} e^{-i\int_{t_0}^{t}\mathbf{A}(t)\cdot\mathbf{p}} e^{-\frac{i}{2}p^2(t-t_0)} e^{i\mathbf{p}\cdot\mathbf{r}}\phi(\mathbf{p}, t_0)d\mathbf{p} \tag{B.16}$$

This object has some interesting feature that makes it analogous to Eq. (B.7).
Previously, the analogy between electron wavepacket and light pulse was claimed by neglecting k_L, now, thanks to the electromagnetic potential we are introducing this term, making the analogy complete.
As a matter of fact, the momentum component which feels the electromagnetic field is the one in the field polarization direction, therefore we can discuss everything in a simple 1D model.
Assuming, now, a linear polarization in x-direction, we can evaluate a simpler

integral:

$$\psi(x,t) = N_0(t) \int_{\mathcal{R}} e^{-ip_x \int_{t_0}^{t} A(t)} e^{-\frac{i}{2}p_x^2(t-t_0)} e^{ip_x x} e^{-\frac{(p_x-p_{0x})^2}{4\sigma_x^2}} dp_x \tag{B.17}$$

where we have already assumed a gaussian distribution for the momentum centered at p_{0x} with standard deviation σ_{px}.

The integral is identical to the previous one with the only difference that now the $x \to x - \int_{t_0}^{t} A$. Thus, we can use the result of Eq. (B.9) and write:

$$\psi(x,t) = N(t)exp(-\frac{(x - \int_{t_0}^{t} A(t) - p_{0x}(t-t_0))^2}{\frac{1}{\sigma_{px}^2} + 4(t-t_0)^2\sigma_{px}^2}) \times ...$$

$$... \times exp(+i\frac{2(x - \int_{t_0}^{t} A(t))^2(t-t_0)\sigma_{px}^2 + \frac{1}{\sigma_{px}^2}(x - \int_{t_0}^{t} A(t))p_{0x}}{\frac{1}{\sigma_{px}^2} + 4(t-t_0)^2\sigma_{px}^2})$$

In this case, the center of mass of the electron propagates following the expected classical law:

$$\boxed{x_b(t) = p_{0x}(t-t_0) + \int_{t_0}^{t} A(t')dt'} \tag{B.18}$$

while the electron wave-packer spatial dispersion is not influenced by the field, this is reasonable since the field is homogeneous and the "quantum paths" are influenced in the same way by the electromagnetic wave.
Another effect of the field is to change the electron-chirp in a way that depends on the electromagnetic field shape.

$$exp\Big(+ i\frac{2(x - \int_{t_0}^{t} A(t))^2(t-t_0)\sigma_{px}^2 + \frac{1}{\sigma_{px}^2}(x - \int_{t_0}^{t} A(t))p_{0x}}{\frac{1}{\sigma_{px}^2} + 4(t-t_0)^2\sigma_{px}^2}\Big) \tag{B.19}$$

Eq. (B.19) can be used, for example, to extend a "semi"-classical model like the three step model of Chapter 1, including also electron-phase and wave-packet effects in the HHG. Before concluding this discussion allow me to make few comments on the results we have achieved thanks to this simple model for the free electron propagation driven by an intense:

i) If we assume an initial spatial uncertainty of $\Delta x = 1$ a.u. (electron initially localized in 0.05 nm, reasonable for an initially bounded electron) it sets a momentum uncertainity of $\Delta p_x = 1$ a.u. which in absence of a field implies $\approx 1/100$ the speed of light.

ii) If the electron feels the whole electric field, from $-\infty$ to $+\infty$ then its final velocity is the same of the initial one. If instead, for some reason, see Chapter 2 and Chapter 3, the electron is generated at a intermediate time, then its final energy may be different from the original one. *This is way in a streaking trace the photo-electrons energy distribution is not flat!*

iii) If we set an initial average momentum at zero, with external field with peak intensity around $10^{13}\,\frac{W}{cm^2}$ we can model in a purely quantum way the propagation of the three step model, see Chapter 1. We can predict, then, both the electron maximum distance from the starting point (≈ 1 nm) and the dispersion of the electron wave-packet, hence the decrease of recombination efficiency, see Chapter 2.

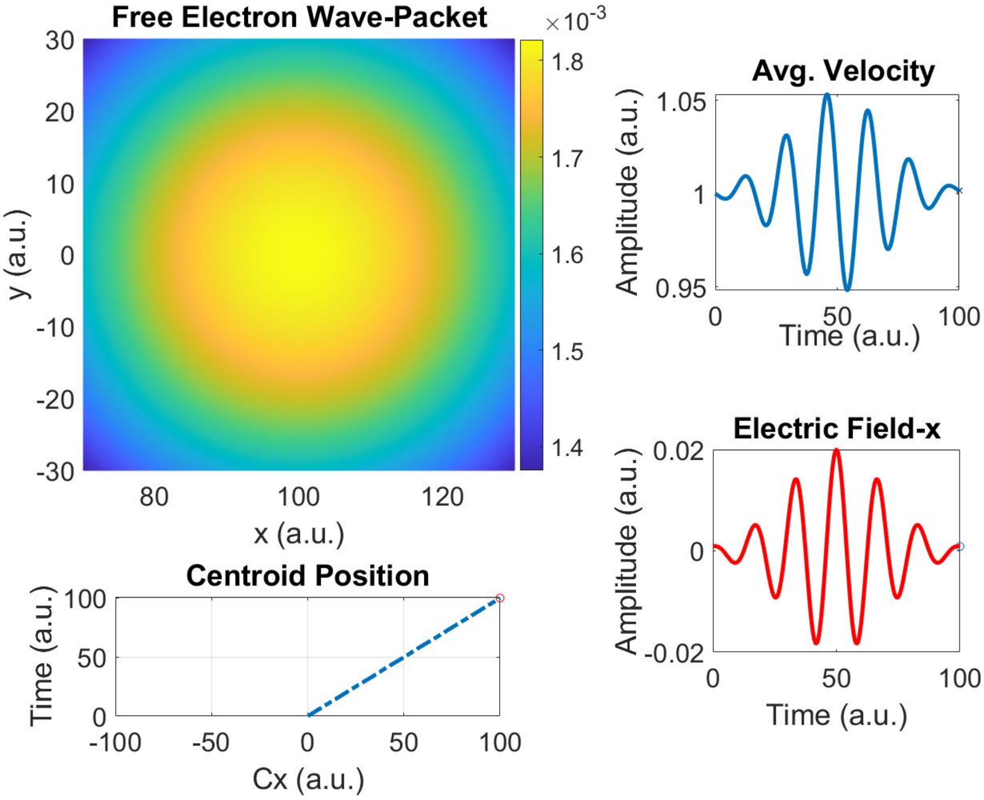

FIGURE B.2: Simulation of a 2D propagation in a $10^{13}\,\frac{W}{cm^2}$ field, with initial velocity in x-direction set at 1 a.u., and an initial uncertainty on the momentum $\sigma_{px} = 0.1$. With such an high initial velocity the electron center of much is barely influenced by the field, top-right corner. Due to the fact that the electron feels the whole electromagnetic field, then, the final velocity is the same of the initial one. Moreover, the field, which is quite intense, see Chapter 1, causes at most variations of "just" the 5% percent, which corresponds to a maximum increase in velocity of $\approx 10^{-4}$ c, where c is the speed of light, bottom-left panel.

Appendix C

Atomic units

The following discussion is inspired by [27].

Atomic units are usually seen so confusing since everything is expressed as an a-dimensional quantity.
However, they are extremely useful in simulations, and, additionally, they are the most natural form to evaluate physical laws at a macroscopic level.
The most common choice is to set $e = 1$ a.u., where e is the positive elementary charge, $\hbar = 1$ a.u., $m_e = 1$ a.u., mass of an electron, and, finally $4\pi\epsilon_0 = 1$ a.u. .
Obviously, at the end of the calculation, one should not forget that the a-dimensionality is just a matter of convention[1], and do not allow any inappropriate mixing between different basic units.

From a microscopic level the four fundamental quantities of SI are time $[T]$, length $[L]$, charge $[C]$, mass $[M]$.
Therefore, a connection between these quantities and the atomic units must be setup, this will create a clear map between any choice of units.
In fact, once this is done we can express an arbitrary physical quantity from a.u. to S.I units and vice versa.

$$\begin{aligned}\hbar &= [M]^{a_{11}}[L]^{a_{12}}[T]^{a_{13}}[C]^{a_{14}}\\ m_e &= [M]^{a_{21}}[L]^{a_{22}}[T]^{a_{23}}[C]^{a_{24}}\\ e &= [M]^{a_{31}}[L]^{a_{32}}[T]^{a_{33}}[C]^{a_{34}}\\ 4\pi\epsilon_0 &= [M]^{a_{41}}[L]^{a_{42}}[T]^{a_{43}}[C]^{a_{44}}\end{aligned}$$

From the physical meaning that we know this quantity have we can write the following matrix which elements are the coefficient to be put in previous equation

$$A = \begin{pmatrix} 1 & 2 & -1 & 0 \\ 1 & 0 & 0 & 0 \\ 0 & 0 & 0 & 1 \\ -1 & -3 & 2 & 2 \end{pmatrix} \tag{C.1}$$

It is now relevant to derive the relation between the four fundamental basic units of SI and our atomic units.

---

[1] In other words, 1 a.u. of charge is different from 1 a.u. of mass.

For analogy,

$$[M] = \hbar^{b_{11}} m_e^{b_{12}} e^{b_{13}} (4\pi\epsilon_0)^{b_{14}} \tag{C.2}$$

$$[L] = \hbar^{b_{21}} m_e^{b_{22}} e^{b_{23}} (4\pi\epsilon_0)^{b_{24}} \tag{C.3}$$

$$[T] = \hbar^{b_{31}} m_e^{b_{32}} e^{b_{33}} (4\pi\epsilon_0)^{b_{34}} \tag{C.4}$$

$$[C] = \hbar^{b_{41}} m_e^{b_{42}} e^{b_{43}} (4\pi\epsilon_0)^{b_{44}} \tag{C.5}$$

Let us, for instance, evaluate time in atomic units, then by exploiting the A matrix definition, we can write:

$$\begin{aligned}
\hbar^{b31} &= [M]^{b_{31}}[L]^{2b_{31}}[T]^{-b_{31}} \\
m_e^{b_{32}} &= [M]^{b_{32}} \\
e^{b_{33}} &= [M]^{b_{31}} \\
4\pi\epsilon_0^{b_{34}} &= [M]^{-b_{34}}[L]^{-3b_{34}}[T]^{2b_{34}}[C]^{2b_{34}}
\end{aligned}$$

Then,

$$[T] = [M]^{b_{31}+b_{32}-b_{34}}[L]^{2b_{31}-3b_{34}}[T]^{-b_{31}+2b_{34}}[C]^{b_{33}+2b_{34}} \tag{C.6}$$

Thus,

$$\begin{cases}
b_{31} + b_{32} - b_{34} = 0 \\
2b_{31} - 3b_{34} = 0 \\
-b_{31} + 2b_{34} = 1 \\
b_{33} + 2b_{34} = 0
\end{cases} \tag{C.7}$$

As a result we found the coefficient which as to be substituted in Eq. (C.4).

$$[T] = \hbar^3 m_e^{-1} (4\pi\epsilon_0)^2 e^{-4} \approx 24.189\, as \tag{C.8}$$

In general, it can be proved by iterating this same procedure:

$$B = \begin{pmatrix} 0 & 1 & 0 & 0 \\ 2 & -1 & -2 & 1 \\ 3 & -1 & -4 & 2 \\ 0 & -0 & 1 & 0 \end{pmatrix} \tag{C.9}$$

Let me allow to spoil the reader some other relevant quantities in Attosecond physics.

The energy in atomic units is:

$$E = \frac{\hbar}{[T]} = \frac{m_e e^4}{(4\pi\epsilon_0)^2 \hbar^2} = 1\, a.u \approx 27.21\, eV \tag{C.10}$$

the energy in atomic units is 2 times the ionization potential of hydrogen.
We may also be curious to evaluate the peak intensity of a pulse in atomic units.

Since one atomic units of electric field is $E_{field} = 1\ a.u. = 5.14\ 10^{11}\ \frac{V}{m}$, then:

$$I_{peak} = \frac{1}{2}\epsilon_0 c|E_{field}|^2 = 1\ a.u. \approx 3.5\ 10^{16}\ \frac{W}{cm^2} \tag{C.11}$$

Which is a quite intense field compared to the typical attosecond science intensities, which are, instead, in the neighbor of $10^{13}\ \frac{W}{cm^2}$.

A more comprehensive overlook on the units is resumed in the following table.

Name	Atomic units	SI value
action	$\hbar$	$1.054571817\ 10^{-34}$ Js
charge	e	$1.602176634\ 10^{-19}$ C
length	a_0	$5.29177210903\ 10^{-11}$ m
mass	m_e	$9.1093837015\ 10^{-31}$ kg
energy	$E_h = \frac{m_e e^4}{(4\pi\epsilon_0)^2\hbar^2}$	$4.35971\ 10^{-18}$ J (27.21 eV)
electric dipole moment	ea_0	$8.4783536255\ 10^{-30}$ Cm
electric field	$E_{\mathrm{h}}/(ea_0)$	$5.14220674763\ 10^{11}$ Vm^{-1}
time	$\hbar/E_h$	$2.4188843265857\ 10^{-17}$ s
velocity	$a_0E_h/\hbar$	$2.18769126364\ 10^{6}$ ms^{-1}
peak intensity	$\frac{c\epsilon_0}{2}E_h^2$	$3.511\ 10^{16}\ \frac{W}{cm^2}$

References

[1] J.D Jackson. *Classical Electrodynamics, 1st edition*. John Wiley and Sons, 1962.

[2] Chang Zenghu. *Fundamentals of Attosecond Optics*. CRC Press; 2011.

[3] F. Calegari et al. "Ultrafast electron dynamics in phenylalanine initiated by attosecond pulses". In: *Science* (2014).

[4] Ferenc Krausz and Misha Ivanov. "Attosecond physics". In: *Rev. Mod. Phys.* 81.1 (2009), pp. 163–234. ISSN: 15390756. DOI: `10.1103/RevModPhys.81.163`.

[5] M. Zavelani-Rossi and F. Vismarra. *High Intensity Laser for physical and nuclear applications*. Esculapio, 2020.

[6] A. McPherson et al. "Studies of multiphoton production of vacuum-ultraviolet radiation in the rare gases". In: *J. Opt. Soc. Am. B* (1987).

[7] P. Villoresi et al. "Isolated Single-Cycle Attosecond Pulses". In: *Science* (2006).

[8] F. Calegari et al. "Charge migration induced by attosecond pulses in bio-relevant molecules". In: *Journal of Physics B: Atomic, Molecular and Optical Physics* 49 (June 2016). DOI: `10.1088/0953-4075/49/14/142001`.

[9] G. Sansone et al. "Electron localization following attosecond molecular photoionization". In: *Nature* (2010).

[10] F. Schläpfer et al. "Attosecond optical-field-enhanced carrier injection into the GaAs conduction band". In: *Nature Physics* (2018).

[11] M. Sabbar et al. "Combining attosecond XUV pulses with coincidence spectroscopy". In: *Rev. Sci. Instrum.* 85.10 (2014). ISSN: 10897623. DOI: `10.1063/1.4898017`. URL: `http://dx.doi.org/10.1063/1.4898017`.

[12] Misha Yu Ivanov, Michael Spanner, and Olga Smirnova. "Anatomy of strong field ionization". In: *J. Mod. Opt.* 52.2-3 (2005), pp. 165–184. ISSN: 09500340. DOI: `10.1080/0950034042000275360`.

[13] M. Schultze et al. "Delay in photoemission". In: *Science (80-.).* 328.5986 (2010), pp. 1658–1662. ISSN: 00368075. DOI: `10.1126/science.1189401`.

[14] A.S. Landsman and Ursula Keller. "Attosecond science and the tunnelling time problem". In: *Phys. Rep.* 547.1 (2015), pp. 1–24. ISSN: 03701573. DOI: `10.1016/j.physrep.2014.09.002`. URL: `http://dx.doi.org/10.1016/j.physrep.2014.09.002`.

[15] Y. Mairesse and F. Quéré. "Frequency-resolved optical gating for complete reconstruction of attosecond bursts". In: *Phys. Rev. A - At. Mol. Opt. Phys.* 71.1 (2005), pp. 1–4. ISSN: 10502947. DOI: `10.1103/PhysRevA.71.011401`.

[16] J. White and Z. Chang. "Attosecond streaking phase retrieval with neural network". In: *Opt. Express* 27.4 (ts), pp. 4799–4807.

[17] R. Trebino et al. "Measuring ultrashort laser pulses in the time-frequency domain using frequency-resolved optical gating". In: *Review of Scientific Instruments* 68.9 (1997), pp. 3277–3295. DOI: `10.1063/1.1148286`. URL: `https://doi.org/10.1063/1.1148286`.

[18] P. Keathley et al. "Volkov transform generalized projection algorithm for attosecond pulse characterization". In: *New Journal of Physics* 18 (July 2016), p. 073009. DOI: `10.1088/1367-2630/18/7/073009`.

[19] M. Lucchini et al. "Ptychographic reconstruction of attosecond pulses". In: *Opt. Express* 23.23 (2015), p. 29502. ISSN: 1094-4087. DOI: `10.1364/oe.23.029502`. arXiv: `1508.07714`.

[20] Matteo Lucchini and Mauro Nisoli. "Refined ptychographic reconstruction of attosecond pulses". In: *Appl. Sci.* 8.12 (2018). ISSN: 20763417. DOI: `10.3390/app8122563`.

[21] R. Boge et al. "Revealing the time-dependent polarization of ultrashort pulses with sub-cycle resolution". In: *Opt. Express* 22.22 (2014), pp. 26967–26975.

[22] M. Murari et al. "Robustness of the ePIE algorithm for the complete characterization of femtosecond, extreme ultra-violet pulses". In: *Opt. Express* 28.7 (2020), p. 10210. ISSN: 1094-4087. DOI: `10.1364/oe.388907`.

[23] T. Gaumnitz, Arohi Jain, and Hans Jakob Wörner. "Complete reconstruction of ultra-broadband isolated attosecond pulses including partial averaging over the angular distribution". In: *Opt. Express* 26.11 (ts), pp. 14719–14740. DOI: `10.1364/OE.26.014719`.

[24] J. J. Sakurai and Jim Napolitano. *Modern Quantum Mechanics*. Cambridge University Press, 1985.

[25] A. Ludwig et al. "Breakdown of the dipole approximation in strong-field ionization". In: *Phys. Rev. Lett.* 113.24 (2014), pp. 1–5. ISSN: 10797114. DOI: `10.1103/PhysRevLett.113.243001`. arXiv: `1408.2336`.

[26] A. D. Bandrauk, F. Fillion-Gourdeau, and E. Lorin. "Atoms and molecules in intense laser fields: Gauge invariance of theory and models". In: *J. Phys. B At. Mol. Opt. Phys.* 46.15 (2013). ISSN: 09534075. DOI: `10.1088/0953-4075/46/15/153001`. arXiv: `1302.2932`.

[27] Peter Mulser and Dieter Bauer. *High Power Laser-Matter*. Springer, 2010.

[28] Zi Jian Long and Wing Ki Liu. "Keldysh theory of strong-field ionization". In: *Can. J. Phys.* 88.4 (2010), pp. 227–245. ISSN: 00084204. DOI: `10.1139/P09-111`.

[29] F. H.M. Faisal. "Gauge-invariant intense-field approximations to all orders". In: *J. Phys. B At. Mol. Opt. Phys.* 40.7 (2007). ISSN: 09534075. DOI: `10.1088/0953-4075/40/7/F02`.

[30] Markus Kitzler et al. "Quantum Theory of Attosecond XUV Pulse Measurement by Laser Dressed Photoionization". In: *Phys. Rev. Lett.* 88.17 (2002), p. 4. ISSN: 10797114. DOI: `10.1103/PhysRevLett.88.173904`.

[31] D. Bauer, D. B. Miloevi, and W. Becker. "Strong-field approximation for intense-laser atom processes: The choice of gauge". In: *Phys. Rev. A - At. Mol. Opt. Phys.* 72.2 (2005), pp. 1–5. ISSN: 10502947. DOI: `10.1103/PhysRevA.72.023415`. arXiv: `0504053 [quant-ph]`.

[32] A. D. Bandrauk, F. Fillion-Gourdeau, and E. Lorin. "Atoms and molecules in intense laser fields: Gauge invariance of theory and models". In: *J. Phys. B At. Mol. Opt. Phys.* 46.15 (2013). ISSN: 09534075. DOI: `10.1088/0953-4075/46/15/153001`. arXiv: `1302.2932`.

[33] L.V. Keldysh. "Ionization in the Field of a Strong Electromagnetic Wave". In: *Soviet Physics Jetp* 20.5 (1965).

[34] A. Scrinzi. "Attosecond physics-theory". Unpublished Lecture Notes.

[35] K. Amini et al. "Symphony on strong field approximation". In: *Rep. Prog. Phys.* 82.11 (2019), p. 116001. ISSN: 13616633. DOI: `10.1088/1361-6633/ab2bb1`. arXiv: `1812.11447`.

[36] T. Schultz. *Attosecond and XUV Physics*. Wiley, 2014. ISBN: 9780470387719.

[37] D. B. Milošević et al. "Above-threshold ionization by few-cycle pulses". In: *J. Phys. B At. Mol. Opt. Phys.* 39.14 (2006). ISSN: 09534075. DOI: `10.1088/0953-4075/39/14/R01`.

[38] L Landau and Lifsits E. *Theoretical Physics Vol III*. Editori Riuniti, university press, 2010.

[39] C. Hofmann et al. "Interpreting electron-momentum distributions and nonadiabaticity in strong-field ionization". In: *Phys. Rev. A - At. Mol. Opt. Phys.* 90.4 (2014). ISSN: 10941622. DOI: `10.1103/PhysRevA.90.043406`.

[40] H. R. Reiss and V. P. Krainov. "Approximation for a Coulomb-Volkov solution in strong fields (Phys. Rev. A (1994) 50 (R910))". In: *Phys. Rev. A - At. Mol. Opt. Phys.* 74.4 (2006), pp. 910–912. ISSN: 10502947. DOI: `10.1103/PhysRevA.74.049903`.

[41] Diego G. Arbó et al. "Coulomb-Volkov approximation for near-threshold ionization by short laser pulses". In: *Phys. Rev. A - At. Mol. Opt. Phys.* 77.1 (2008), pp. 1–8. ISSN: 10502947. DOI: `10.1103/PhysRevA.77.013401`.

[42] D. B. Milošević and W. Becker. "Atom-Volkov strong-field approximation for above-threshold ionization". In: *Phys. Rev. A* 99.4 (2019), pp. 1–7. ISSN: 24699934. DOI: `10.1103/PhysRevA.99.043411`.

[43] J. M. Dahlström, A. L'Huillier, and A. Maquet. "Introduction to attosecond delays in photoionization". In: *J. Phys. B At. Mol. Opt. Phys.* 45.18 (2012). ISSN: 09534075. DOI: `10.1088/0953-4075/45/18/183001`. arXiv: `1205.6624`.

[44] A.S. Kheifets. "The attoclock and the tunneling time debate". In: *Journal of Physics B: Atomic, Molecular and Optical Physics* 53.7 (2020), p. 072001. DOI: `10.1088/1361-6455/ab6b3b`. URL: `https://doi.org/10.1088%2F1361-6455%2Fab6b3b`.

[45] H. Wei, Toru Morishita, and C. D. Lin. "Critical evaluation of attosecond time delays retrieved from photoelectron streaking measurements". In: *Phys. Rev. A* 93.5 (2016), pp. 1–14. ISSN: 24699934. DOI: `10.1103/PhysRevA.93.053412`.

[46] H. Wei et al. "Benchmarking accurate spectral phase retrieval of single attosecond pulses". In: *Phys. Rev. A* (2015).

[47] L. Cattaneo et al. "Comparison of attosecond streaking and RABBITT". In: *Opt. Express* 24.25 (2016), pp. 29060–29076. DOI: `10.1364/OE.24.029060`. URL: `http://www.opticsexpress.org/abstract.cfm?URI=oe-24-25-29060`.

[48] P. Dirac. *The Principles of Quantum Mechanics*. Oxford University Press, 2012.

[49] R. Loudon. *The Quantum Theory of Light*. Oxford Univeristy Press, 2010.

[50] K. W. Chan, C. K. Law, and J. H. Eberly. "Localized Single-Photon Wave Functions in Free Space". In: *Phys. Rev. Lett.* 88.10 (2002), p. 4. ISSN: 10797114. DOI: `10.1103/PhysRevLett.88.100402`.

[51] A. Messiah. *Quantum mechanics*. Dover, 1995.

[52] P. Dennery. *Mathematics for physicist, 1st edition*. Dover, 1995.